Dissertations and Theses (Open Access)   MD Anderson UTHealth Houston Graduate School

5-2012

Role Of Sox9 In Uterine Gland Development And Disease Initiation

Gabriel Gonzalez

Follow this and additional works at: https://digitalcommons.library.tmc.edu/utgsbs_dissertations

Part of the Medicine and Health Sciences Commons

ROLE OF SOX9 IN UTERINE GLAND DEVELOPMENT

AND DISEASE INITIATION

A

DISSERTATION

Presented to the Faculty of

The University of Texas

Health Science Center at Houston

and

The University of Texas

M. D. Anderson Cancer Center

Graduate School of Biomedical Sciences

in Partial Fulfillment

of the Requirements

for the Degree of

DOCTOR OF PHILOSOPHY

by

Gabriel Gonzalez, M.S.

Houston, Texas

May, 2012

To my past self, he who did the work.

To my present self, he who is writing this dissertation.

And to my future self, he who will savor all my hard work.

Acknowledgements

I have to acknowledge every single person that knowingly or unknowingly contributed to the ideas that I will put forward in this thesis. Every new idea I heard or read stimulated new connections in my brain, which in turn provoked the emergence of new ideas. Conversations with colleagues and even people outside the science community have all, in some way, contributed to this work. Of equal or perhaps more importance, I have to acknowledge all scientists and engineers that have contributed to the ideas that I used to build upon in this thesis.

I have to thank Dr. Behringer for providing me with the resources, the excellent mentorship, and a great place to conduct scientific studies. I could have not asked for a better mentor. Dr. Broaddus, a member of my advisory committee, not only provided me with human tissue slides, he also sat down with me to look at my slides and explain the morphological changes present on the tissues derived from mutant mice. I have to thank Jenny Deng all the help she has provided me over the years. Ying Wang helped me with histology, and as you will see, most of my observations and arguments relied heavily on histology. One particular person that requires my acknowledgment is Haruhiko Akiyama; a person I have heard about but have not actually met. Most of the mouse lines used throughout my Ph.D. work were envisioned and generated by Dr. Akiyama. I also have to thank Allison Stewart for all her help. Jichao Chen performed the OPT imaging I used to generate the 3D imaging of the uterus. Hao Chang

Role of Sox9 in Uterine Gland Development and Disease Initiation

Publication No._____*

Gabriel Gonzalez, M.S.

Supervisory Professor: Richard R. Behringer, Ph. D.

The female reproductive tract (FRT) develops midway through embryogenesis, and consists of oviducts, uterine horns, cervix and upper part of the vagina. The uterine horns are composed of an epithelial layer, luminal (LE) and glandular epithelium (GE), surrounded by a mesenchymal layer, the stroma and myometrium. Interestingly, in most mammals the GE forms after birth and it only becomes fully differentiated as the female reaches sexual maturity. Uterine glands (UG) are made up of GE and are present in all mammals. They secrete nutrients, cytokines and several other proteins, termed histotroph, that are necessary for embryo implantation and development. Experiments in ewes and mice have revealed that females who lack UGs are infertile mainly due to impaired implantation and early pregnancy loss, suggesting that UGs are essential for fertility. Fortunately for us, UGs develop after birth allowing us to peer into the genetic mechanism of tubulogenesis and branching morphogenesis; two processes that are disrupted in various adenocarcinomas (cancer derived from glands).

We created 3D replicas of the epithelium lining the FRT using optical projection tomography and characterized UG development in mice using lineage-tracing experiments. Our findings indicate that mouse UGs develop as simple tubular structures and later grow multiple secretory units that stem from the main duct.

The main aim of this project was to study the role of SOX9 in the UGs. Preliminary studies revealed that Sox9 is mostly found in the nucleus of the GE.

This observation led to the hypothesis that Sox9 plays a role in the formation and/or differentiation of the GE. To study the role of Sox9 in UGs differentiation, we conditionally knocked out and overexpressed Sox9 in both the LE and GE using the progesterone receptor (Pgr) promoter. Overexpressing *Sox9* in the uterine epithelium, parts of the stroma, and myometrium led to formation of multiple cystic structures inside the endometrium. Histological analysis revealed that these structures appeared morphologically similar to structures present in histological tissue sections obtained from patients with endometrial polyps. We have accounted for the presence of simple and complex hyperplasia with atypia, metaplasia, thick-walled blood vessels, and stromal fibrosis; all "hallmarks" that indicate overexpressing *Sox9* leads to development of a polyp-like morphology. Therefore, we can propose the use of *Sox9-cOE* mice to study development of endometrial cystic lesions and disease progression into hyperplastic lesions.

Supervisory Committee:

Richard Behringer, Ph.D., Chair

Michelle Barton, Ph.D.

Russell Broaddus, M.D., Ph.D.

Yasuhide Furuta, Ph.D.

Michael Galko, Ph.D.

Table of Contents

List of Illustrations

List of Tables

Abbreviations

FRT= female reproductive tract

E= embryonic day

UG= uterine gland

TS= tail somite

AMH= anti-Müllerian hormone

LE= luminal epithelium

GE= glandular epithelium

E2= estrogen

P4= progesterone

ECM= extracellular matrix

OPT= optical projection tomography

R26R-RG= Rosa-26-Reporter--H_2B-mCherry-EGFP-GPI

SOX9-LP= Sox9-lineage positive

GFP= green fluorescent protein

Sox9-cKO= Pgr-Cre; Sox9 fx/fx

Sox9-cOE= Pgr-Cre; CAG-loxP-mRFP1-stop-loxP-SOX9-Ires-EGFP

Chapter I. Introduction

The Mammalian Female Reproductive Tract

In therian mammals, fertilization, implantation and embryo development take place inside the mother's reproductive tract. During evolution, the mammalian female reproductive tract (FRT) adapted to incorporate a novel strategy: to shelter and nourish the new life developing inside the body instead of exposing the fetus to outside hazards. In mammals, conception is initiated by sex hormones that ready the female for pregnancy. Upon hormonal cues, inside the ovary, depending on the species, one or multiple oocytes mature and is/are released into the oviduct interspace. In the oviduct, fimbriae covered with cilia collect and transport the oocytes into the uterus[1,2]. After mating, sperm enters the FRT, travels through the uterus and towards the oviduct/fallopian tube where it encounters and fertilizes the oocytes. In laboratory mice, mating and subsequent fertilization usually take place during the night, therefore, we consider the embryo the next day around noon to be at embryonic day (E0.5). Muscle contractions in the oviduct move the embryo into the uterus through the uterotubal junction[2]. By the time the embryo reaches the uterine cavity (~E3.5), it has undergone several cleavage divisions and is considered to be at the blastocyst stage. Before attaching to the uterine wall, the embryo breaks free from the zona pellucida, a protective layer surrounding the embryo. Once outside this protective layer, the embryo must attach to the epithelium lining the uterine cavity and burrow into the

stroma, where it will remain for the rest of gestation. Before encasing itself in the mother's womb, the embryo obtains many of the nutrients it requires from the milieu of the uterine cavity[3]. Experiments in pigs have shown that the uterine glands (UG) secrete various nutrients, cytokines and several other proteins, termed histotroph, into the uterine cavity[4]. Therefore, UGs secrete the nutrients essential for embryo viability during the first critical stages of development.

Formation of the Female Reproductive Tract

The FRT develops from the Müllerian duct (paramesonephric duct). In mice, around Tail Somite (TS) Stage 19 or E11.5, cells in the coelomic epithelium apparently invaginate next to the Wolfian duct (mesonephric duct). The Müllerian duct elongates adjacent to the Wolfian duct until it reaches the urogenital sinus at TS34[5]. In females, the Müllerian duct differentiates into the FRT, while in males, fetal Sertoli cells of the testis secrete anti-Müllerian Hormone (AMH), a member of the Transforming Growth Factor-β superfamily, which induces Müllerian duct regression[6]. In females, the absence of testosterone leads to Wolfian duct degeneration, while the Müllerian duct gives rise to the oviducts, uterine horns, cervix and upper part of the vagina[7]. All four sections derived from the Müllerian duct connect with each other and form functional compartments or parenchyma. Interestingly, the cells that make up each compartment, although derived from the same progenitor pool, appear remarkably morphologically different from one another. The oviducts, which connect to their respective uterine horns, show

varying cellular morphology throughout their subcompartments: the infundibulum, the ampulla and the isthmus[1,8]. The infundibulum is made up of tall fimbriae covered in cilia used to collect the oocytes and transport them into the ampulla. The ampulla contains both tall columnar epithelium covered in cilia and secretory cells[1,9]. The next subcompartment is the isthmus, an area containing mostly secretory epithelia encircled by a dense muscle layer, the myometrium. The myometrium helps generate peristaltic contractions that push the embryo past the uterotubal junction and into the uterine horns[2]. The uterine horns are made of a functional layer called the endometrium surrounded by a myometrium and covered by the serosa. The uterine epithelium regulates the passage of molecules between the endometrium and the uterine lumen[10]. The epithelium covering the uterine lumen is called the **luminal epithelium (LE),** while the **glandular epithelium (GE)** extends out from the LE into the **stroma**, the region between the LE and the myometrium (Figure 1). Upon hatching from the zona pellucida, the embryo attaches to the LE, burrows into the stroma and later establishes the fetal-placental network. The placenta provides direct access to all the nutrients, oxygen and waste exchange the developing fetus will require for full gestation[11,12]. Molecular signals trigger a cascade of reactions that generate heavy contractions of the myometrium that help push the fetus into the cervical canal at parturition[13]. The cervix is divided into two parallel hollowed epithelial tubes surrounded by a thick myometrium. Both cervical tubes open into the vagina.

Figure 1: The human and mouse female reproductive system. (A) Illustration of the human reproductive system (http://genericlook.com/img/uploads/anatomy/uterus.jpg). (B) The adult female reproductive tract of the mouse. (C) H&E stain histological cross section of the adult mouse uterus. (D) Illustration of the mouse uterus, showing the position where the embryo implants (http://www.informatics.jax.org/greenbook/images/12-11.jpg). GE, glandular epithelium; LE, luminal epithelium; M, mesometrial side; A, antimesometrial side; Ant, anterior; Post, posterior.

A

fallopian tube

ovary

vagina

uterus

cervix

B

ovary

oviduct

uterus

C

stroma

myometrium

LE

GE

D

M

uterus

Dorsal

Ant.   Post.

Ventral

embryo

A

B

C

A
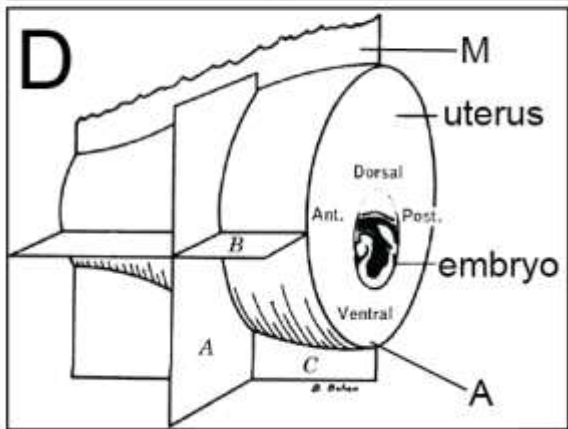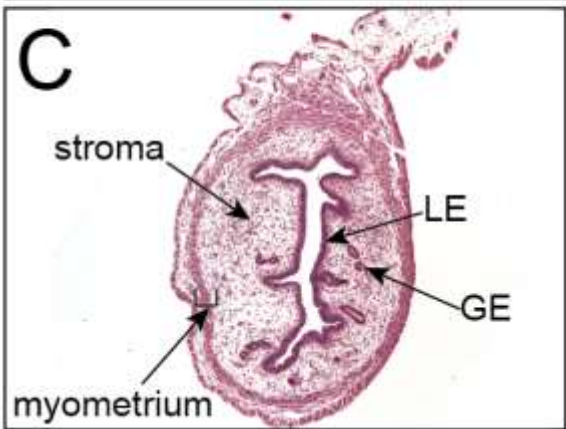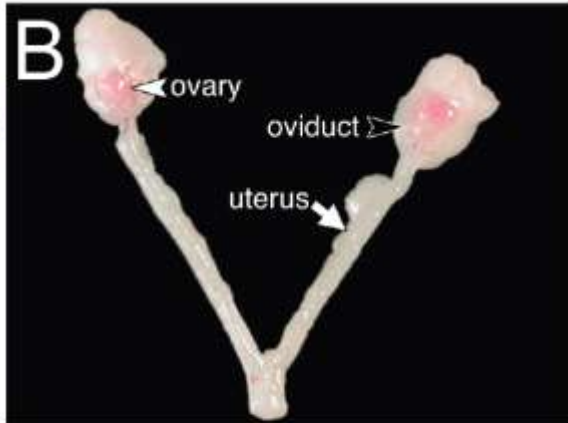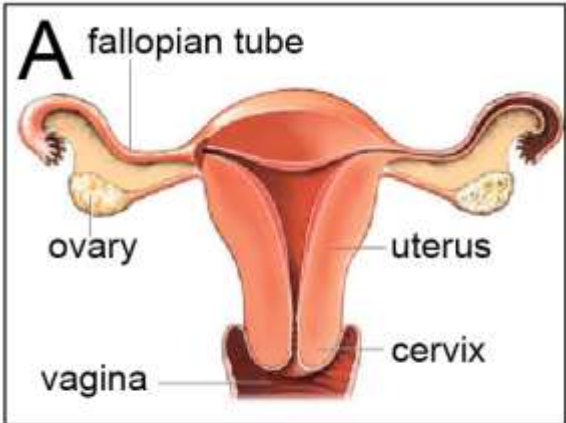
The FRT is a highly complex organ that contains multiple functional areas. During FRT development, various signaling pathways must work together to create a fully functional organ. In most mammals, the FRT is not completely developed at birth, instead it will transform from a partially compartmentalized tube into a highly patterned organ capable of ensuring the continuation of the species.

Estrous Cycle

The rise and fall of circulating hormones, especially estrogen (E2) and progesterone (P4) play a critical role in the preparation of the endometrium to receive the embryo. In mice, E2 induces proliferation of the uterine epithelium on day 1 of the estrous cycle. By day 3, P4 secreted from the corpus lutea results in proliferation of the stromal cells. On day 4, there is a spike in E2 that allows implantation of the embryo within the endometrium[14,15].

The endometrium undergoes a hormone-dependent cyclic wave of extensive proliferation to assure it will accommodate the fertilized embryos[16-18]. If fertilization does not take place, the endometrium undergoes abrupt apoptosis. The hormonally controlled process of regeneration followed by cell death is termed the estrous cycle, and it occurs in most mammals. Humans, primates (old world monkeys and apes), bats (phyllostomid and mollosid), and elephant shrews go through the menstrual cycle, where part of the endometrium in shed at the end of the cycle[19,20]. Female mice do not menstruate but instead go through

estrous cycle. The estrous cycle in mice lasts 4-5 days, if kept on a constant light-dark cycle. Generally, **proestrus** is considered to be the first phase of a new estrous cycle. During proestrus, mostly epithelial cells, and some stromal cells, proliferate while very few cells undergo apoptosis. During **estrus**, the females are considered to be in "heat" and if the conditions are right, oocytes will mature and be released where they will wait to be fertilized. If fertilization does not take place, **metestrus** ensues. During metestrus, a high number of cells in both the epithelium and stroma undergo apoptosis and are shed into the uterine cavity[18]. The endometrium then transitions into **diestrus**. During diestrus very few epithelial cells undergo cell division, while many stromal cells proliferate. The estrous cycle induces morphological changes in the uterus. During estrus, the uterus expands to almost triple its size during diestrus[18]. Maximal thickness and secretory activity of the uterine epithelium is observed during estrus[21]. Dysregulation of the estrous cycle can have dire consequences to the organism.

Diseases of the Female Reproductive Tract

Hormonal imbalance is the primary cause of female infertility. Additionally, studies have demonstrated that hormone treatments of an undeveloped FRT can lead to infertility[22] and disruption of normal uterine gland development[23]. Hormones, particularly estrogen, stimulate cell division and have been shown to promote endometrial cancer formation[24,25]. Most endometrial cancers of the female reproductive organs arise from the uterine epithelium[25]. In 2012, it is

7

estimated that 47,130 women will be diagnosed with endometrial cancer in the United States and 8,010 of these women will succumb to it[26]. **Adenocarcinoma** is the most prevalent type of endometrial cancer and arises from uncontrolled growth of the GE. Adenocarcinoma development occurs in stages[27]. The first stage is widely thought to be the manifestation of uterine lesions known as **endometrial hyperplasia**, subclassified into simple or complex. In simple hyperplasia, the uterine glands become cystically dilated, showing pseudostratified epithelium, while the stroma appears normal and contains small blood vessels uniformly spaced. In **complex hyperplasia** the uterine glands appear irregular in shape and size and often contain numerous side buds, while the stroma appears normal. Various studies have demonstrated that the presence of cytological atypia accompanying either simple or complex hyperplasia indicates progression to adenocarcinoma. In **Atypical hyperplasia,** glands lose the normal columnar epithelium morphology and the nucleus becomes rounder. Upon transition into adenocarcinoma, the glands are seen growing together with hardly any stroma observed between them. Silverberg calculated that the progression rate to adenocarcinoma is 4.3% from simple hyperplasia, 16.1% from complex hyperplasia, 7.4% from atypical simple hyperplasia, and 47% from atypical complex hyperplasia[27].

Endometrial polyposis is another type of endometrial lesion frequently diagnosed in women[28]. Endometrial polyps are described as benign growths that develop in the endometrium. The size of the polyps range from a few millimeters up to several centimeters. 20-25% of menopausal and postmenopausal women

will develop endometrial polyps[29]. Although mostly benign, endometrial polyps can transform into endometrial cancer[30]. The cellular morphology observed in histological samples obtained from endometrial polyps shows hyperplastic lesions, however, unlike in simple hyperplasia, polyps also display fibrotic stroma and thick-walled blood vessels. Treatment for endometrial polyps requires a minor operative hysteroscopy[31]. The polyps are identified and removed using a scope inserted through the vagina. Early discovery and removal is the key factor for treating endometrial polyps before they transform into endometrial cancer; therefore, understanding the molecular mechanisms that promote the transformation from benign lesions to cancer will assist with diagnosis and more effective treatment of endometrial cancers.

Both adenocarcinomas and endometrial polyps arise from a faulty genetic program in the GE, thought to be the result of unopposed estrogenic stimulation[32] (Giuntoli & Zacur, Endometrial hyperplasia, uptodate.com, 2011). Therefore, to fully understand the steps that are necessary for disease formation and development, it is important to understand the process of UG development.

Uterine Gland Development

Uterine glands are present in all studied mammals. Experiments in ewes and mice have revealed that females who lack UGs are infertile mainly due to impaired implantation and early pregnancy loss, suggesting that UGs are essential for fertility[33]. In humans, histotroph is thought to nourish the developing

fetus for the first trimester until the feto-placental network is established[34], yet, little is known about UG development and function.

UGs are an essential part of the uterine parenchyma, they secrete histotroph that aids implantation and nurtures the developing embryo. It is widely believed that the GE originates from the LE, the simple columnar epithelium that lines the uterine cavity. Extracellular signals, derived most likely from the stroma, induce epithelial cells to bud out from the LE and invaginate into the stroma, forming a tubular structure that later coil and branch[35]. Interestingly, in most mammals, even though the GE initially differentiates after birth, it only becomes fully differentiated as the female reaches sexual maturity. The uterine glands are known to secrete factors that are essential for proper embryo implantation, leukemia inhibiting factor (LIF) and calcitonin[36,37]. In mice, it has been reported that UG formation commences around postnatal day (P6) and is completed by P14[38]. UGs invaginate into the surrounding mesenchyme (stroma) forming a coiled tubular duct that opens to the lumen. In ewes and pigs, it has been observed that UGs branch as they extend into the stoma[39].

In many mammals, including mice, UGs develop after birth facilitating investigations of the cellular mechanisms that drive UG development, also termed **adenogenesis**.

Morphological Patterning of the Female Reproductive Tract

Like many forming organs, the Müllerian duct develops as a simple tubular structure composed of an inner epithelium surrounded by a mesenchyme[7]. Paracrine signals between the epithelium and mesenchyme, known as epithelial-mesenchymal crosstalk, are essential for proper formation and development of the FRT[40]. Orchestrated epithelial-mesenchymal interactions induce cell differentiation and establish membrane domains that set up cell polarity. Experiments have shown that the mesenchyme actively specifies which type of epithelium will develop[8,41].

The uterine epithelium is induced to adopt a columnar morphology, while both the vaginal and cervical epithelium, develops stratified morphology. In contrast with other organs, cytodifferentiation of the FRT is not completed until the female reaches sexual maturity. The uterus undergoes extensive remodeling during postnatal differentiation, increasing in both length and width, while expanding internally to accommodate such changes. At the same time, epithelial buds observed in the LE, are the nascent UGs. Initial budding is followed by invagination and formation of the main glandular duct. The initial formation of the UGs is similar to adenogenesis in many other organs. Therefore, I will introduce the cellular mechanisms that are known to play a role in the formation of glandular structures in other organs.

Tubulogenesis during UG Development

The formation of epithelial tubes is an evolutionary conserved process that is genetically programmed. It is widely thought that cells form tubular structures to increase surface area without having to increase in size, while at the same time decreasing the distance that molecules need to travel inside the organ. Tubulogenesis takes place during the formation of the neural tube, lung, kidney, gut, and FRT[42,43]. Studies in various organisms have elucidated some of the common genetic programs used to create such tubular structures (Figure 2). The principal signal likely required for tubulogenesis is acquisition of polarized epithelium[42,43]. There are tubes that develop from non-polarized epithelium packed together into a three-dimensional cluster that do not contain a lumen, however, after initial formation, cells acquire apical-basal polarity (Figure 2B).

Apical-basal polarity establishes cell compartments and membrane domains. The apical membrane faces the lumen while the basal membrane lies adjacent to the extracellular matrix (ECM). The formation of the baso-lateral domains is in part generated by E-Cadherin[44]. Canine kidney cells in suspension show a mixed distribution of apical-basal membrane proteins. E-cadherin localizes to the lateral membrane domain and promotes cell-cell contacts and generation of tight junctions. Other tight junction proteins localized to the lateral domain and create a partial paracellular seal. Once the epithelium forms a barrier, apical-basal polarity is established after ECM accumulates on one side of the cell. Polarized epithelium shows distinct cytoskeleton organization.

Figure 2: Models of tubulogenesis. (A) Invagination of a polarized epithelium. (B) Initial bud formation and subsequent formation of a glandular lumen in non-polarized cells. (C) Model of apical-driven epithelial invagination proposed by Sawyer, 2010. Adapted from Hogan et. al., Nature Reviews, 2002 and Sawyer, Developmental Biology, 2010.

A

B

Bud

Microlumen

Duct

Future
secretory
region

C
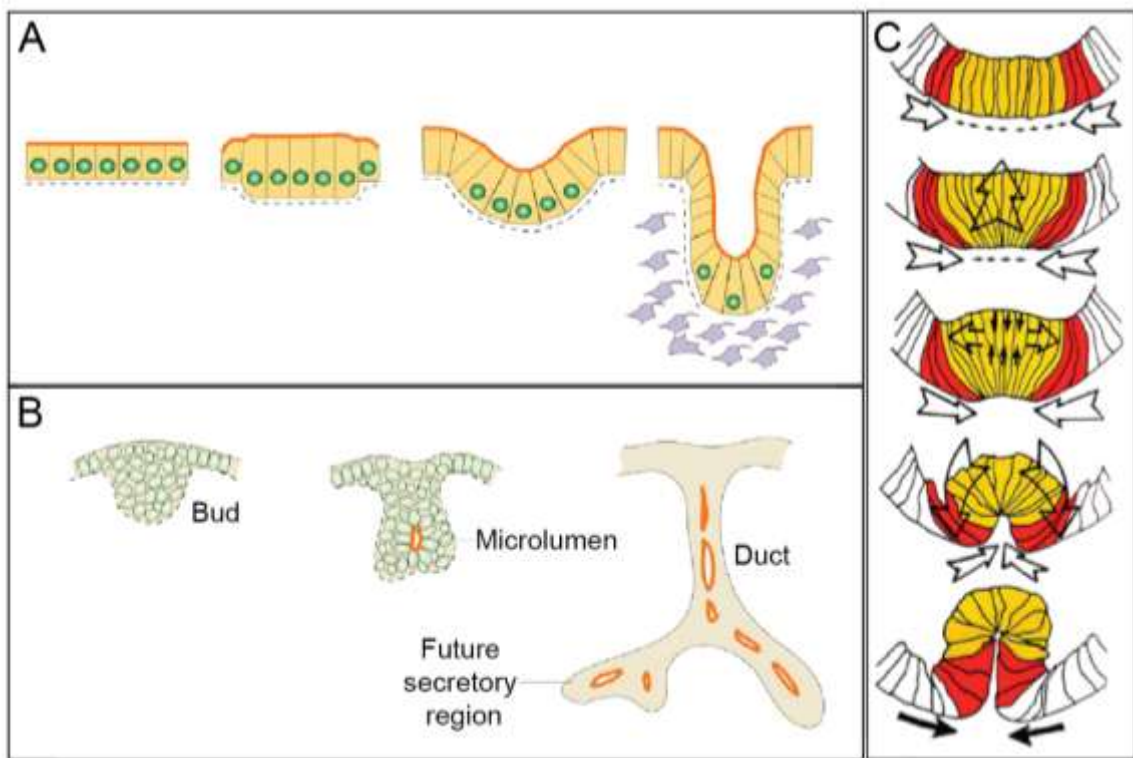
Cell-cell contact and cell-ECM contacts orient the cells. The apical domain usually is structurally and functionally different from the basal domain. This difference establishes the polarization that enables cells to transport ions and other factors across the epithelium.

Acquisition of cell polarity appears to be a requirement for proper tubulogenesis (Figure 2). Additionally there are other cellular mechanisms that play a role in tubulogenesis. To date, there are seven ways described to generate tubular structures in many animals[42]:

1- Wrapping: Epithelial sheet rolls up into a tubular structure as described during neural tube formation.

2- Budding: Spatial thickening of the polarized epithelial sheet followed by invagination. Branching morphogenesis often follows formation of a main tubular structure. Observed during lung, kidney, mammary gland and *Drosophila* salivary gland development.

3- Cavitation: Hollowing of a previously formed cylindrical structure by eliminating the cells in the center. Observed during mammalian salivary gland development.

4- Cord hollowing: Similar to cavitation, although cells migrate into the luminal walls instead of undergoing apoptosis. Observed during zebrafish gut development.

5- Cell hollowing: A single cell creates a lumen. Observed during *Drosophila* tracheal development.

6- Cell wrapping: Cells form a doughnut shape, attaching to themselves and thus forming a center where the lumen will eventually form. Observed during *C. elegans* digestive tract development.

7- Cell assembly: Two separated rows of cells first specify cell regional membrane domains; then both rows fuse together to form a tubular structure. Observed during *Drosophila* heart tube formation.

Here, I will focus my attention on **budding**, since it appears to be the primary cellular mechanism used during uterine adenogenesis. During budding, polarized epithelia invaginate into the stroma forming a tubular structure that will give rise to the main duct. The Müllerian duct itself forms from a tube that invaginates next to the Wolfian duct.

Salivary gland morphogenesis in *Drosophila* has been studied in great detail[45]. Here, signals from the neighboring cells trigger a differentiation program in some epithelial cells. Upon specification, the nuclei migrate basally while the apical membranes constrict. *Forkhead (fkh)* is known to regulate constriction of the apical membrane in the fly. In *fkh* mutants, the nuclei move basally, however, tubulogenesis is impaired due to failure of apical membrane constriction. Therefore, basal migration of the nuclei concomitant with apical membrane constriction seems to play an important role during tubulogenesis[46]. FOXA2, an orthologue of FKH, has been reported to regulate UG formation[47]. Mice, in which *Foxa2* was conditionally knocked out in the postnatal uterus, showed reduced numbers of UGs.

Glandular structures that arise from budding usually develop additional branches that stem off the main duct by subsequent epithelial invaginations. The morphological process of creating additional branches out of the main duct is termed **branching morphogenesis**.

Branching Morphogenesis

In mice and humans, there are conflicting reports when it comes to UG branching. In the lung, kidney and mammary glands branching morphogenesis has been well characterized[48]. During tubulogenesis, buds are formed on the main duct. Nascent buds extend out of the main duct forming primary branches, which themselves can further branch multiple times forming complex glandular structures. Branching morphogenesis takes place during UG development in pigs and sheep[49,50].

Several signaling pathways, particularly Wnt and Receptor Tyrosine Kinases, are known to play a role in branching morphogenesis[51-54]. In addition, there are various mutant mice that show developmental defects in uterine adenogenesis. Therefore, we can use them to create a picture of the molecular signals that may regulate UG development.

Molecular Pathways that Contribute to Uterine Gland Development

Creation of the main glandular duct requires multiple signaling pathways that establish apical-basal membrane domains, shape cell morphology for invagination, and regulate cell proliferation. Later, other signaling pathways are essential for the generation of glandular branching.

Several Wnt ligands are expressed in the developing and adult reproductive tract[55]. The *Wnt* genes encode secreted cysteine-rich glycoproteins that bind to seven-pass transmembrane receptors called Frizzled (Fz) and Lrp co-receptors and initiate a series of downstream events inside the cell[56]. In the canonical Wnt signaling pathway, Disheveled (DVL) becomes activated upon ligand binding to its respective receptor. Activation of DVL inactivates glycogen synthase kinase-3 (GSK3), a kinase that phosphorylates and targets β-catenin for degradation[57]. Cytoplasmic levels of β-catenin rise and subsequently translocate into the nucleus and form a heterodimer complex with transcription factor (TCF) or lymphoid enhancer-binding factor (LEF) binding proteins. β-Catenin/TCF/LEF complexes have been shown regulate genes involved in cell fate specification and proliferation. In the "noncanonical" *Wnt* signaling pathway, activation of the receptor by its specific ligand can either regulate downstream pathways that reorganize the cytoskeleton through actin and microtubular reorganization, or result in a surge of Ca^{2+} ions that activate other pathways.

Wnt4 is initially required for Müllerian duct formation[58]. Once the uterus is formed, conditional deletion of *Wnt4* leads to a reduction in the number of UGs.

In addition, loss of *Wnt4* disrupts tubulogenesis during renal tube formation[59]. Furthermore, in the mouse mammary gland, *Wnt4* is proposed to be a major inducer of glandular branching[53]. *Wnt5a* knockout mice lack the cervix and upper vagina, and show defects in adenogenesis[60]. *Wnt7a* knockouts lack UGs, and oviduct and they show a posteriorization of the uterine epithelium that becomes stratified epithelium similar to that found in the cervix and vagina[61]. *Wnt11* was shown to be required for ureteric bud branching morphogenesis[52]. Therefore Wnt signaling potentially regulates uterine adenogenesis by regulating the expression of genes that mediate tubulogenesis and branching morphogenesis.

Among the receptor tyrosine kinase (RTK) superfamily of signaling pathways, fibroblast growth factor (FGF) and epidermal growth factor (EGF) have been reported to regulate adenogenesis[62]. Binding of ligand to the receptor leads to a conformational shift that activates its intracellular kinase domain that subsequently induces multiple downstream signaling cascades that results in various biological responses, including proliferation, differentiation, migration and inhibition of apoptosis[63]. There are four FGF receptors (FGFR), and alternative splicing of the third immunoglobulin (Ig) domain controls the ligand-receptor specificity. Epithelial cells mostly express the b-splice variant (IIIb), while the c-splice form (IIIc) is usually found on mesenchymal cells. Mutations in *FGFR2* that encode for a receptor that is activated in the absent of the ligand have been found in a subset of endometrial cancers[64]. *Fgf7* and *Fgf10* regulate neonatal uterine development in sheep[62]. Moreover, in the ovine endometrium, *Fgf7* is expressed in the myometrium, while *Fgf10* is expressed in the stroma. They both

bind and activate FGFR2-IIIb, which is expressed in the LE and GE[65]. During lung formation *Fgf10* is expressed in the mesenchyme surrounding the growing epithelial branch tip, while *Fgfr2* is expressed in the epithelium and also the mammary epithelium as it invaginates[51,66,67]. Ex vivo studies of submandibular gland development determined that FGF7 functions as an autocrine signal that promotes budding, while FGF10 promotes elongation of the duct[54]. Both FGF7 and FGF10 downstream signals were shown to be mediated by ERK1/2. Therefore, FGF7, secreted from the myometrium, most likely promotes branching morphogenesis, while FGF10, secreted from the stroma regulates UG elongation.

Both Wnt and Fgf signaling regulate epithelial-mesenchymal interactions that induce cellular differentiation and specify morphological changes that play a key role during uterine development. Additional to the epithelial-mesenchymal interactions, circulating hormones secreted by the ovary and pituitary, exert a major influence on the endometrium.

The focus of this thesis is on the transcription factor SOX9. Our initial observation demonstrated that SOX9 was expressed in the UGs (Figure 3). Interestingly, SOX9 appears to be regulated by both Wnt and FGF pathways. During chondrocyte differentiation, SOX9 was reported to bind, phosphorylate and trigger degradation of β-Catenin[68]. Conversely, activated β-Catenin repressed *Sox9* transcription by inhibiting SF1 from binding to the testis-specific enhancer of *SOX9* core (*TESCO)* region[69]. In the intestinal epithelium, *Sox9* is activated by the β-Catenin-TCF4 complex[70].

Figure 3: SOX9 is expressed in the uterine glands of both mice and women.

Immunofluorescent staining performed using α-SOX9 antibody. (A) Adult mouse uterus expresses SOX9 (green) mostly in the GE. (B) SOX9 is present in the human uterine glands. SOX9, green; DAPI, blue; GE, glandular epithelium; LE, luminal epithelium.
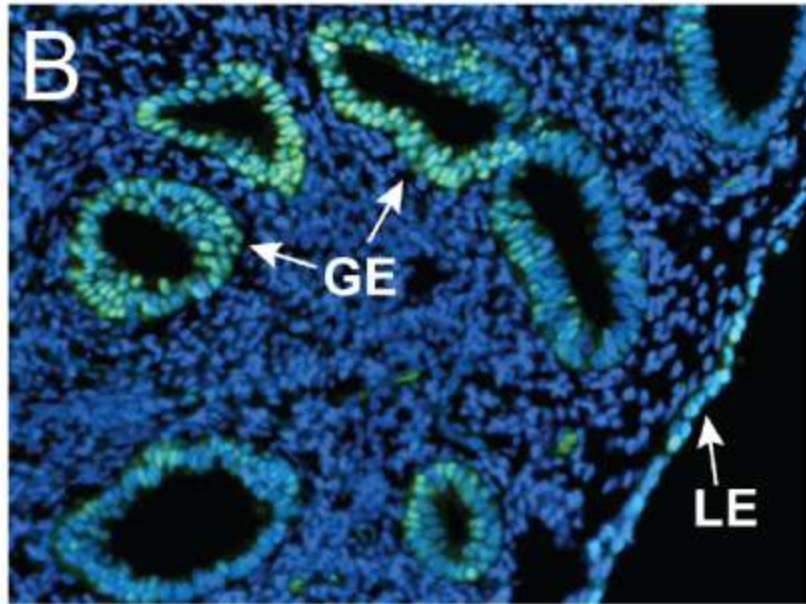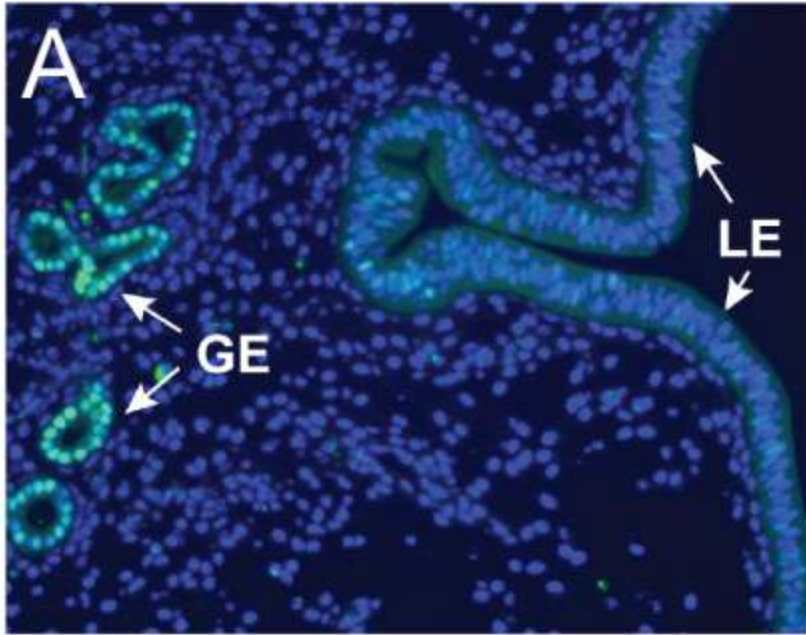
Therefore, it appears that β-Catenin can both repress and activate *Sox9*, while SOX9 seems to promote β-Catenin degradation. *Sox9* was shown to be upregulated by RTK activation[71]. Specifically, binding of FGF9 to FGFR2 can activate *Sox9* transcription[72]. Moreover, a recent study demonstrated that *Sox9* expression was specifically induced by EGFR activation through the MEK/ERK pathway[73]. Thus, it appears that both pathways converge onto SOX9 in certain tissues.

SOX Gene Family

SOX9 is part of the Sry (sex determination region Y)- related HMG box (SOX) family. The *SOX* genes are critical in multiple developmental and physiological processes[74]. Members of the SOX family contain a conserved high mobility group (HMG) DNA binding domain. There are 22 known SOX genes in both humans and mice, which are subdivided into 9 subgroups (A, B1, B2, C, D, E, F, G, H)[74]. *SOX9* is part of the SOXE subgroup, along with *Sox8* and *Sox10*. These genes share a very conserved amino acid sequence in the HMG domain and a transactivation domain at the N-terminus. SoxE genes appear to have duplicated early during evolution since they have been detected in lampreys[75]. It appears that over time the SOXE genes have acquired other important roles in the development of many organs. *Sox9* mutant mice die early during embryogenesis[76], while *Sox10* mutants show defects in neural crest differentiation[77]. *Sox8* mutant mice are viable and show no detectable phenotypic

abnormality, which is thought to be in part to a shared functional redundancy between all three members of the SOXE group[78]. All three members seem to have overlapping spatio-temporal expression patterns during development. For example, *Sox9* is highly expressed initially during embryonic development of the pancreas and *Sox8* and *Sox10* appear to be also expressed although a low levels[79].

In humans, mutations in *SOX9* result in Campomelic Dysplasia, a disorder associated with bowing of the bones and male to female sex-reversal[80]. *Sox9* is required for the condensation of the mesenchyme that differentiates into chondrocytes[81]. SOX9 regulates *Col2a1*, *Col11a2*, *Col9a1*, *Aggrecan*, and *Cartilage link protein*[82-86]. In mammalian males, *Sox9* is expressed right after *Sry* and is essential in testis formation[87]. Immunofluorescent staining revealed that SOX9 is present in the mouse uterine epithelium, but appeared to be concentrated in the nuclei of the GE (Figure 3A). Moreover, human endometrial samples also express nuclear SOX9 in the GE (Figure 3B). These observations suggest a role for SOX9 in the LE and GE and the overall hypothesis of this thesis.

Hypothesis

SOX9 is required for uterine gland development and/or differentiation

Chapter II: Three-Dimensional Visualization of the Female Reproductive Tract

Introduction

The function of the FRT is to protect and nurture the developing embryo inside the mother. In the mouse, the blastocyst implants and develops on the antimesometrial side of the uterus. UGs are an essential part of the uterine parenchyma, they secrete histotroph that is required for implantation and provides nutrients to the developing embryo. In humans, histotroph is thought to nourish the developing fetus for the first trimester until the feto-placental network is established[34]. UGs are present in all studied mammals.

In mice, UG formation initiates around postnatal day (P6) and is complete by P14[38]. This process is termed **adenogenesis**. UGs invaginate into the surrounding mesenchyme (stroma) forming a coiled tubular duct that is open to the lumen. During tubulogenesis, buds are formed on the main duct. Nascent buds extend out of the main duct forming primary branches, which themselves can further branch multiple times forming complex glandular structures. In ewes and pigs, it has been observed that UGs branch as they extend into the stoma[39]. In mice and humans, there are conflicting reports regarding UG branching. To date, little is known of about the three-dimensional (3D) structure of the UGs. The UGs are relatively small and the dense muscle layers that surround the endometrium makes it difficult to visualize their structure. In the past, various

artistic renderings of the UGs have been generated based on histological sections and 3D reconstructions[88]. However, this is very tedious and time consuming, making a comprehensive analysis of UG formation and structure difficult.

In our lab, we are actively searching for novel ways to visualize organ development and differentiation to uncover cell behaviors and understand how cells become organized to form complex structures[89,90]. We have created 3D models of fetal mouse testicular cords during development by compiling multiple Z-stacks images[91]. Computer generated (CG) models have enabled us to visualize structures that are not easily detected in histological sections. To elucidate the 3D structure of the UGs, we performed whole mount immunofluorescent staining using α-E-Cadherin antibody to mark fluorescently the entire uterine epithelium. By collaborating with Dr. Jichao Chen (M.D. Anderson Cancer Center), we used **optical projection tomography** (OPT) to create CG 3D-replicas of the structural framework of the epithelium in the FRT. This allowed us to visualize UG structure and position in the uterus.

To create detailed 3D replica of UGs at the cellular level, we devised a genetic strategy to mark the UGs. Since our initial finding indicated that SOX9 was expressed in the GE, we mated *Sox9-Cre* mice[92] to *Rosa-26-Reporter--H$_2$B-mCherry-EGFP-GPI (R26R-RG)* mice[93] to mark fluorescently the GE. By using this genetic strategy we were able to express mCherry fluorescent protein-conjugated to histone H$_2$B, allowing us to mark GE nuclei. This fluorescent protein was visualized using confocal microscopy. By generating multiple Z-stack

images we were able to recreate the 3D structure of the UGs at cellular resolution.

Material and Methods

Mice

Rosa-26 Reporter-H$_2$B-mCherry-EGFP-GPI (R26R-RG)[93] and *Sox9-Cre*[92] mice were generously provided by Dr. Haruhiko Akiyama (Kyoto University). All mice were maintained on a C57BL/6J x 129/SvEv mixed genetic background. All animals were maintained in compliance with the Public Health Service Policy on Humane Care and Use of Laboratory Animals, the U.S. Department of Health and Humane Services Guide for the Care and Use of Laboratory Animals, and the United States Department of Agriculture Animal Welfare Act. All protocols were pre-approved by the University of Texas M.D. Anderson Cancer Center Institutional Animal Care and Use Committee.

Polymerase Chain Reaction

DNA was extracted from the tip of the tail. Tails were placed in 1.5 ml microcentrifuge tubes containing 300 μl of tail digestion buffer (10 mM Tris pH 8, 5 mM EDTA pH 8, 0.1 M NaCl, 1% SDS), 5 μl of a 40 mg/ml Proteinase K solution was added to the tube and placed in a 65°C bath overnight. The next

day the tubes were mixed, 250 µl of phenol/chloroform added and vortexed again. The tubes were centrifuged at 13,200 revolutions per minute (rpm) for 10 minutes in a microcentrifuge (Eppendorf, 5415D). 300 µl of the supernatant was transferred into a clean 1.5 ml microcentrifuge tube. 300 µl of 100% isopropanol was added and mixed well to precipitate DNA and centrifuged at 13,200 rpm for 10 minutes. The supernatant was carefully decanted and 300 µl of 70% ethanol was added to the tube to wash off remaining salts from the DNA pellet. The tubes were centrifuged at 13,200 rpm for 2 minutes. The supernatant was decanted and the tubes were placed upside-down on the bench to air dry. Once dried 100 µl of TE (10 mM Tris pH 8, 1 mM EDTA pH 8) buffer was added to dissolve the DNA. DNA concentration was calculated using a NanoDrop Spectrophotometer.

For each 20 µl PCR reaction, we mixed 100 ng of tail DNA, 0.5 µl of 10 mM dNTPs (250 µM total or 62.5 µM each), 0.5 µl of 10 mM of each forward and reverse primer (250 µM), 2 µl of Gene Choice (#608607) 10x Standard Buffer (1.5 mM MgCl$_2$ final), 0.2 µl of Gene Choice (#608601) DNA Taq polymerase (1 unit). We added water to fill a 20 µl final volume. We used a Bio-Rad DNA engine peltier thermal cycler to amplify the region of interest.

Cre primers: (*Sox9-Cre)*

Cre forward: 5' GGACATGTTCAGGGATCGCCAGGC 3'

Cre reverse: 5' CGACGATGAAGCATGTTTAGCTG 3'

PCR was performed with a 95°C denaturing step for 5 minutes, followed by a second 95°C denature for 30 seconds, a 57°C annealing step for 45 seconds and a 72°C elongation step for 45 seconds. Steps 2-4 were cycled 30 times. Lastly, a final incubation of 72°C for 5 minutes allowed complete elongation of the region of interest. Using Cre forward and reverse primers, we detected a 219 bp Cre DNA product in a 1.5% agarose gel.

GFP primers (*R26R-RG)*:

GFP forward: 5' ACCCTGAAGTTCATCTGCACCACCG 3'

GFP reverse: 5'-CGTCGTCCTTGAAGAAGATGGTGCG3'

PCR was performed with a 95°C denaturing step for 5 minutes, followed by a second 95°C denature for 30 seconds, a 57°C annealing step for 45 seconds and a 72°C elongation step for 45 seconds. Steps 2-4 were cycled 30 times. Lastly, a final incubation of 72°C for 5 minutes allowed complete elongation of the region of interest. Using Cre forward and reverse primers, we detected a 173 bp DNA product in a 1.5% agarose gel.

The PCR products were mixed with loading buffer (Bromophenol Blue Sucrose Solution, 0.25% w/v bromophenol blue, 40% w/v sucrose) and placed into a well in a 1.5% agarose gel (Agarose HS-Denville Scientific Inc.) containing ethidium bromide (10 mg/ml, FisherBiotech, BP102-5). The agarose gel was run for 30 minutes at 100 Volts (~ 400 mA) and later analyzed using an ultraviolet

lamp. On each run, a 100 base pair DNA ladder (Invitrogen, cat# 15628-050) was used as a marker to assess band size.

Whole Mount Immunofluorescence

The samples were processed following a protocol generously provided by Dr. Allison Stewart (M.D. Anderson Cancer Center). FRTs were dissected and fixed overnight in 4% Paraformaldehyde (PFA) (Electron Microscopy Sciences, cat#19210) at 4°C. The next day, the tissues were washed twice for 30 minutes in cold PBS. Later, the tissues were dehydrated using sequential methanol dehydration steps (25% MeOH, 50% MeOH, 75% MeOH, 100% MeOH) by leaving them 10 minutes at 4°C during each step. Once dehydrated, the tissues were transferred into a MeOH/ 30% H_2O_2 (4:1) solution overnight at 4°C to bleach the tissues. H_2O_2 is usually used to block endogenous peroxidase activity, however, Dr. Jichao Chen (M.D. Anderson Cancer Center) recommended we perform this additional step to better clear the samples. The tissues were rehydrated by reversing the dehydration steps and then were transferred into blocking solution (1% BSA, 11% Sucrose, in PBS) for 5 minutes, 3 times. Rat α-mouse-E-Cadherin (Invitrogen, Cat# 131900) (1:100) was added to the last blocking solution and the tissues were left rocking overnight at 4°C. The next day, the tissues were washed 3 times for 5 minutes in PBS. The tissues were transferred into blocking solution containing the secondary antibody (AlexaFluor 546, Cat# A11081) (1:200). The tissues were placed in a brown glass vial to

reduce light exposure. The next day, the tissues were washed 3 times for 2 hours in PBS. The tissues were dehydrated following sequential steps described earlier. The tissues were transferred into a MeOH: BABB (1:2 benzyl alcohol (Sigma-Aldrich, Cat# B2263)/ benzyl benzoate (Sigma-Aldrich, Cat# W213810) (1:1) for 1 hour. Later, the tissues were transferred into BABB and left overnight at 4°C. This cleared the tissue and allowed us to determine if the antibody had labeled the epithelium of the FRT. The tissues were then transferred into MeOH/ BABB (1:1) for 1 hour and later transferred into 100% MeOH and left overnight at 4°C. The samples were delivered to Dr. Jichao Chen for OPT imaging.

Clearing the FRT using ScaleA2

We dissected FRT from *Sox9-RG* females and placed them in 4% PFA overnight. The next day, the tissues were washed 3 times in PBS for 15 minutes. The tissues were transferred into a 15 ml conical tube containing ScaleA2[94] (4M Urea, 10% Glycerol, 0.1% Triton X-100) solution and left for four days at 4°C. After the tissues were cleared in ScaleA2 solution, the fluorescent proteins were viewed by fluorescent microscopy.

Immunofluorescent Staining

FRTs were dissected and placed in 15 ml conical tubes containing 4% PFA and wrapped with aluminum foil to reduce light exposure. The next day, the

tissues were washed twice for 30 minutes in cold PBS. Later, the PBS was discarded and replaced with a 15% sucrose solution and left until the tissues sank to the bottom of the tube. The previous step was repeated using a 30% sucrose solution. The sucrose was discarded and replaced with a 30% sucrose/ OCT compound (FisherScientific, Cat# 14-373-65) (1:1) solution and left for 1 hour at 4ºC. The tissues were embedded and frozen in OCT on top of dry ice.

Frozen blocks were sectioned using a Cryostat. The thickness of the sections varied from 20 - 80 µm. The tissue sections were placed on a slide and air dried for 5 minutes. The slides were placed inside a Coplin staining jar containing cold acetone for 5 minutes. The slides were transferred into another Coplin staining glass containing 1% Triton X-100 in PBS and left for 10 minutes. The slides were tapped on a flat surface to remove excess PBS and 100 µl of Phalloidin (1:20) was added on top of the tissue sections. The tissue sections were incubated with Phalloidin for 30 minutes. The tissue sections were washed twice with PBS for 10 minutes. DAPI with Vectashield was added on top of the tissue sections and covered with a coverslip.

Results

Generating 3D Replicas of the Female Reproductive Tract Using Optical Projection Tomography

We used OPT to create CG 3D-replicas of the epithelium of the FRT. A caveat of using OPT is that the samples must be small enough to fit in a cylinder with a diameter of around a centimeter. Therefore, for our initial experiment we used P11 FRTs. We performed whole mount immunofluorescent staining using α-E-Cadherin antibody to label the uterine epithelium. Using fluorescent microscopy, we confirmed that the epithelium of the FRT was stained before analyzing the samples using the OPT machine. After the sample was analyzed and all the optical sections were compiled into one large file, we used the Imaris software to generate a CG 3D-replica of the FRT (Figure 4).

Using the Imaris software, we enhanced the background signal to visualize the surface of the FRT (Figure 4A). An optical section along the longitudinal axis of the FRT showed the difference between the marked epithelium and the background signal (Figure 4B). Inside the uterus, we could discern multiple UGs present along the entire length of the uterine horn. By removing the background signal we were able to observe that UGs extend radially on the ventral (antimesometrial) side of the uterus (Figure 4C, D). At P11, the UGs extend out from the LE as simple cylindrical tubes. No UGs were present on the mesometrial side of the uterus.

Figure 4: OPT imaging of the FRT at P11. (A) The surface of the entire FRT, composed of ovary (ov), oviduct (ovd), and uterus (ut), is shown by enhancing the background signal. (B-D) The epithelium lining the FRT marked by wholemount immunofluorescent staining using an α-E-Cadherin antibody. (B) An optical longitudinal section with enhanced background signal shows the uterine epithelium (red) lining the inside of the oviduct and uterus. (C, D) Images of the epithelium of the oviduct (above) and uterus (below). Black arrows point to a novel structure discovered in the mouse uterus, the uterine rail. A, anterior; P, posterior; D, dorsal; V, ventral.
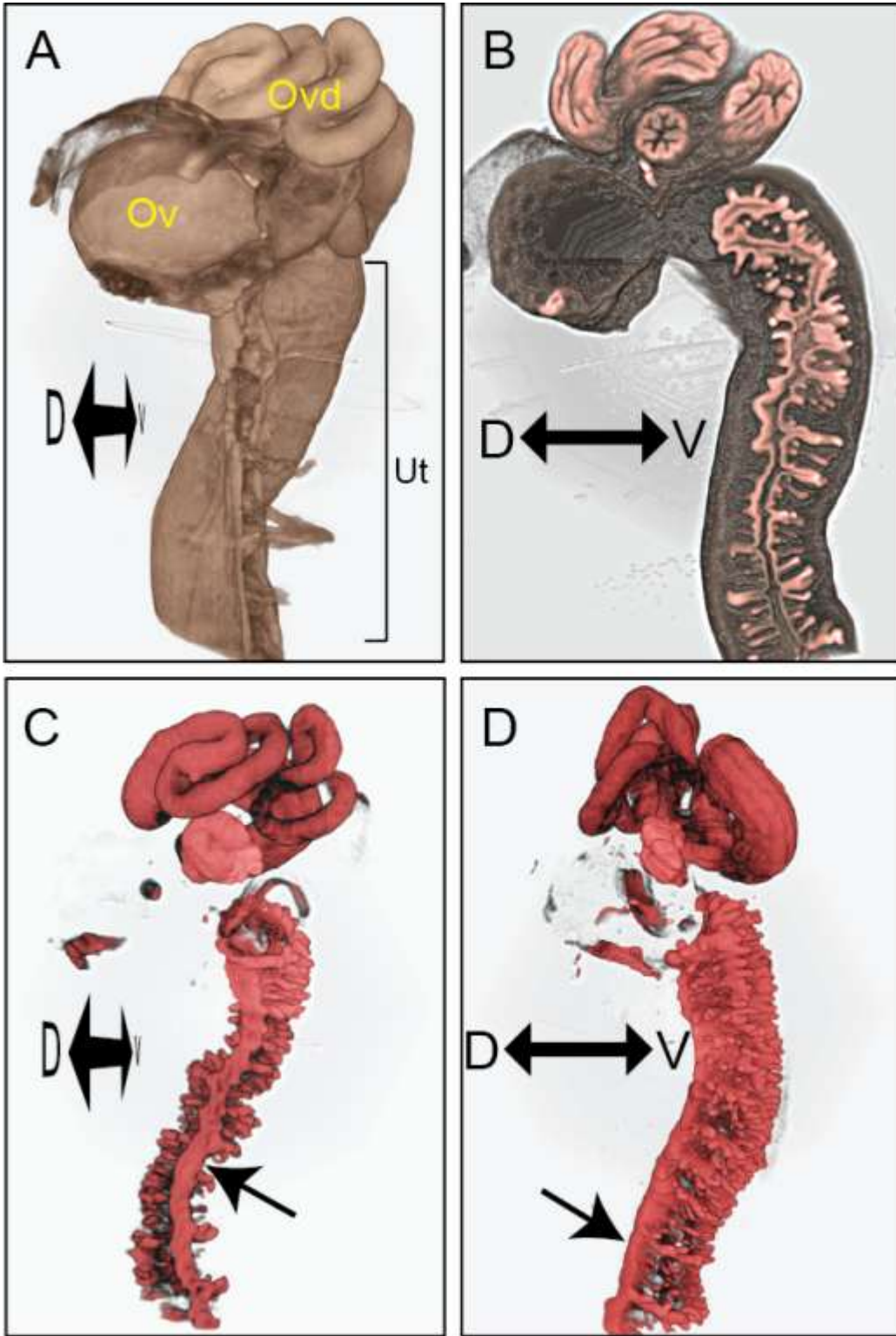
We created an optical cross section of the uterus and enhanced the background to show that if one divides the uterine cavity into four sections (I, II, III, IV), along the mesometrial to antimesometrial axis, the first section (I), closest to the mesometrial side, is for the most part devoid of UGs (Figure 5A). Most UGs can be observed on the antimesometrial side (sections III & IV) of the uterus, the site of embryo implantation.

Surprisingly, we detected a prominent structure that has not been described in the literature (Figure 4, arrowheads, Figure 5, flanked by yellow lines). The LE closest to the mesometrial side of the uterus appears to have a unique structure along the length of the uterine horn. By remaining fixed along the anterior-posterior axis, the epithelium on the mesometrial side forms a structure that resembles a handrail, so we decided to name this dorsal structure the "uterine rail". If we trace an imaginary circle along the dorsal-ventral axis, where the mesometrial side lies at zero degrees, the uterine rail appears to extend 20-30 degrees laterally (40-60 degrees total) from the middle of the uterine lumen, creating a U-shaped epithelium that resembles a hand rail or chef's hat and comprises ~15% of the circumference of an imaginary circle tracing the endometrium (Figure 5B). Identification of the uterine rail in 3D images facilitated seeing this structure in uterine histological cross-sections when the mesometrial-antimesometrial orientation is positioned dorsal-ventral.

Generating 3D Images of Uterine Glands at Cellular Resolution by Confocal Microscopy

The main focus of my research is to study UG development. Using OPT, we were able to demarcate the entire epithelium of the FRT, although at poor cellular resolution. To create a CG replica of the UGs at cellular resolution, we took advantage of the high-resolution quality obtained by using confocal microscopy. We found that SOX9 is expressed in most of the GE and some of the LE, which will be discussed later. Therefore, we generated *Sox9-Cre; Rosa 26 Reporter-H_2B-mCherry-EGFP-GPI (Sox9-RG)* mice to mark cells derived from SOX9 expressing epithelium, anticipating that most of the GE would be labeled with the fluorescent proteins (FP). Upon Cre-mediated activation of the *Rosa 26* allele, cells expressing *Sox9* also turned on expression of a red fluorescent protein (mCherry) conjugated to histone H_2B and a green fluorescent protein (GFP) that attaches to the cell membrane.

By using *Sox9-RG* mice, I cannot assert that all cells that expressed the FPs were expressing *Sox9* at the time of dissection. Instead, the cells showing a positive signal were either expressing *Sox9* or were derived from a parental cell that had expressed *Sox9* previously. Thus, I shall refer to the cells showing FP signal Sox9-lineage positive (Sox9-LP) cells.

Although, later I will describe in more detail the observations we made using the *Sox9-RG* mice, in this section I will describe our initial findings for adult tissues.

Figure 5: Visualizing the structure of the uterine epithelium at P11. (A, B) Optical cross-section of the mouse uterus stained with α-E-Cadherin antibody (red) with enhanced background signal. (A) The uterine lumen is divided into four sections to display the presence or absence of UGs between dorsal (mesometrial) and ventral (antimesometrial) side. (B) The uterine rail is present within ~50° from the middle of the uterine cavity forming a structure that resembles a hand rail or a chef's hat. (C) Imaging to only show the epithelium of the uterus. UGs extend radially within the ventral side of the uterus. (D) View from the dorsal side to show the uterine rail delineated by yellow dashed lines. UG, uterine glands.
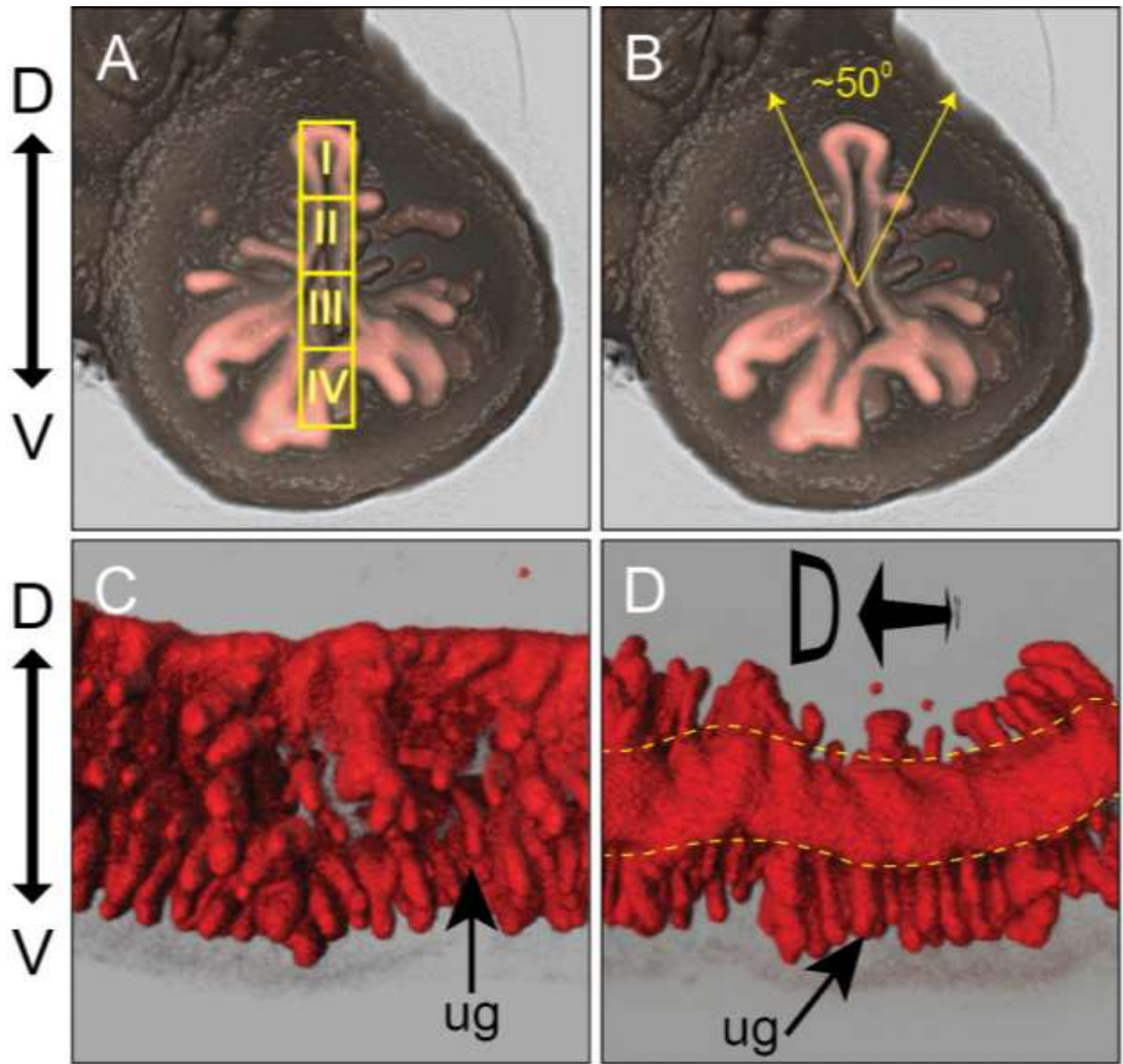
The uteri of 8-week-old females were dissected, fixed, and frozen to prevent the leaking of the FPs from the cell. To quickly assess the 3D structure of the UG, we placed a few of the uteri in a ScaleA2[94]. This solution decreases the background noise, allowing us to view the fluorescent signal present in the nuclei of SOX9-LP cells. We were able to visualize the structure of the UGs. Adult UGs featured a main duct with primary buds or branches (Figure 6B). The images clearly show that branching morphogenesis takes place in the development of the mouse UGs. However, the resolution was not high enough to create high-resolution CG 3D replicas.

To generate a CG 3D replica of the UGs, we sectioned frozen uteri of *Sox9-RG* females at 60 μm. Using confocal microscopy, we took multiple Z-stack images of these tissue sections. We were able to detect the mCherry inside the nuclei of Sox9-LP cells using low laser power. The GFP was not as easy to detect. In fact, in order to detect the GFP, the laser power had to be turned up very high, which then caused the detectors to pick up autofluorescent signals from the tissue.

Using *Sox9-RG* females, we were able to generate the first 3D CG replica of UGs at cellular resolution (Figure 6C-G). We observed that the lumens of the branches connect to the main ductal lumen (Figure 6E, G). Various primary branches are present as small round structures (Figure 6D, E) and as longer cylinder-shaped buds (Figure 6F, G) that stem from the main duct. Additionally, we noticed that the circumference of each bud was made up of roughly the same number of cells, approximately 12 cells (Figure 6E, G).

Figure 6: Visualization of the adult uterine glands at cellular resolution in Sox9-RG mice. (A) Genetic strategy used to express a red fluorescent protein conjugated to histone H_2B in the nuclei of UGs. (B) UG visualized by confocal fluorescent microscopy (C-G) 3D images of UGs generated by reconstructing Z-stack images taken using confocal microscopy. (C) Uterine sections; nuclei of SOX9-LP cells (red) and all nuclei stained by DAPI (blue). (D) The signal detected from the blue channel (DAPI) was removed to show only nuclei of SOX9-LP cells. (E) Magnified image from D (box) used to count the number of cells in the circumference of the glandular buds. (F) Nuclei of SOX9-LPs in UGs. (G) Magnified image from F of the UG showing the number of cells making up the circumference of the primary branches is maintained as they lengthen from the main glandular duct. GE, glandular epithelium; LE, luminal epithelium.
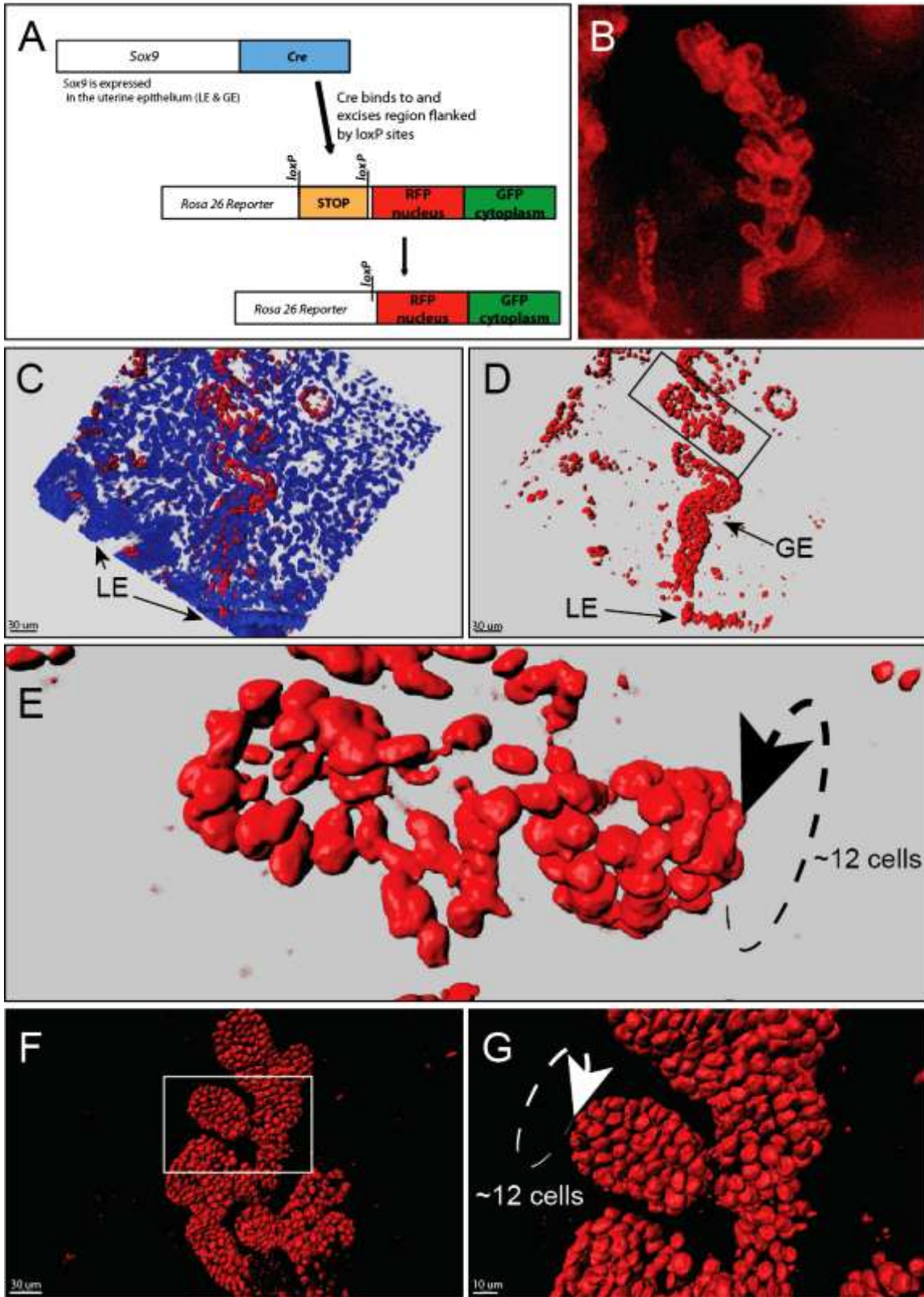
Figure 7: Model of uterine gland development. Uterine glands develop as simple ducts, which later form primary branches that elongate from the main duct.

Postnatal day 11 → Adult
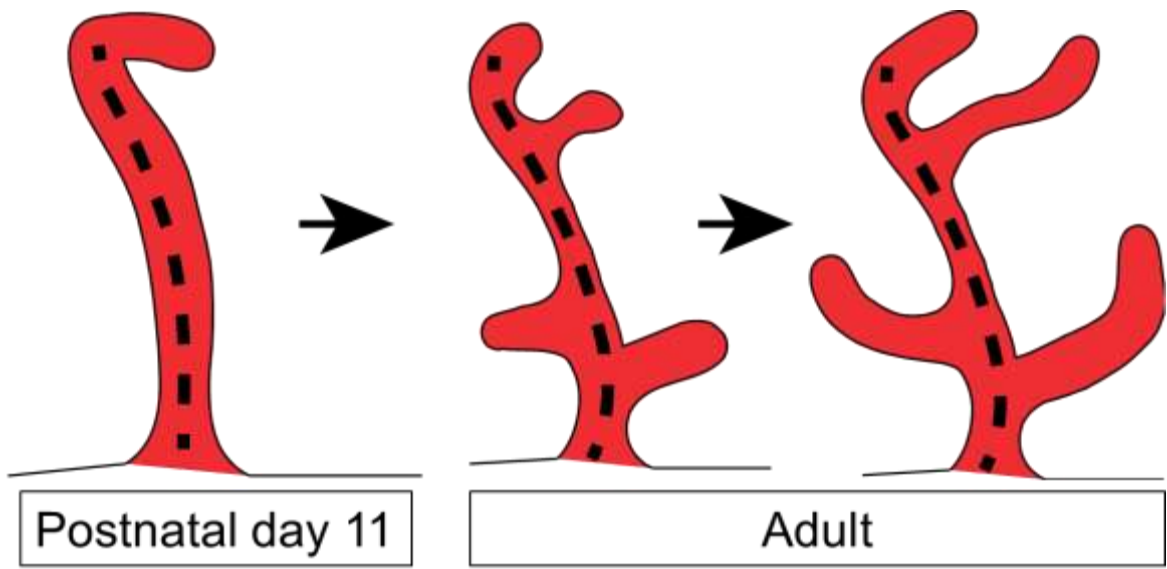
Therefore, it appears that primary branches initially develop as round structures containing a lumen that subsequently lengthen from the main glandular duct as cylinder-like structures (Figure 7).

Discussion

Whole mount immunofluorescence followed by OPT imaging allowed us to create 3D replicas of the epithelium lining the mouse FRT at P11. We observed UGs present along the entire uterine horn. UGs are exocrine glands that secrete histotroph into their lumen, which is transported into the uterine cavity[4]. Histologically, UGs are classified as simple tubular glands[39]. In simple glands the main duct remains unbranched, while the secretory portion attached to the duct can itself branch[95]. Conversely, in compound glands, the ducts branch to accommodate more secretory units. In the uterus of pigs, sheep and mice, the main glandular duct forms postnatally, while branching morphogenesis is only thought to take place in pigs and sheep[39]. Therefore, histologically the UGs of pigs and sheep are considered simple branched tubular, while mouse UGs are considered as simple tubular (unbranched). At P11, we observed that UGs were present as simple tubular (unbranched) structures; however, examination at later time-points revealed that UGs develop into simple branched tubular structures.

OPT imaging also allowed us to visualize the 3D structure of the oviductal epithelium. The oviduct is composed of three subcompartments: the infundibulum, the ampulla and the isthmus[1,8]. The twists and coils present in the

oviduct make it difficult to accurately measure the length grossly. Moreover, a thin membrane is attached to the coiled oviduct which needs to be cut before the oviduct can be stretched for accurate measuring. A 3D replica of the mouse oviduct will allow us to accurately measure the difference in length and width between each of the subcompartments that make up the oviduct.

OPT imaging allowed us to detect a novel structure, the uterine rail. This structure is present at the mesometrial (dorsal) side of the mouse uterine horn. By generating digital cross sections of the uterine horn, we were able to determine that the uterine epithelium on the mesometrial side expands laterally forming the uterine rail. This structure resembled a chef's hat. Moreover, UGs were not present near the uterine rail at P11. In the future, we would like to visualize adult FRTs using OPT imaging to determine the structure of the uterine rail in the adult uterus. From what we can appreciate in the 3D replicas of the FRT at P11, this structure possibly functions as a frame that confers support to the uterus. It would be interesting to uncover if this structure is present in other mammals with bicornuate uteri. Additionally, we are would like to identify mutant mouse lines that lack this structure, to gather more information about its function.

By reconstructing mouse uterine sections, a previous study had shown that UG were mostly distributed on the antimesometrial side of the uterus[88]. Our 3D replicas confirmed these findings and also show that the UGs extend radially on the antimesometrial side. These observations suggest that there may be a morphogenic gradient in the mouse uterus that forms this mesometrial-antimesometrial difference[96]. Morphogenic gradients control evolutionary

conserved signaling pathways that regulate tissue patterning[96]. Perhaps, secreted molecules from the antimesometrial side are creating a morphogenic gradient that promotes UG development. Alternatively, secreted molecules from the mesometrial side could be actively preventing UG development.

By confocal microscopy, we were able to visualize multiple secretory units in adult mouse UGs. This observation contrasted with what was known about mouse UGs[39]. Histologically, exocrine glands are categorized into simple or compound[95]. In the mouse lung, kidney and mammary glands, tubulogenesis is followed by branching morphogenesis which leads to the branching of the main duct and formation of multiple secretory units in each duct[48]. We analyzed the structural framework of several UGs (n=17) at cellular resolution. These samples revealed for the most part, UGs are composed of one main duct with multiple secretory units. Occasionally, we observed two UGs that appeared to meet near the uterine cavity, which would make them compound; however, for the most part, UGs were observed as simple branched ducts.

The secretory portion of exocrine glands can be tubular (cylindrically-shaped) or acinar (sac-like)[95]. We observed that the secretory units were cylindrical-shaped. Moreover, we counted the number of nuclei around the circumference of the secretory units. We estimated that the circumference of each secretory unit was composed of 12-14 cells. Quantification of the cells of UGs in the future will contribute to an understanding of the cellular mechanisms that lead to their development, e.g. number of cell doublings.

In other organs, the secretory portions can themselves be unbranched or branched. Our findings indicate that at P11, mouse UGs are unbranched, however, multiple secretory units branch from the main duct. These, secretory units, for the most part, do not branch. The observation that most UGs appeared as single tubes at P11 (n=1) and that all adult uteri examined contained UGs that were branched suggests that branching morphogenesis in mice takes place sometime after P11.

In adult mouse UGs we observed that UGs were branched. The next step will be to create a detailed-timeline of UG branching morphogenesis. Using *Sox9-RG* mice, we could potentially collect multiple samples at various time points to determine when branching morphogenesis takes place in mouse UGs. Furthermore, advances in cell culturing techniques are allowing us to visualize how tissue morphogenesis takes place in vitro[97]. In the future, we would like to culture GE using in vitro culturing systems that mimic the 3D matrix found in the uterus. The methods used to isolate and grow mouse uterine epithelium in vitro have already been determined[98]. Therefore, culturing uterine epithelium prior to glandular differentiation will allow us to visualize budding, tubulogenesis and branching morphogenesis. Moreover, in vitro culturing will enable us to study the molecular pathways that induce bud outgrowth in UGs.

Chapter III: Uterine Epithelial Knockout of *Sox9*

Introduction

UGs secrete factors essential for embryo implantation and development[4]. In mice, UGs initially develop around P6 and are differentiated by P14[39]. The cellular mechanisms that promote invagination of the uterine epithelium, subsequent tubulogenesis, and glandular differentiation is still poorly understood[39]. In this thesis, we focus on the role of SOX9 in UG development. Our initial observation indicated that SOX9 was expressed mainly in the UGs (Figure 3). Moreover, SOX9 was localized inside the nucleus of the GE, the cells that compose the UGs. SOX9 is a transcription factor essential for embryo development and correlated with disease progression[99]. SOX9 expression is essential for proper differentiation of the prostate epithelium[100]. *Sox9* is also expressed in lung epithelia during organogenesis; however, mice in which this gene was conditionally inactivated were phenotypically normal[101]. To elucidate the role of SOX9 in the UGs, we decided to determine the spatio-temporal expression of SOX9 during FRT development and UG differentiation.

Furthermore, we conditionally inactivated *Sox9* in the uterine epithelium to determine its role in UGs development. *Sox9* mutant mice die early during embryogenesis[76] and *Sox9* heterozygotes die soon after birth[102]. Therefore, to analyze the function of SOX9 in UG development and differentiation we required a genetic strategy to conditionally inactivate *Sox9* in the uterine epithelium. We

used the progesterone receptor (*Pgr*) promoter to conditionally inactivate *Sox9* in the uterine epithelium. Although this was the best tool available, one potential pitfall was that *Sox9* would be inactivated after the UGs had formed. Additionally, SOX8, SOX9, and SOX10 have known compensatory roles during testicular development and neural crest differentiation[78,103,104].

Cre/lox System

The Cre/lox system is a genetic tool mostly used to conditionally knock out a specific sequence in a specific cell type. Usually, *loxP* sites are inserted flanking an essential exon of the gene of interest, which upon recombination, translate into a non-functional protein. A *loxP* site is a 34 base pair sequence composed of reverse 13 bp palindromic repeats flanking an 8 bp core sequence. Cre recombinase is a Type I topoisomerase, isolated from P1 bacteriophage, which catalyzes DNA recombination between *lox*P (locus of crossing over, P1) sites. Depending on the orientation of the *lox*P sites, Cre will either delete or invert the DNA segment they flank[105].

This same strategy can be used to overexpress a protein in a specific cell type. Here, a "strong" promoter sequence is used to transcribe our cDNA of interest. By placing a polyA stop signal flanked by *loxP* sites before the cDNA, transcription stops and the cDNA remains untranscribed. Upon Cre-mediated excision of the stop signal, transcription of the cDNA can take place. The cDNA of interest, in theory, is then expressed in specific cell types, and their progeny.

We used a Cre-loxP genetic strategy to conditionally inactivate and overexpress *Sox9* in the uterine epithelium. We took advantage of the *Pgr-Cre* mouse line that expresses Cre recombinase in the LE and GE starting around P14. *Pgr-Cre* mice were crossed with *Sox9 fx/fx* mice to generate *Pgr-Cre; Sox9 fx/fx* females. Upon Cre-mediated recombination, the 3rd exon of the *Sox9* gene should be deleted, thus inactivating the protein.

Material and Methods

Mice

Pgr-Cre mice were obtained from Dr. Franco DeMayo at Baylor Medical Center[106]. *Sox9 fx/fx* mice were obtained from Dr. Andreas Schedl (University of Nice, France)[107], *Rosa 26 Reporter-H$_2$B-mCherry-EGFP-GPI (R26R-RG)*[93] were obtained from Dr. Go Shioi (RIKEN Center for Developmental Biology, Kobe, Japan). *Sox9-Cre*[92] and *Sox9-ires-enhanced green fluorescent protein (EGFP)* mice[108] were generated in our laboratory in collaboration with Dr. Haruhiko Akiyama (University of Kyoto, Japan). *R26R-LacZ* mice were obtained from Dr. Philippe Soriano (Baylor College of Medicine). All mice were maintained on a C57BL/6J x 129/SvEv mixed genetic background. All animals were maintained in accordance with the Public Health Service Policy on Humane Care and Use of Laboratory Animals, the U.S. Department of Health and Humane Services Guide

for the Care and Use of Laboratory Animals, and the United States Department of Agriculture Animal Welfare Act. All protocols were approved by the University of Texas M.D. Anderson Cancer Center Institutional Animal Care and Use Committee.

Polymerase Chain Reaction

DNA was extracted following the protocol described in Chapter II. PCR was performed using the following primers.

Cre primers: (*Sox9-Cre* and *Pgr-Cre)*

Cre forward: 5' GGACATGTTCAGGGATCGCCAGGC 3'

Cre reverse: 5' CGACGATGAAGCATGTTTAGCTG 3'

PCR was performed with a 95°C denaturing step for 5 minutes, followed by a second 95°C denature for 30 seconds, a 57°C annealing step for 45 seconds and a 72°C elongation step for 45 seconds. Steps 2-4 were cycled 30 times. Lastly, a final incubation of 72°C for 5 minutes allowed complete elongation of the region of interest. Using Cre forward and reverse primers, we detected a 219 bp Cre DNA product on a 1.5% agarose gel.

Sox9 fx/fx primers:

Sox9-Forward: GGGGCTTGTCTCCTTCAGAG

Sox9-Reverse: TGGTAATGAGTCATACACAGTAC

PCR was performed with a 95°C denaturing step for 5 minutes, followed by a second 95°C denature for 30 seconds, a 65°C annealing step for 45 seconds and a 72°C elongation step for 45 seconds and cycled 30 times. Lastly, a final incubation of 72°C for 5 minutes allowed complete elongation of the region of interest. Using *Sox9* forward and reverse primers, we detected a 150 bp wild-type and a 170 bp fx band DNA product on a 1.5% agarose gel.

X-gal Staining of Female Reproductive Tracts

Sox9-Cre mice were crossed to Gtrosa26[tm1Sor] (R26R) females to mark *Sox9*-expressing cells and their progeny in the uterine epithelium. FRTs were collected at various developmental and post-parturition time-points. The FRT was dissected in cold PBS and then transferred into 4% paraformaldehyde (4% PFA) for 1 hour at 4ºC, followed by 3 x 15 minute rinses in 0.02% NP-40 (Calbiochem, 492015)/0.01% deoxycholic acid (Sigma, D-6750) in PBS. The FRTs were then transferred into staining solution (10% NP-40, 1% deoxycholic acid, 1 M MgCl$_2$, 0.1 M EDTA, pH 8, 0.5 M K$_3$Fe(CN)$_6$ (Sigma-Aldrich 244023) = 8.25 g/50 ml, 0.5 M K$_4$Fe(CN)$_6$ (Sigma-Aldrich P3289) = 10.5 g/50 ml, and 40 mg/ml X-gal (Gold Biotechnology, cat# X4281C)) and stained overnight at 37ºC. The following morning the FRTs were washed with 0.02% NP40/0.01% deoxycholate in PBS.

The FRTs were dehydrated using sequential methanol (MeOH) dehydration steps (25% MeOH, 50% MeOH, 75% MeOH, 100% MeOH), 15 minutes in each step at 4ºC. Following the dehydration steps, the tissues were cleared inside a glass tube by adding a 1:1 BABB (benzyl alcohol- benzyl benzoate) /MeOH solution and incubated for 2 hours at 4ºC. The BABB/MeOH was discarded appropriately and a BABB solution was added and incubated for more than 2 hours at 4ºC. The tissues were viewed and photographed under the Leica microscope.

Hematoxylin and Eosin (H&E) Staining

The female reproductive organs were dissected and immediately placed in cold PBS. Depending on the size, the tissues were transferred into 15 ml conical tubes or 1.5 ml tubes containing 4% PFA (Electron Microscopy Sciences, cat#19210) and left overnight on a nutator mixer at 4ºC. The next day the tissues were washed with 70% ethanol 3 times for 15 minutes on the nutator at 4ºC. The tissues were enclosed inside a tissue cassette (Fisherbrand histosette II tissue cassettes, cat # 15182701E). The cassettes were then placed in a Leica TP 1020- automatic tissue processor and processed in 70% ethanol for 30 minutes, 80% ethanol for 30 minutes, 90% ethanol for 30 minutes, and 95% ethanol (1) for 30 minutes. 95% ethanol (2) for 8 hours and 3 dehydration steps of 100% ethanol for 30 minutes each. After the ethanol dehydration steps the cassettes were transferred into a Histoclear (National Diagnostics, # HS-200) for 30

minutes followed by another Histoclear wash for 30 minutes. Lastly, the cassettes were transferred into a vacuumed chamber containing melted paraffin for 8 hours followed by a second vacuumed chamber containing melted paraffin for 2 hours.

The tissues were released from the tissue cassette and embedded in paraffin (McCormick paraplast tissue embedding medium, Ref# 501006) using a Leica EG 1160 embedding station set at a temperature of 61°C. The tissues were placed in a metal cast either perpendicular to the bottom for transverse sections or on the side for longitudinal sections.

Serial sections of the uterus were cut using the Leica RM 2255 microtome. Cross-sections of the uterus were made starting in the most anterior end (oviduct) to the most posterior end (cervix). Sections were cut with a width of 6 μm, air-dried and then left at 42ºC overnight.

Before staining, tissue sections were deparaffinized 3 times in Histoclear solution for 5 minutes. Sections were washed twice with 100% ethanol (Pharmco-Aaper, cat# E200) for 3 minutes, twice with 95% ethanol (Pharmco-Aaper, cat# E190) for 3 minutes, and a final 70% ethanol wash for 5 minutes. After the ethanol wash the slides were rinsed in tap water and then transferred to distilled water for 1 minute.

The tissue sections were stained with Harris Hematoxylin (Protocol, Cat# 245-651) for 5 minute, quickly rinsed in tap water, and then dipped 10 times in 1% acid alcohol (1% hydrochloric acid/70% ethanol). The tissue sections were then placed under running tap water for 15 minutes. After the tap water wash, the

sections were verified for proper retention of the hematoxylin, dark blue nucleus with a clear background. Overstained slides were dipped in 1% acid alcohol and checked for proper dark blue nuclear stain. The tissue sections were transferred from into 0.5% eosin (Sigma Eosin Y solution, aqueous, Cat# HT110-2-128) solution for 5 minutes. The excess eosin was washed off by a series of ethanol washes, 10-15 dips in 70% ethanol, 10-15 dips in two consecutive 95% ethanol solutions, and 10-15 dips in two consecutive 100% ethanol solutions. The tissue sections were transferred into a three times for two minutes washes in Histoclear solution. Lastly, 2-3 drops of Permount (Fisher Scientific, SP15-500) were placed on top of the tissue sections and a coverslip was carefully positioned on top of the slide.

Masson's Trichrome Staining

Sections were washed twice with 100% for 3 minutes, twice with 95% ethanol (Pharmco-Aaper, cat# E190) for 3 minutes, and a final 70% ethanol wash for 5 minutes. After the ethanol wash the slides were rinsed in tap water and then transferred to distilled water for 1 minute.

To stain collagen fibers we used the Accustain Trichrome Stain Kit (Sigma-Aldrich, Cat# HT15) and followed the protocol suggested by the company.

Alcian Blue Staining

We performed Alcian Blue staining to detect sulfated and carboxylated acid mucopolysaccharides. Tissue slides were deparaffinized and rehydrated following the same protocol described in H&E. The tissue sections were placed in a 3% acetic acid solution (Fisher Scientific, Cat # BP1185-500) for 3 minutes. The slides were transferred into an Alcian blue solution containing 1% Alcian Blue 8GX Stain (Sigma, Cat# A3157) and 3% acetic acid diluted in water for 30 minutes at room temperature. Later, the slides were washed in tap water for 10 minutes and then rinsed in distilled water. The tissue sections were counterstained in a nuclear red solution for 5 minutes. The slides were washed in tap water for 1 minute and dehydrated in 95% ethanol. Later, the slides were transferred into 3 x Histoclear for 2 minutes and sealed with Permount.

Immunofluorescent Staining

Tissue sections were placed in an oven for 30 min at 55ºC, then deparaffinized and rehydrated as for H&E histology. The sections were placed in a 10mM Sodium Citrate (Fisher Scientific, Cat# S279-3) epitope retrieval solution heated in a microwave oven for 20 minutes, and cooled for 45 minutes at room temperature. The sections were washed with PBS for 5 minutes, then placed in 3% H_2O_2 (Dako) for 10 minutes. The sections were washed with PBS for 5

minutes. Several primary antibodies used here were produced in mice; therefore, we incubated tissue sections in mouse IgG for 1 hour at room temperature. Following the masking of native IgG, the tissue sections were placed in serum-free protein blocking solution made up 3% BSA, 1%Triton-X 100, in PBS for 30 minutes at room temperature. The excess blocking solution was absorbed using a Kimwipe before the primary antibody was added. The following primary antibodies and dilutions were used:

α-SOX9- Millipore Cat# AB5535 - 1:200

α-E-Cadherin- BD Biosciences Cat# 610181 - 1:200

α-FOXA2- Abcam- Cat# ab40874 - 1:200

α-TRPV4- Abcam- Cat# ab39260 – 1:100

α-Ki67- Abcam- Cat# ab8191- 1:100

α-Phosphohistone H3- Millipore Cat# 06-570- 1:200

Alexa Fluor 488 Phalloidin- Invitrogen Cat# A12379 - 1:20

The primary antibody solution was added directly on top of the tissue sections and incubated overnight at 4ºC. The next day, the tissue sections were washed 3 times with PBS for 10 minutes to remove non-specific binding. After the PBS washes the sections were incubated with a 1:400 dilution of the secondary antibody.

The tissue sections were washed 3 times with PBS/tween for 5 minutes to remove non-specific secondary antibody binding. One drop of Vectashield mounting media (Vector, #H-1200) containing 4', 6-diamidino-2-phenylindole

(DAPI) was placed directly on top of each tissue section. The sections were mounted with coverslips with then imaged. After imaging sections were stored at 4ºC.

TUNEL Staining

To determine the number of cells undergoing programmed cell death, we performed TUNEL staining. Fragmented double stranded DNA can be identified by labeling free 3'-OH terminal ends using this protocol. Tissue slides were deparaffinized and rehydrated following the same protocol described in H&E.

The slides were incubated with Proteinase K (20 µg/ ml in 10 mM Tris-HCl pH 8.0) for 20 minutes at 37ºC. The slides were washed 3 times in PBS for 5 minutes. After washing off the Proteinase K, the slides were transferred into permeabilization solution (0.1% Triton X-100 in 0.1% sodium citrate) for 2 minutes on ice. We added 50 µl TUNEL reaction mixture (5 µl of TUNEL-Enzyme solution (Roche Applied Science, Cat# 1767305) and 45 µl TUNEL-Label solution (Roche Applied Science, Cat #1767291)) and incubated for 1 hour at 37ºC in the dark. The slides were washed 3 times in PBS for 10 minutes. Drops of Vectashield mounting media were added directly on top of the tissue sections and covered with a coverslip.

Results

Spatio-Temporal Expression of *Sox9* during Uterine Gland Development

In the adult uterus, SOX9 was present mostly localized in the nucleus of the GE (Figure 3). In Chapter IV (Figure 24), I show immunofluorescent staining that demonstrates that SOX9 is present primarily in the GE at various time point during the development of the FRT. To visualize spatio-temporal expression of *Sox9* in the uterine epithelium*,* we used a mouse line in which an *ires-enhanced green fluorescent protein (EGFP)* sequence was knocked into the 3' untranslated region of the endogenous *Sox9* gene[108]. Cells expressing *Sox9* should also express green fluorescent protein (GFP), which can be detected using fluorescent microscopy. We mated male and female homozygous *Sox9-EGFP* mice and dissected the reproductive tract of 16.5 days post-coitum *Sox9-EGFP* females.

In embryonic day (E) 16.5 females, the Müllerian duct is present while the Wolfian duct degenerates due to a lack of testosterone. We observed GFP signal present in the epithelium of the Müllerian duct (Figure 8A, B). This observation suggests that *Sox9* is expressed in progenitor cells of the female reproductive tract. GFP fluorescence was also observed in the developing female gonads; however, the gonads are known to contain various endogenous fluorophores that emit fluorescent signal under ultra violet light. This auto-fluorescence is caused by increased levels of NADH and FAD during meiotic maturation[109].

Figure 8: Expression of *Sox9-EGFP* during uterine gland development. (A, H) Brightfield images, (B-G, I), fluorescent images. (A) Anterior region of E16.5 FRT. (B) Fluorescent image of Panel A, showing GFP signal detected in the epithelium of the Müllerian duct. (C) P1 FRT shows GFP signal in the uterine epithelium and in the oviduct. (D) P6 uterus shows GFP signal in the uterine epithelium. Epithelial invaginations can be observed. (E-G) P8 FRT. (E) Multiple buds are observed sprouting from the luminal epithelium. (F) Higher magnification showing the surface of the luminal epithelium. Greater GFP signal is detected in the creased epithelium and in the nascent. (G) GFP signal is detected in the cervical epithelium. (H, I) P21 uterus opened to reveal the surface of the luminal epithelium. (I) Epithelial creases and uterine glands show greater GFP signal. cvx, cervix; g, gonad; ge, glandular epithelium; le, luminal epithelium; md, Müllerian duct; ovd, oviduct; ut, uterus. Scale bar, 500 µm
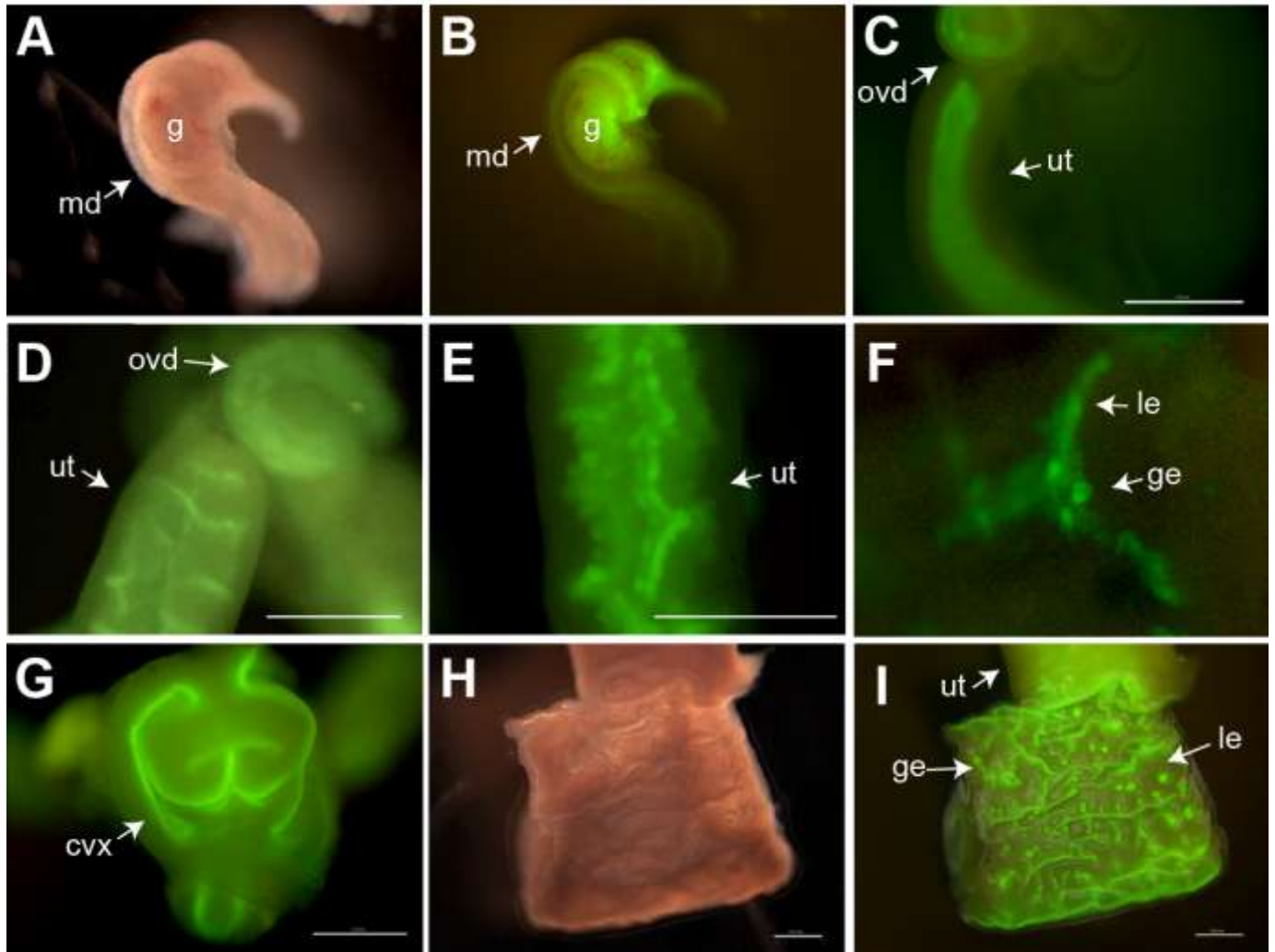
At P1, the GFP signal was observed in the uterine epithelium (Figure 8C). Interestingly, at P6, as the uterus remodels during postnatal development, we detected greater GFP signal in the epithelial invaginations forming radially along the length of the uterus (Figure 8D). These epithelial invaginations extend along the surface of the uterine epithelium forming epithelial creases, also termed uterine folds. At P8 a large number of epithelial buds were observed protruding from the LE (Figure 8E). Opening the uteri revealed that the GFP signal was pronounced in the epithelial creases and the nascent UGs (Figure 8F). Nascent glands were seen at P8 but not at P6. We also detected GFP in the cervical epithelium (Figure 8G). Therefore, *Sox9* was expressed in the epithelia of the female reproductive tract.

At P21, we detected strong GFP signal in the GE and the creases of the LE. We observed multiple UGs that extended perpendicularly from the creases in the epithelium. These observations corresponded with our initial findings that SOX9 levels were predominantly present in the GE and suggested that SOX9 somehow regulates invagination of the uterine epithelium and subsequent UG formation.

Analysis of SOX9-Lineage Positive Cells during Uterine Gland Development

The GFP expressed in the *Sox9-EGFP* mouse line is easily degraded, rendering us unable to visualize the fluorescent signal by confocal microscopy. Fortunately, RFP expressed from *Sox9-RG* is adequately maintained during

tissue processing, allowing us to take advantage of tissue sections from postnatal *Sox9-RG* females to visualize the location of SOX9-lineage positive (LP) cells during uterine differentiation. At P6, most SOX9-LP cells were detected close to where the uterine epithelium is beginning to invaginate (Figure 9A). Removing the DAPI signal allowed us to visualize solely the red nuclei of SOX9-LP cells (Figure 9B). We observed that most SOX9-LP cells were present in the LE, although some cells were present in the stroma (Figure 9B).

As UGs develop and differentiate, a greater number of SOX9-LP cells were present in the GE and to a lesser extent in the LE (Figure 9C-F). In adult females, SOX9-LP cells constitute almost the entire GE (Figure 6, 9G, H). Additionally, some SOX9-LP cells were also present in sections of the LE. Our findings demonstrated that SOX9-LP cells, although initially found in the LE, appear to relocate themselves into the forming UGs and eventually compose the entire GE.

To generate a detailed picture where SOX9-LP cells are positioned during UG formation we examined several uteri from P6 to P10. We were unable to observe any UGs at P6, only the start of the creases that formed in the uterine epithelium (Figure 9A). We observed a nascent UG at P7 (Figure 10A-D). The entire nascent UG was composed of SOX9-LP cells (Figure 10D). Additionally, SOX9-LP cells were part of the invaginating epithelium (Figure 10A-F). The invaginating epithelium forms the creases we observed at P21 (Figure 8H-I).

Figure 9: Sox9-lineage positive (Sox9-LP) cells mark the adult UGs. (A - H) Frozen sections made from uteri dissected from *Sox9-RG* females. Fluorescent images captured using confocal microscopy and rendered using Imaris software. (A, B) Section of the uterus dissected at P6. (A) mCherry FP (red) and DAPI (blue). (B) Only the red channel is shown for Panel A to highlight the SOX9-LP cells. (C, E) Uterine sections from P35 females, showing mCherry FP and DAPI signals. (D, F) Only red channel is shown in D for Panel C and in F for Panel E. (G, H) Uterine sections derived from 8-week-old females. (G) mCherry FP and DAPI signals. (H). Only red channel is shown in H for Panel G. GE, glandular epithelium; LE, luminal epithelium. Scale bar, 50 µm.
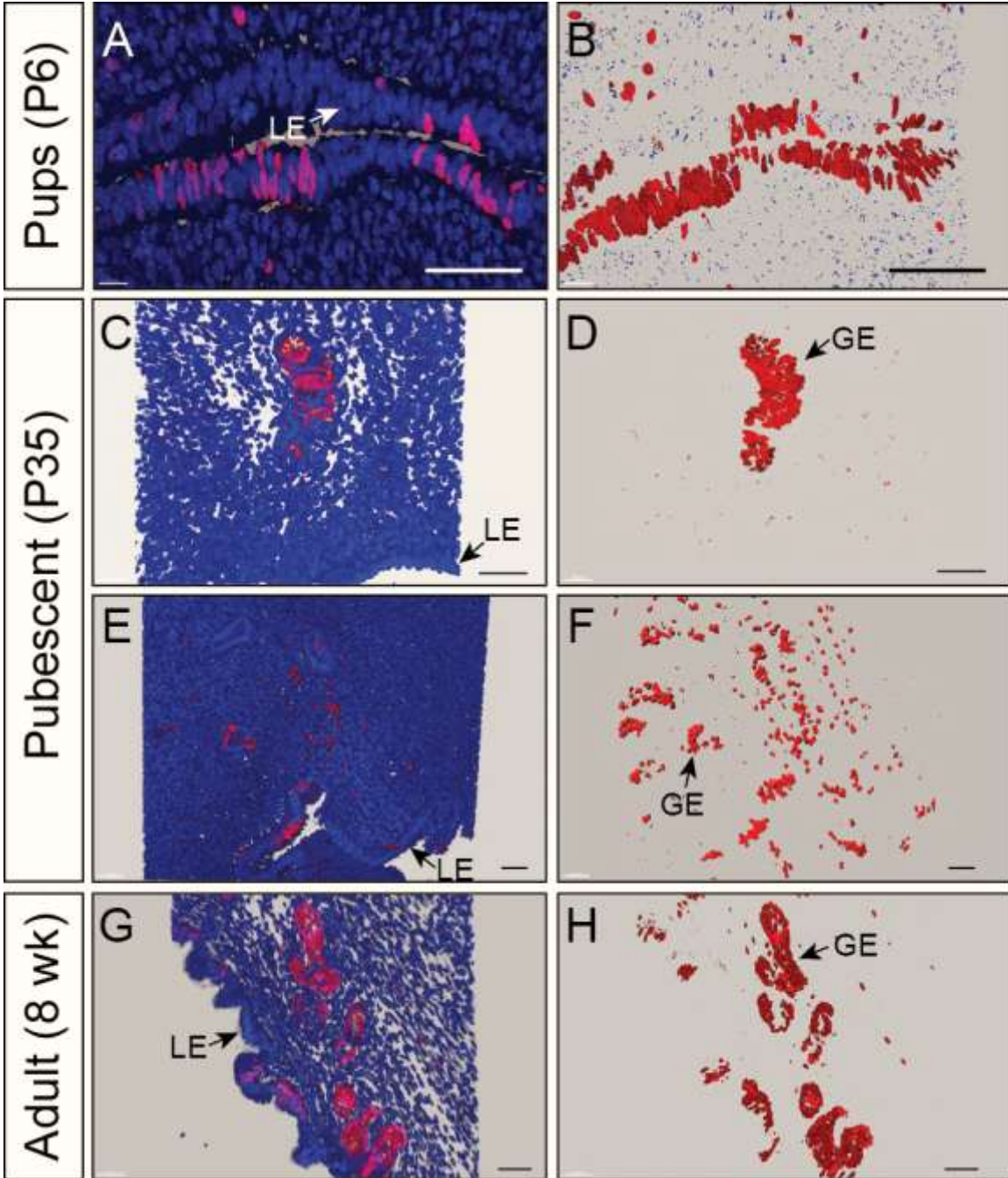
Figure 10: SOX9-Lineage Positive cells contribute to UG formation. (A-H) Frozen sections derived from P7 *Sox9-RG* females stained with Phalloidin (green) and DAPI (blue). (A, C) Red, blue, and green channels. (B, D) Red and green channels. Blue arrowhead shows a mitotic figure in the luminal epithelium near the invaginated epithelium. (C, D) Nascent UG in the stroma. (E, F) Red and green channels. Arrowheads point to the nuclei of SOX9-LP cells found close to the basement membrane. (G, H) View of the apical membrane. (G) Red, blue, and green channels. (H) Removal of the green signal (cytoskeleton) from Panel G. Nuclei of SOX9-LP cells (arrowheads) appear to be closer to the basement membrane. SOX9-LP cells, red; DAPI, blue; Phalloidin, green; basement membrane (dashed lined).
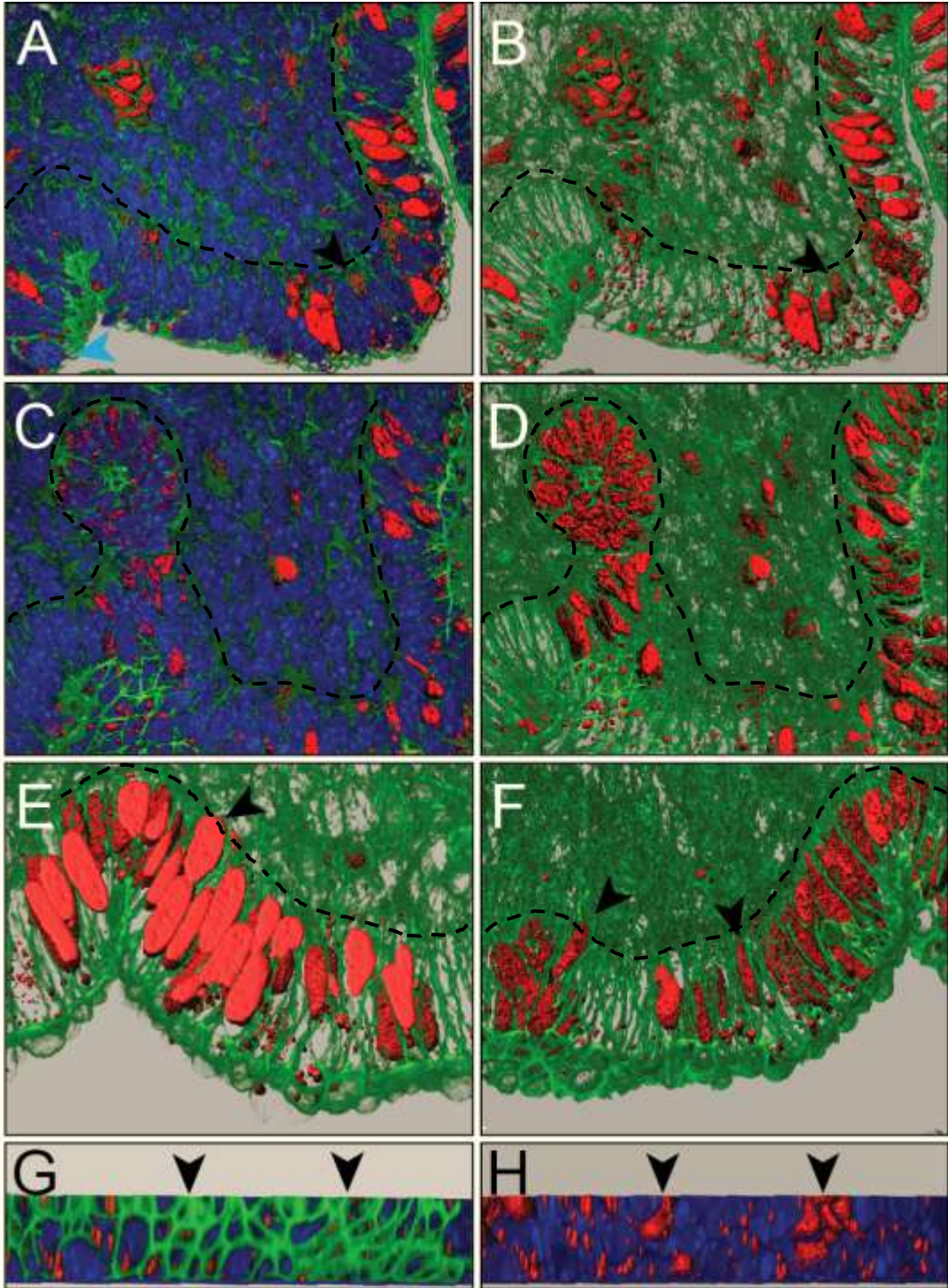
The nuclei of SOX9-LP cells were positioned near the basal membrane and appear to extend into the stroma (Figure 10A, B, E, F, black arrowheads). Moreover, by looking at the surface of the LE, we noticed that the actin cytoskeleton of SOX9-LP cells, stained green by Phalloidin, masked the red nuclei, indicating that the nuclei were positioned closer to the basal membrane (Figure 10G, H). Therefore, we have provided additional evidence that correlates the presence of SOX9 with the invaginations of the uterine epithelium.

SOX9 Expression in the Adult Uterus during the Estrous Cycle

We determined that SOX9 was expressed during the embryonic and postnatal development of the mouse FRT. In adult females, SOX9 was present in the ampulla of the oviduct and in the UGs of the uterus (Figure 8C, D). Once females reach adulthood, the uterus undergoes considerable morphological changes during the estrous cycle[18]. Driven primarily by the influence of circulating hormones, various genes are upregulated and downregulated during the estrous cycle. Two independent datasets detected higher levels of *Sox9* mRNA during the secretory phase in the human endometrium[110,111]. To determine if SOX9 fluctuates during the estrous cycle, we dissected uteri of B6 females at specific stages of the estrous cycle. By performing daily vaginal smears on B6 females, we were able to determine the stage of the estrous cycle. We collected various uteri at proestrus, estrus, metestrus, and diestrus.

We sectioned longitudinally along the length of the uteri. Longitudinal uterine sections were taken and stained using α-SOX9. We observed that UGs, stained by SOX9, were found primarily in the antimesometrial side of the uterus, corroborating our findings from Chapter I. We observed that SOX9 was present in the GE all through the estrous cycle (Figure 11A-H). In comparison to all the other stages of the estrous cycle, a relatively small number of LE cells stained positive for SOX9 during diestrus (Figure 11G, H). Therefore, it appears that SOX9 is maintained in the GE while its expression fluctuates during the different stages of the estrous cycle.

Two independent datasets detected higher levels of *Sox9* mRNA during the secretory phase in the human endometrium[110,111]. In mice, the maximal secretory activity of the uterine takes place during estrus[21]. We observed greater number of cells expressing SOX9 during estrus. Thus, it seems SOX9 levels are higher during the secretory phase in both human and mice.

While assaying for changes in levels of SOX9 in the adult uterus, we also found that mitotic figures in the LE seem to be, for the most part, devoid of SOX9 (Figure 11, black arrows). We only observed a few mitotic figures that were SOX9 positive (Figure 11, red arrowhead). At P7, we made a similar observation (Figure 10A, blue arrowhead). This suggests that cells with nuclear SOX9 are less likely to be in mitosis.

Figure 11: SOX9 levels fluctuate throughout the estrous cycle. (A-H) Immunofluorescent staining of the uterus using an α-SOX9 antibody (green). Nuclei were stained with DAPI (black). B, D, F, and H are higher magnification images of A, C, E, and G, respectively. (A, B) Proestrus. (C, D) Estrus. (E, F) Metestrus. (G, H) Diestrus. Most mitotic figures (black arrowheads) are negative for SOX9. Red arrowhead shows one mitotic figure that contained SOX9. SOX9, green. Scale bar, 50 μm

Proestrus

Estrus

Metestrus

Diestrus

72
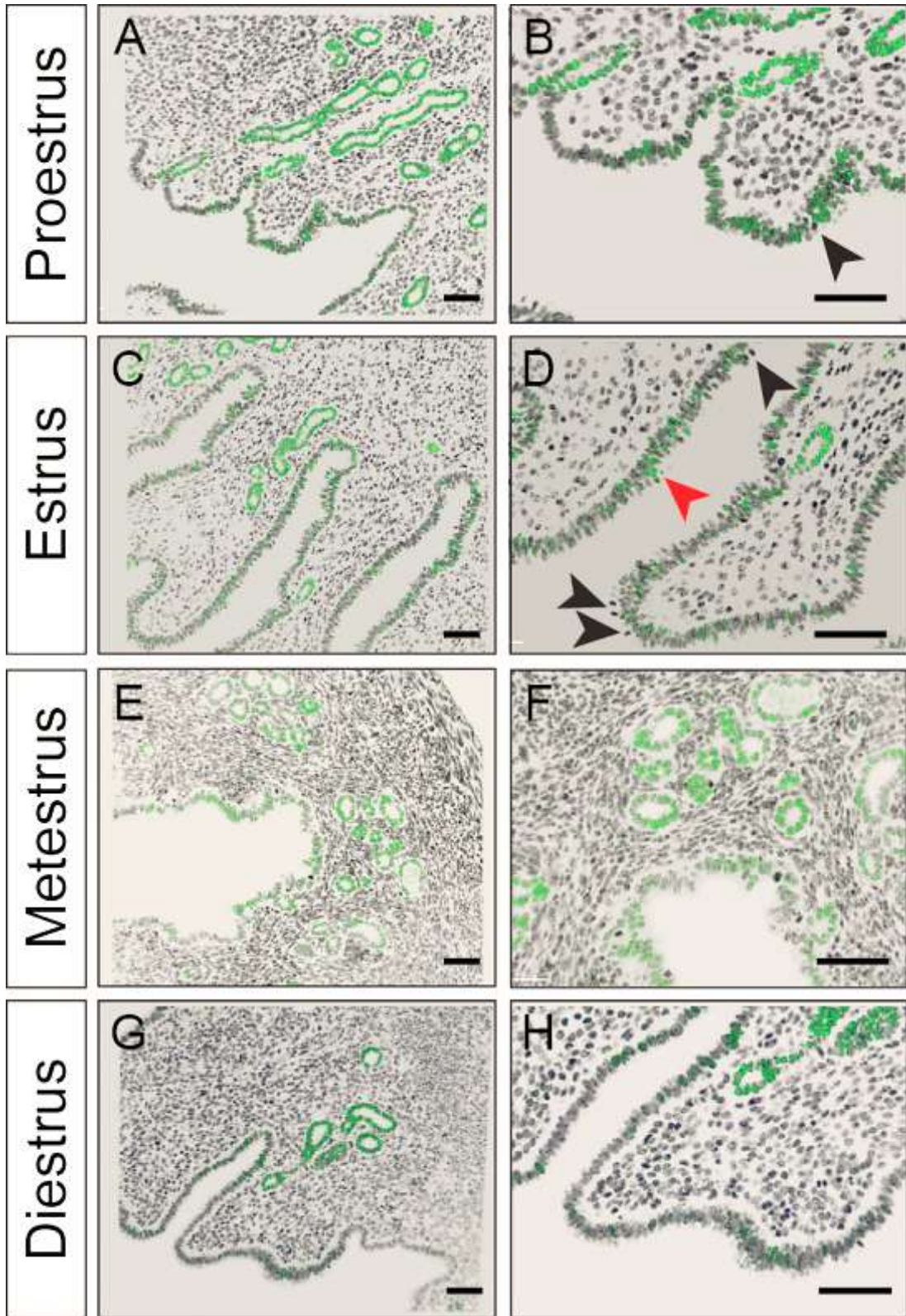
Affects of Parturition on Uterine Gland Homeostasis

As the fetus grows inside the mother's womb, it puts a strain on the uterus. The human endometrium is fully regenerated by the 16th day post parturition (PPD)[112]. Tissue regeneration of the mouse endometrium PPD is poorly understood. To determine if the UGs are affected by the developing fetus places on the endometrium, we used *Sox9-EGFP* mice to observe the UGs during pregnancy and after birth during endometrial regeneration. Using the *Sox9-EGFP* mouse line, we were able to detect UGs present in the uterus of pregnant females (16.5 days post-coitus, dpc) (Figure 12A, B). Our observations indicate that UGs are maintained in inter-implantation regions of the uteri (Figure 12A). Therefore, we can conclude that UGs are present in the uterus between implantation sites two days prior to parturition (18.5 dpc) and that they appear normal.

To determine what happens to the UGs after parturition, we generated *Sox9-Cre*; *Rosa-26-Reporter-LacZ (Sox9-R26R-LacZ)* females. We mated these females to B6 wild-type males and dissected the uteri at 10.5 dpc and at post-parturition day 1 (PPD1). Cells that express *Sox9* and their progeny will express β-galactosidase. The uteri were placed in a solution that contained X-gal. β-galactosidase converted the X-gal into an indigo-colored compound that marked SOX9-LP cells.

Figure 12: UGs are maintained in inter-implantation sites. (A, B) Fluorescent image of uteri from pregnant 16.5 dpc *Sox9-EGFP* females. UGs (red arrowhead) are found between implantation sites (*). (B) Because the uterus is stretched, single UGs were observed spaced around the uterus. (C-F) LacZ-stained and BABB cleared uteri from pregnant *Sox9-LacZ* females. Lineage-tracing analysis showed SOX9-lineage positive cells present in implantation sites (*) but were absent after parturition (E, F). SOX9-LP cells in the inter-implantation sites (red arrowhead) extend toward the implantation sites that lack SOX9-LP cells. M, mesometrial side; A, antimesometrial side; P, placenta; E, embryo. Scale bar, 1 mm.
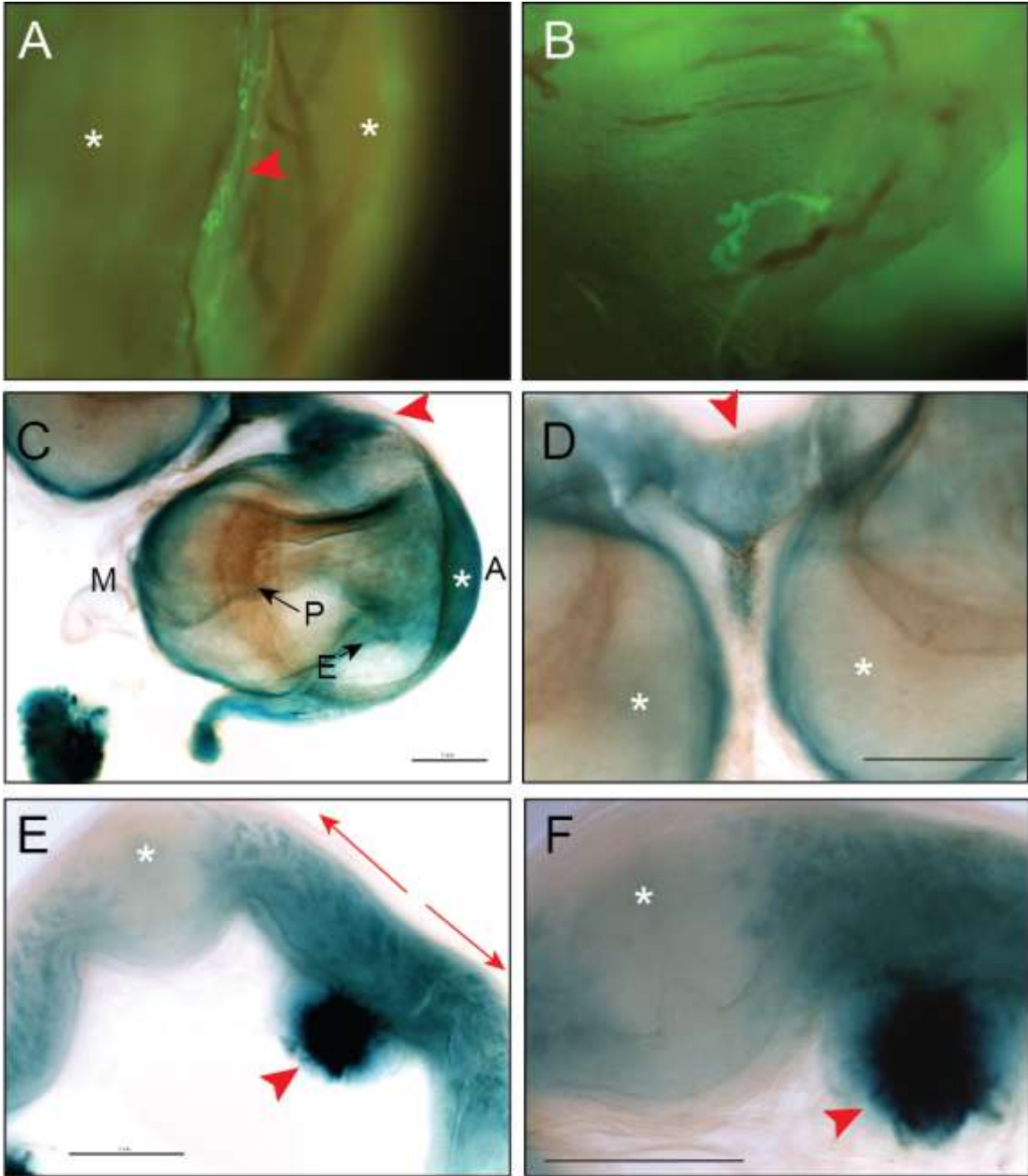
We detected LacZ signal along the entire length of the uteri of pregnant females in both the antimesometrial and mesometrial regions (Figure 12C, D). LacZ signal was detected in the inter-implantation sites (Figure 9D, red arrowhead) and in the implantation sites (Figure 12C, D, white asterisk).

At PPD 1, we detected LacZ signals in most of the uterine horn (Figure 12E). However, we did not detect any LacZ signal in the presumptive implantation sites (Figure 12E, F, white asterisk). Therefore, it seems that most of the SOX9-LP cells in the implantation sites are lost during parturition. Moreover, SOX9-LP cells that were maintained in the inter-implantation regions appear to expand rapidly after parturition, as detected in PPD1 uteri (Figure 12E).

We have also detected a structure present on the mesometrial side of the uteri. Interestingly, this structure was detected in the inter-implantation sites at E10.5 (Figure 12C, D), at PPD1 (Figure 12E, F, red arrowhead), and at PPD5 (data not shown). Red blood cells appeared brown under the light microscope. At E10.5, brown dots can be observed in the placenta and in inter-implantation sites (Figure 12C, D). A greater number of brown dots were observed in the structures present in the inter-implantation sites at PPD1 (Figure 12, F). In these regions, we also detected a greater LacZ staining.

Generation of *Pgr-Cre; Sox9 fx/fx* Conditional Knockout (cKO) Mice

Pgr-Cre mice were mated with *Sox9 fx/fx* mice. *Pgr-Cre/+; Sox9 fx/+* males were fertile; therefore, they were mated to *Sox9 fx/fx* females to generate *Pgr-Cre/+; Sox9 fx/fx* males and females (Figure 13). *Pgr-Cre/+; Sox9 fx/fx* males were crossed with *Sox9 fx/fx* females to generate *Pgr-Cre/+; Sox9 fx/fx* (**Sox9-cKO**) females at a higher rate. The progeny inherited the Cre allele following Mendelian patterns of inheritance. No statistical differences were found in weight or size between *Sox9-cKO* and control littermate females (data not shown).

Sox9-cKO females were fertile; however, they were not used for breeding purposes. The *Pgr-Cre* allele was generated by knocking Cre into the 1st exon of the *Pgr* gene[106]. This insertion inactivates the *Pgr* gene product. Therefore, homozygous *Pgr-Cre/ Pgr-Cre* are considered *Pgr* knockouts.

To analyze the effect of inactivating *Sox9* in the epithelium, we focused our primary analysis on P21, 28, and 35, since the Cre is presumably expressed after P14. We dissected the female reproductive organs and measured in the length. No statistical difference was observed when comparing *Sox9-cKO* and control littermates (n= 56). No gross abnormalities in the FRT were observed. All the constituent organs (2 ovaries, 2 oviducts, 2 uterine horns, a cervix and the upper vagina) were present in all the FRTs dissected

Examination at later time-points, 8 weeks, 4 month, 8 months, and 1-year-old revealed no overt gross morphological differences between *Sox9-cKO* and control littermates (Figure 14E-H).

Figure 13: Genetic strategy used to conditionally knockout *Sox9* in the uterus*.* Pgr-Cre heterozygotes were crossed with Sox9 fx/fx mice to generate *Pgr-Cre; Sox9 fx/+* mice. *Pgr-Cre; Sox9 fx/+* males were crossed to *Sox9 fx/fx* females to generate both *Sox9-cKO* (*Pgr-Cre; Sox9 fx/fx*) and control (*Sox9 fx/fx*) females.

Pgr-Cre   Sox9 fx/fx

Pgr-Cre; Sox9 fx/+   Sox9 fx/fx

Pgr-Cre; Sox9 fx/fx   Wt; Sox9 fx/fx
Sox9-cKO   Control
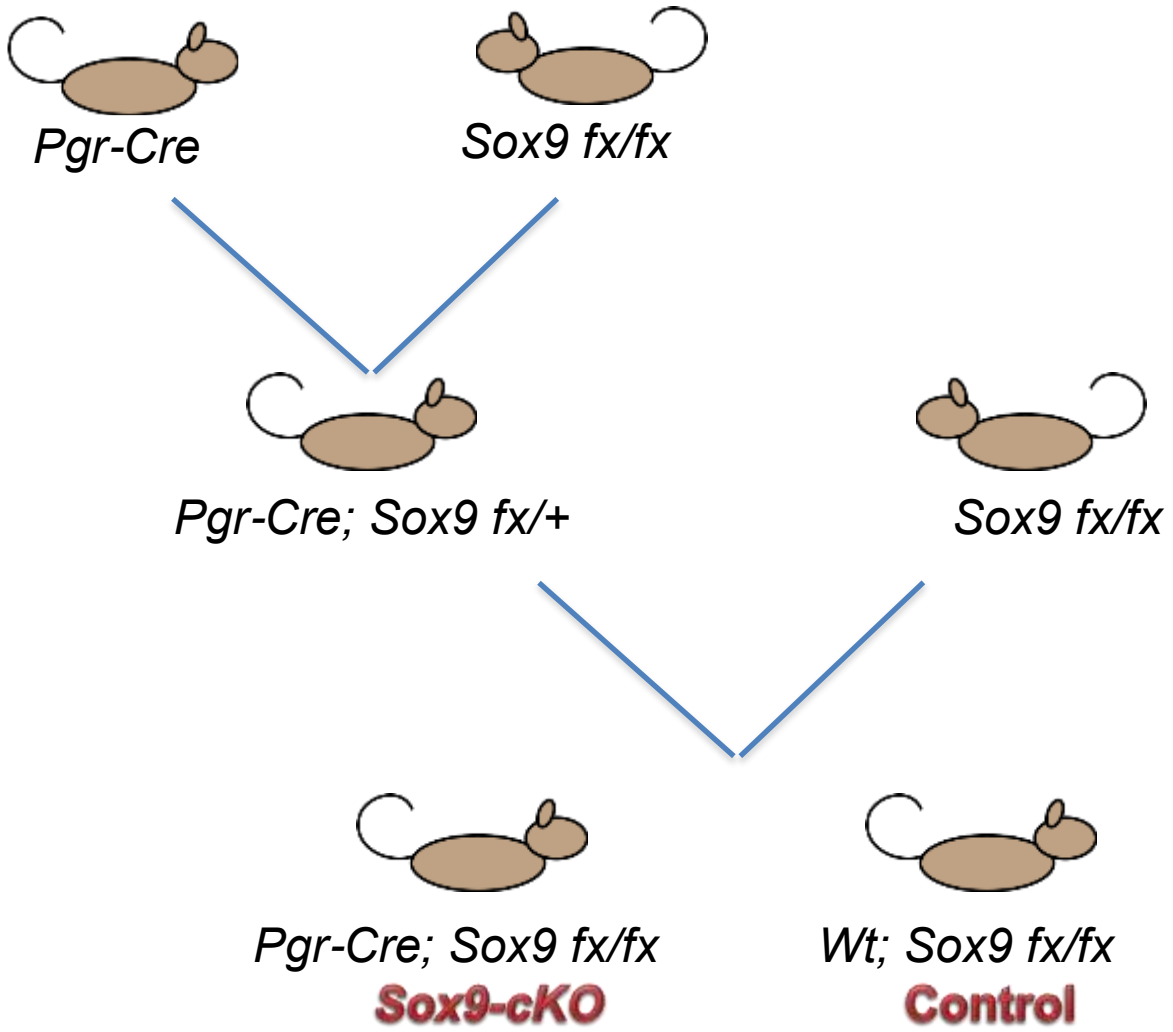
In 8 months and 1-year-old females, I did notice that there appeared to be an increased number of epithelial folds in *Sox-cKO* (n=5) when compared to control uteri (n=7) (Figure 14F, H). Concomitantly, there was less space in the uterine cavity. This was an initial observation and still requires a more effective way to quantify these potential differences. Although it is a minor change, I will come back to this later during the discussion.

Initial assessment showed that *Sox9-cKO* females appeared to be subfertile; however, upon increasing the number of females in the trial, we found that there was no statistical difference between cKO and littermates, 4.6 and 5.1 pups/litter, respectively.

Histological Analysis of *Sox9-cKO* Uteri

To analyze the changes that take place in uterine morphology at the cellular-level following the inactivation of *Sox9*, uteri were fixed in 4% PFA and mounted in paraffin blocks. Tissues were sectioned in the transverse plane (cross-sections) and longitudinal plane of the entire reproductive tract. We generated approximately 10-15 tissue section slides from each female. Tissue sections were stained with H&E, Masson's Trichrome or Alcian Blue. H&E stains nuclei dark blue and cytoplasm pink. Masson's Trichrome stained collagen fibers blue, nuclei black and keratin red. Alcian blue stained mucopolysaccharides and glycosaminoglycans blue.

Figure 14: Gross morphology of *Sox9-cKO* uteri. (A-H) Brightfield images of 1-year-old uteri. No major gross morphological changes were observed in the uterus after conditionally inactivating *Sox9* (E-H) when compared controls (A-D).
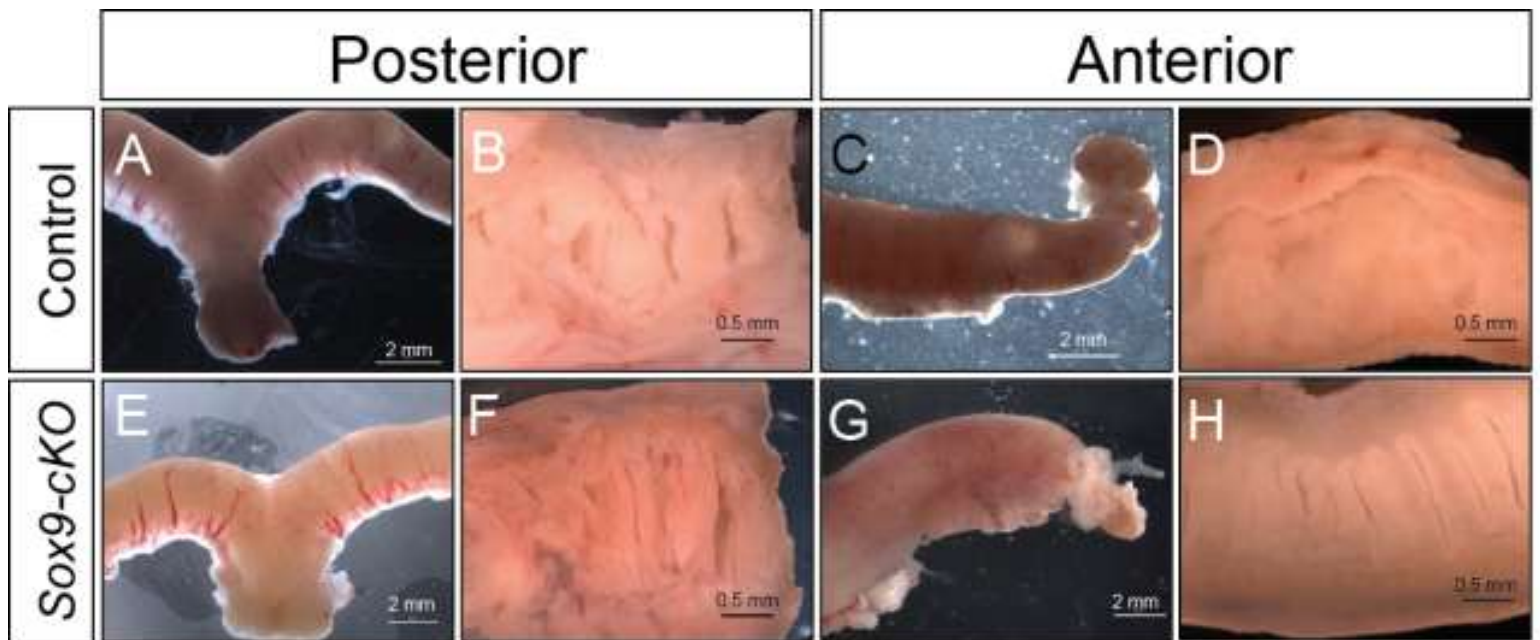
Tissue sections stained with H&E revealed generally subtle differences when comparing the cellular morphology of *Sox9-cKOs* and controls. At P21 and P28, the luminal epithelium appeared similar to controls as did the stroma and myometrium. As we analyzed tissue sections at later time points (8-week, 4-month, and 8-month), we observed that the stroma of the *Sox9-cKO* appeared less dense when compared to tissue sections made from control littermates. I do have to point out that the thinning of the stroma observed in tissue sections derived from *Sox9-cKO* uteri was observed primarily during estrus; when the uteri increase in width (Figure 15D, E, asterisk). To summarize our findings using H&E, there were no major morphological differences between *Sox9-cKO* and control uteri from P21 to 8-month.

Since SOX9 is known to regulate extra cellular matrix (ECM) secretions we stained uterine sections using Masson's Trichrome and Alcian Blue. Using Masson's Trichrome staining, we were able to detect lower levels of collagen fibers, stained blue, in the uterine stroma of *Sox9-cKO* females (Figure 16D, E). Minimal differences in levels of mucopolysaccharides were observed using Alcian Blue staining (Figure 16F). Interestingly, in *Sox9-cKO* uterine sections, we were able to detect collagen fibers in the myometrium; therefore, the reduction in collagen fibers observed in the stroma could be the result of deleting *Sox9* in the uterine epithelium.

Figure 15: Histology of adult *Sox9-cKO* uteri. (A-F) H&E stained uterine sections from control (A-C) and *Sox9-cKO* (D-F) females dissected at various time-points. (D, E) The stroma (*) of *Sox9-cKO* uteri appeared to have a lower density of cells. This difference was primarily observed during estrus. Cystically dilated glands are present in both control and *Sox9-cKO* uteri (red arrows). GE, glandular epithelium. Scale 500 μm.

	8-week-old	4-month-old	8-month-old
Control	A — GE	B — GE	C — GE
Sox9-cKO	D — * GE	E — * GE	F — GE
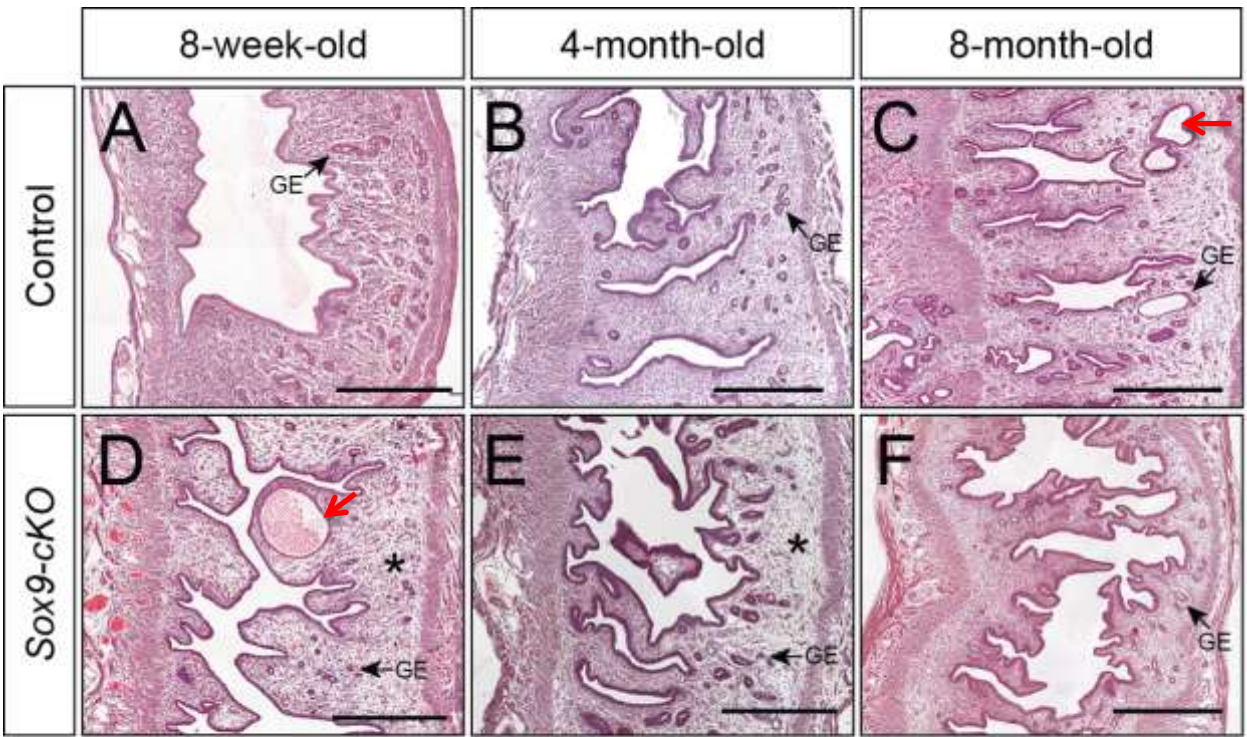
Figure 16: Reduction of collagen fibers in adult *Sox9-cKO* uterus. (A, B, D, E) Tissue sections from 4-month-old females stained by Masson's Trichrome. A reduction in collagen fibers, stained blue, was detected in the *Sox9-cKO* endometrium (D, E) when compared to controls (A, B). (C, F) Tissue sections stained by Alcian blue. No difference in levels of mucopolysaccharides or glycosaminoglycans was observed between *Sox9-cKO* and controls. Scale bar 50 μm.
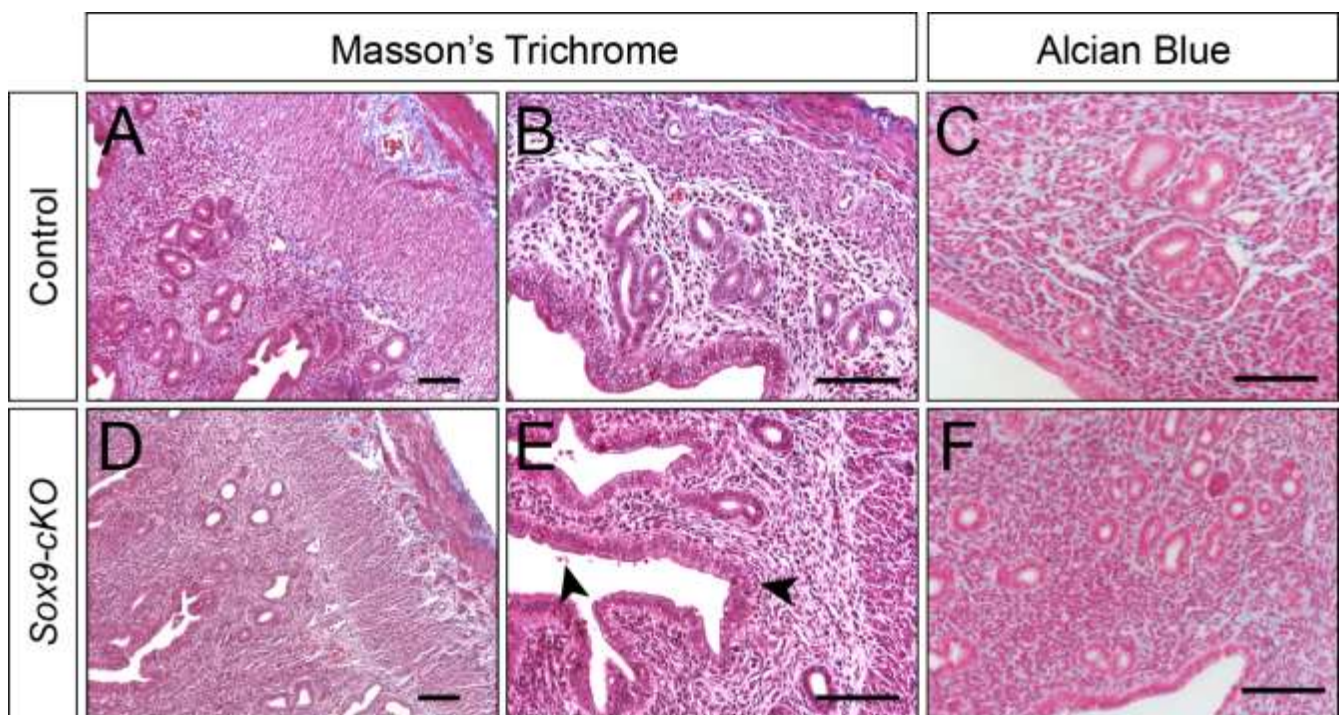
Discussion

SOX9 Promotes the Invagination of the Uterine Epithelium and Formation of Uterine Glands

The female reproductive tract develops from the Müllerian duct[7]. In XX embryos, the Müllerian duct forms as the mesonephric epithelium invaginates next to the Wolfian duct around embryonic day (E) 11.75 and reaches the cloaca by E13.5[5]. The Müllerian duct differentiates into all the components of the FRT[7]. We used *Sox9-EGFP* mice to determine the spatio-temporal expression of *Sox9* during FRT development. In these mice, *EGFP* expression was driven by the *Sox9* endogenous promoter. Therefore, detection of GFP signal by fluorescent microscopy indicated expression of *Sox9*. At E16.5, GFP was detected in the Müllerian duct epithelium. At postnatal day 1 (P1) GFP was present in part of the oviductal epithelium, the entire uterine epithelium, and the cervical epithelium. This suggested that expression of *Sox9* was maintained in the epithelium derived from the Müllerian duct.

We focused our attention to the uterine epithelium. We detected greater GFP signal in the epithelial invaginations forming radially along the entire uterine epithelium starting at P6. At P21 we observed GFP signal in the secondary creases forming perpendicular to the primary creases. We also detected SOX9 in the invaginating epithelium by immunofluorescence staining and by lineage-tracing analysis of SOX9-LP cells, strongly suggesting that *Sox9*-expressing

cells, initially present throughout the LE resolve to sites where the uterine epithelium forms creases and buds. These Sox9-LP cells, initially clustered in LE at P6/7, make up the entire GE at 8 weeks. We can then hypothesize that SOX9 contributes to the postnatal invagination of the uterine epithelium.

SOX9 plays a crucial role during invagination of the mouse otic placode[113]. In *Sox9* conditional knockout mice, the otic epithelium fails to invaginate. Furthermore, it was suggested that SOX9-downstream effectors promote strengthening of apical junction proteins that contribute to the invagination of the epithelium. In Drosophila, *Forkhead (fkh)* is known to regulate apical membrane constriction[45]. FOXA2 is the mammalian homologue of Fkh. FOXA2 can form a complex with HIF1-α and activate *Sox9*[114]. In mice, conditional inactivation of FOXA2 led to a decreased number of UGs[47]. This group conditionally inactivated FOXA2 by generating *Pgr-Cre; Foxa2 fx/fx* mice. Therefore, inactivating *Foxa2* led to a reduction in number of UGs, whereas inactivating *Sox9* did not. Perhaps, FOXA2 lies downstream of SOX9, although, FOXA2 controls gene expression of other genes essential for UG formation and maintenance. It would be interesting to determine if the levels of SOX9 are affected in these mice.

Another group demonstrated that inactivating HIF1-α reduced levels of SOX9 and SOX9-downstream targets in the condensating mesenchyme[115]. In the future, we would like to explore if the FOXA2-HIF1-α complex activates *Sox9* in the uterine epithelium, which leads to epithelial invagination. Alternatively, we would like to determine if this complex alone is sufficient to turn on the genetic program that establishes the invagination of the uterine epithelium. This would

answer the question if SOX9 is necessary for UG formation or if it is activated by FOXA2 but does not play an essential role in UG formation.

Regardless, we have linked the presence of SOX9 to epithelial invagination. Additionally, we have shown that SOX9 changes during the estrous cycle. Here, I will present three alternative hypotheses as to how SOX9 can potentially regulate UG development.

SOX9 regulate genes that promote secretion of ECM: *Col2a1*, *Col11a2*, *Col9a1*, *Aggrecan*, and *Cartilage link protein*[82-86]. We have demonstrated that there is a reduction of collagen fibers in the stroma of *Sox9-cKO* uteri. However, there was no difference in the levels of mucopolysaccharides, stained by Alcian Blue. Therefore, it is possible SOX9 is regulating epithelial invagination and subsequent adenogenesis by regulating ECM secretions. Secreted collagen fibers accumulate near the basement membrane; therefore, SOX9-expressing cells could promote areas of the epithelium to become structurally firmer than the surrounding space. We have observed at various time-points that cells undergoing mitosis appear to be devoid of SOX9, which indicates that SOX9-expressing cells do not divide as frequently as their neighboring cells. Lateral forces exerted by neighboring cells can potentially push the cells into the crevices formed between these collagen-secreting cells.

We have correlated the presence SOX9 with the initial invagination of the uterine epithelium. Additionally, we have shown that the uterus appears grossly and histologically normal following inactivating of *Sox9* in the uterine epithelium.

Perhaps, SOX9 is only necessary for the initial invagination of the uterine epithelium and subsequent formation of UGs. In mice, the process of adenogenesis starts at P6 and is completed by P14[39]. We knocked out *Sox9* at P14, after the UGs were formed. Therefore, we require a better reagent to inactivate *Sox9* in the uterine epithelium prior to UG formation.

SOX9 is activated by EGFR/MEK/ERK pathway and actively degraded by the proteasome[73]. Additionally, this group also demonstrated that SOX9 contributes to migration and invasion. In sheep, EGF and FGF7 secreted from the mesenchyme activate the FGFR2-IIIb found in the LE[65]. Activation of the RTKs leads to enhanced MEK/ERK signal, which phosphorylates and activates SOX9. Phosphorylation of SOX9 by Protein Kinase A (PKA) promotes EMT in neural crest cells by activating *Snail2*[116]. Furthermore, SOX9 promotes neural crest migration by upregulating SLUG[117]. Therefore, by promoting cell migration and invagination and possibly even lowering the rate of division, SOX9-expressing cells promote the initial invagination of the uterine epithelium. However, once the UGs form, SOX9 becomes unessential for tissue homeostasis.

SOX9 is known to regulate β-CATENIN. SOX9 was described to promote β-CATENIN nuclear-export and degradation[68,118]. Conversely, activated β-CATENIN inhibits expression of *Sox9* by binding to and sequestering SF1[119]. Uterine glands are maintained in close contact with the myometrium, where presumably FGF7 is expressed[65]. Downstream effector ERK positively regulates *Sox9* expression, while SOX9 inhibits β-CATENIN. In the neuroectoderm, Wnt

signaling promotes ectodermal fate specification by blocking the ability of the cells to respond to FGFs[120]. If Wnts somehow block Fgf signaling early during embryo development, perhaps, Wnts expressed in the LE and the stroma adjacent to the LE, actively block Fgf signaling from the myometrium and stroma. SOX9 downregulates Wnt signaling, thus, allowing Fgf signaling to prevail and activate downstream effector. One downstream effector is SOX9 itself. By allowing Fgf signal to activate gene expression, while downregulating β-CATENIN, SOX9 possibly activate a genetic network that established a glandular epithelial identity. Therefore, SOX9 contributes to the differentiation of the glandular epithelium.

SOX8 and SOX10 Compensate for the Loss of SOX9

Sox9 was conditionally knocking out in the lung epithelium[101]. No phenotypical abnormalities were observed in these mice. Inactivating *Sox9* during kidney development did not affect normal development either[121]. However, inactivating both *Sox8* and *Sox9* disrupted the process of branching morphogenesis. Conditionally knocking out *Sox9* did not disrupt UG homeostasis. All three members of the SoxE subfamily (SOX8, SOX9, and SOX10) are known to have overlapping expression patterns and to share a functional redundant redundancy[78]. *Sox8* mutant mice are viable and show no detectable phenotypic abnormalities. It is thought that the other two members can compensate for the loss of SOX8. Preliminary studies using an antibody that

detected both SOX8 and SOX10, showed positive signal in the mouse uterine epithelium (data not shown). Microarray data demonstrated that *Sox10* is expressed in the human endometrium[111]. To bypass the potential functional redundancy caused by the other two *SoxE* genes, future experiments would require knocking out two or possibly all three genes.

Chapter IV: Overexpression of *Sox9* in the Uterine Epithelium Causes Endometrial Gland Hyperplasia

Introduction

In 2012, it is estimated that 47,130 women will be diagnosed with endometrial cancer in the United States, and this malignancy will prove to be fatal for 8,010[26]. Uterine adenocarcinoma is the most prevalent type of endometrial cancer arising from uncontrolled growth of the GE. SOX9 is present in the nuclei of the adult uterine GE. In previous chapters, we have presented evidence to link SOX9 with invagination of the uterine epithelium and subsequent formation of UGs. SOX9 has also been linked to colorectal cancer, prostate cancer and lung adenocarcinoma[122-124]. SOX9 is activated by fgf signaling. Mutations that result in a constitutively active form of the FGFR2-IIIb have been discovered 12% of endometrial cancers[125]. Moreover, high levels of SOX9 have been detected in human uterine cancers (Dr. Broaddus, personal communication); consequently, we hypothesized that overexpressing SOX9 would contribute to the development of uterine cancer. To examine the possibility that *Sox9* drives uterine tumorogenesis, we conditionally overexpressed *Sox9* in the uterine epithelium and allowed the females to age.

We used the *Pgr-Cre* mice to overexpress *Sox9* in the uterine epithelium. The *Pgr* is expressed in the mouse uterine epithelium starting at P14. Therefore, we anticipated *Sox9* would be overexpressed in the uterine epithelium starting at

P14. Upon reaching sexual maturity *Pgr* is also expressed in the stroma and myometrium. Thus, we also expected ectopic expression of SOX9 in the stroma and myometrium. Regardless, the *Pgr-Cre* mouse line was the best reagent available at the time we started this project since Cre should not be as widely expressed when compared to other tissue specific Cre-expressing mouse lines.

Pgr-Cre mice were mated with *Sox9* overexpressing mice (*CAG-loxP-mRFP1-stop-loxP-SOX9-Ires-EGFP) mice*[126]. Upon Cre-mediated recombination and excision of the DNA sequence flanked by *loxP* sites, the SOX9 overexpressing allele becomes constitutively activated. The progeny of cells where Cre-mediated recombination took place should have inherited the constitutively activated SOX9 overexpressing allele. We analyzed the immediate effect of overexpressing *Sox9* in the uterine epithelium by dissecting FRTs from prepubescent females. Additionally, we aged females to determine the effect of prolonged expression of *Sox9* in the epithelium, stroma, and myometrium.

Material and Methods

Mice

Pgr-Cre mice[106] were obtained from Dr. Franco DeMayo (Baylor Medical Center). *Sox9* overexpressing mice (*CAG-loxP-mRFP1-stop-loxP-SOX9-Ires-EGFP) mice*[126] were obtained from Dr. Haruhiko Akiyama (Kyoto University). All mice were maintained on a C57BL/6J x 129/SvEv mixed genetic background. All

animals were maintained in compliance with the Public Health Service Policy on Humane Care and Use of Laboratory Animals, the U.S. Department of Health and Humane Services Guide for the Care and Use of Laboratory Animals, and the United States Department of Agriculture Animal Welfare Act. All protocols were pre-approved by the University of Texas M.D. Anderson Cancer Center Institutional Animal Care and Use Committee.

Polymerase Chain Reaction- See Material and Methods in Chapter III.

H&E Staining- See Material and Methods in Chapter III.

Masson Trichrome Staining- See Material and Methods in Chapter III.

Alcian Blue Staining- See Material and Methods in Chapter III.

Immunofluorescent Staining- See Material and Methods in Chapter III.

TUNEL Staining- See Material and Methods in Chapter III.

Results

Generating *Pgr-Cre; Sox9* Conditionally Overexpressing *(cOE)* Mice

We observed minor morphological changes in the FRT after inactivating *Sox9*, indicating that homeostasis was not greatly affected, possibly due to the redundant action of the two other SoxE genes: *Sox8* and *Sox10*. Conversely, we decided to continuously overexpress *Sox9* using the same *Pgr-Cre* mouse line to explore the effect of overloading the system with SOX9. *Pgr-Cre* mice were

mated with *CAG-loxP-mRFP1-stop-loxP-Sox9-EGFP* (*CAG-Sox9)* mice. *CAG-Sox9* mice constitutively express RFP. Upon Cre-mediated excision of the stop signal *Sox9* cDNA and EGFP become constitutively expressed. *Pgr-Cre/+; CAG-Sox9/+* males were crossed with homozygous *CAG-Sox9/CAG-Sox9* females to generate *Pgr-Cre/+; CAG-Sox9/CAG-Sox9* (***Sox9-cOE***) females (Figure 17). The progeny inherited the Cre allele following Mendelian patterns of inheritance.

To analyze the effect of overexpressing *Sox9* in the epithelium, we focus our analysis on P21, 28, and 35, since the Cre is presumably expressed after P14. We dissected the female reproductive organs and measured the length of the uteri (n= 48). No statistical difference was observed when comparing *Sox9-cOE* and control littermates at these stages (data not shown). In prepubescent females, gross examination revealed no morphological differences between *Sox9-cOE* and control FRTs. All the constituent organs (two ovaries, two oviducts, two uterine horns, a cervix and the upper vagina) were present in all the FRTs dissected. We examined the female reproductive organs at later time-points, 8 weeks, 8 months, and 1-year-old.

Gross examination revealed morphological differences between control and *Sox9-cOE* uteri at 1 year (Figure 18). Under the dissecting microscope, we observed cystoid structures inside the uteri of 1-year-old *Sox9-cOE* females (Figure 18E-H, arrowheads). In control females, we observed 1-2 cystoid structures (Figure 18C, arrowhead) along the entire length of the uteri. In comparison, many small to large cystoid structures were present in the uteri of *Sox9-cOE* females.

Figure 17: Genetic strategy used to conditionally overexpress *Sox9* in the uterus. (A) Founding mice on top were crossed to generate *Pgr-Cre; CAG-Sox9-OE* mice, WT; *CAG-Sox9-OE* and WT; WT mice. (B) *Sox9-OE* allele. mRFP is constitutively expressed driven by the CAG promoter. (C) Mice that inherit the *CAG-Sox9-OE* allele express RFP in the entire FRT. (D) Upon Cre-mediated excision of the RFP sequence, cells that express *Pgr* also express GFP and *Sox9* cDNA.

A

Pgr-Cre   CAG-Sox9-OE

Pgr-Cre; CAG-Sox9-OE
(Sox9-cOE)

WT; CAG-Sox9-OE
(Control)

WT
(Control)

B

CAG-Sox9-OE

loxP   loxP   X

CAG
promoter | mRFP1-STOP | | Sox9 cDNA | ires-EGFP

C

WT   WT; *CAG-Sox9-OE*   WT   WT; *CAG-Sox9-OE*
Control   Control   Control   Control

D

Cre

loxP

CAG
promoter | Sox9 cDNA | ires-EGFP

Pgr-Cre; CAG-Sox9-OE
(Sox9-cOE)

99
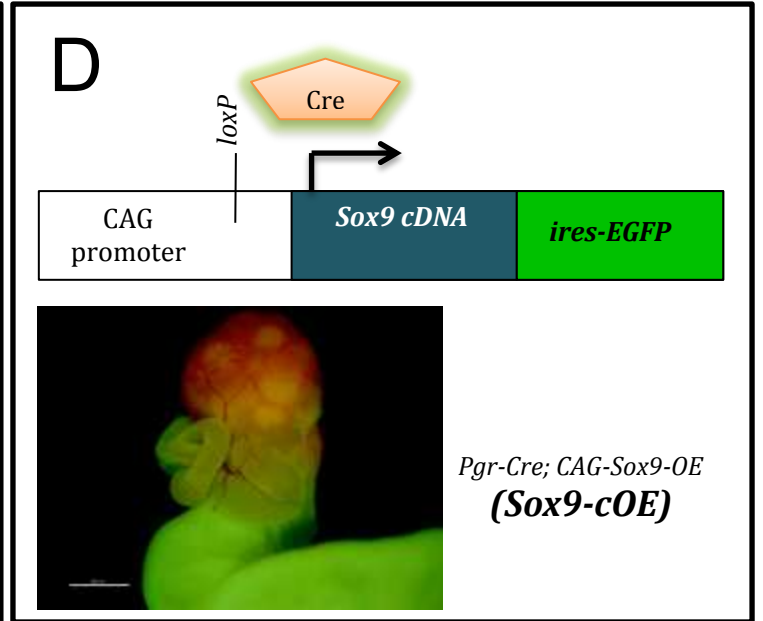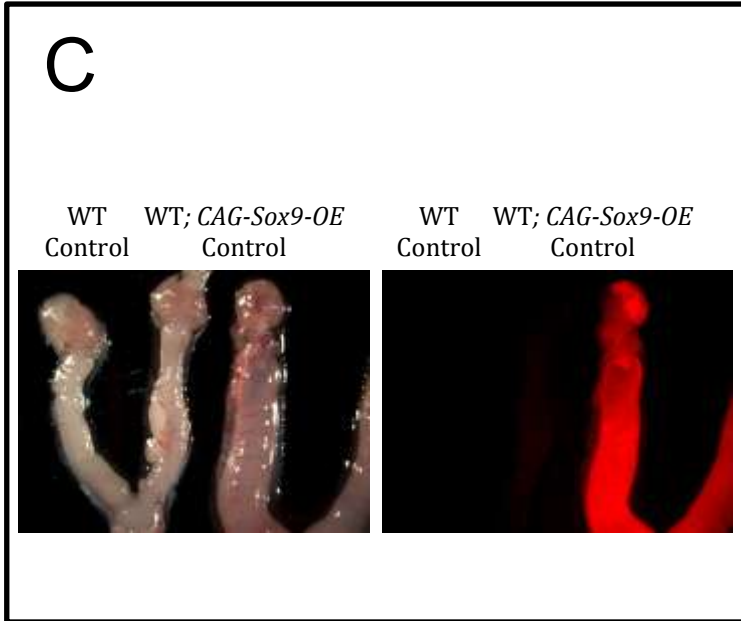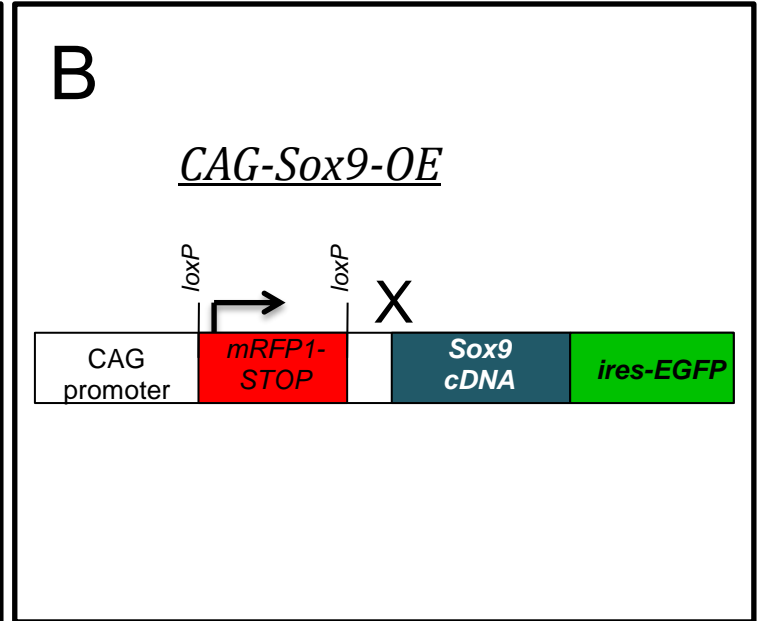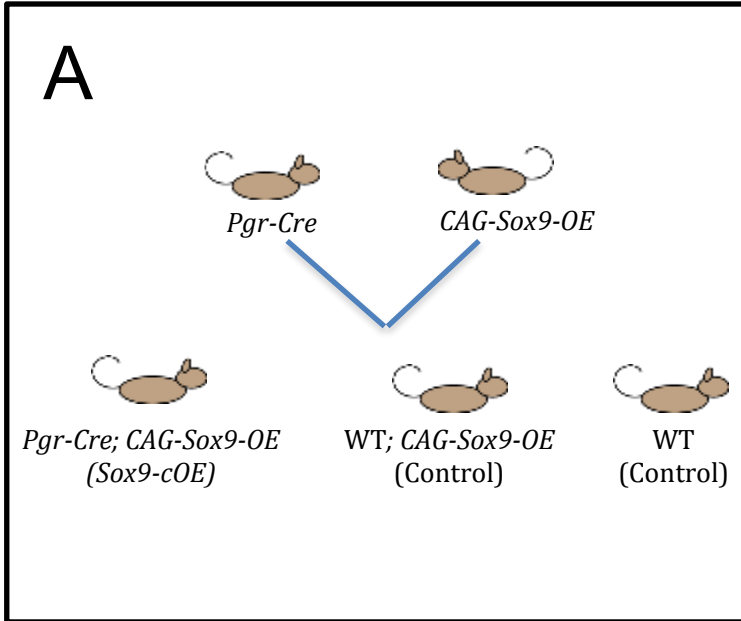
Figure 18: **Gross morphology of Sox9-*cOE* uteri.** Brightfield images of 1-year-old uteri. (B, D, F, H) Uteri sectioned longitudinally (mesometrial side on top). (B, D) 1-2 cystic structures observed inside the control uteri (arrowhead). (E, G) Multiple cystic structures (arrowheads) present inside the uteri of *Sox9-cOE* females. (H) Note that these cystic structures were also present in the mesometrial side (*). Scale bar 2 mm.
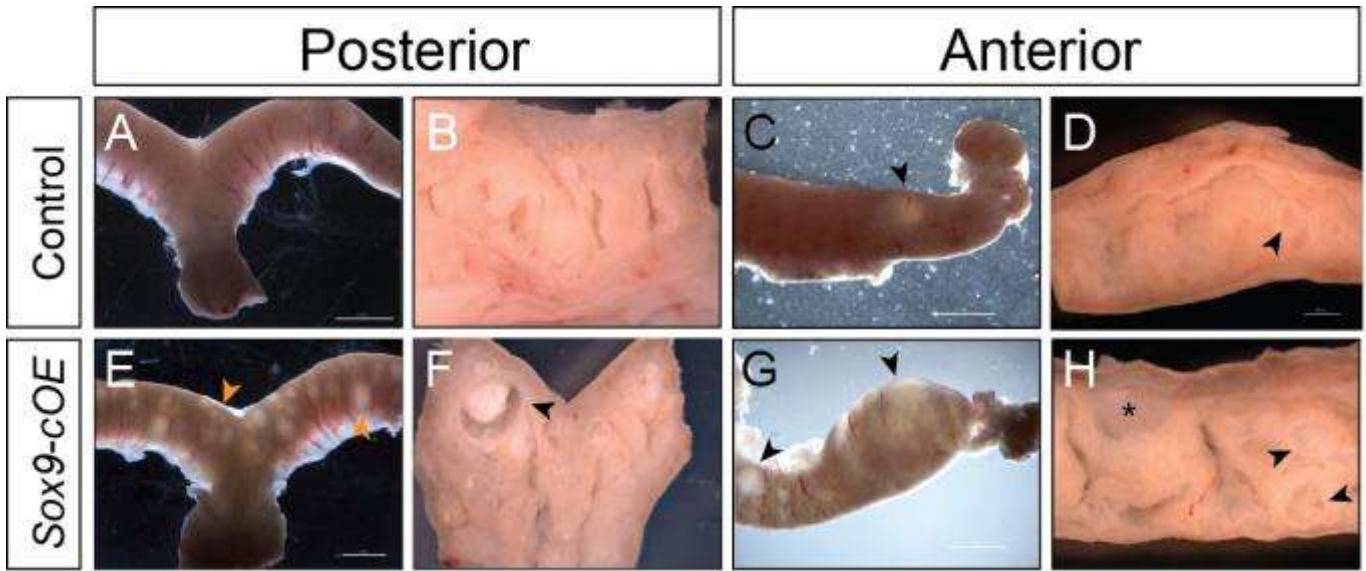
A longitudinal incision along the length of the uterus revealed that the cystic structures were filled with white matter (Figure 18H, asterisk). Additionally, the epithelial creases appeared deeper in *Sox9-cOE* uteri when compared to controls.

Histological Analysis of *Sox9-cOE* Uteri

We performed similar histology as when comparing *Sox9-cKO* and control females. Tissues collected at various time points were sectioned in the transverse plane (cross-sections) and longitudinal plane of the entire reproductive tract. Tissue sections were stained with H&E, Masson's Trichrome or Alcian Blue.

The major morphological difference observed in *Sox9*-cKO tissue sections was that the stroma appeared less cellular that age-matched controls. Correspondingly, the stroma of *Sox9-cOE* uteri appeared denser (Figure 19C), indicating it had become fibrotic. The LE and GE were arranged in a simple columnar epithelial layer in both control and *Sox9-cOE* mice (Figure 19C-F).

Examination of 8-month-old and 1-year-old *Sox9-cOE* uterine sections revealed consistent morphological abnormalities; stromal fibrosis and cystically dilated UGs (Figure 20). Both morphological abnormalities, although mostly prevalent in 8-month-old and 1-year-old *Sox9-cOE* uterine tissue samples, were also observed rarely in 8-week-old uterine sections (Figure 19C).

Figure 19: Histology of adult *Sox9-cOE* uteri. (A-F) H&E stained uterine sections from control (A-C) and *Sox9-cOE* (D-F) females dissected at various time-points. (D, F) The stroma of *Sox9-cOE* uteri appeared denser and contained cystically dilated UGs. GE, glandular epithelium. Scale 500 μm.

	8-week-old	4-month-old	8-month-old
Control	A GE	B GE	C GE
Sox9-cOE	D GE	E GE	F GE
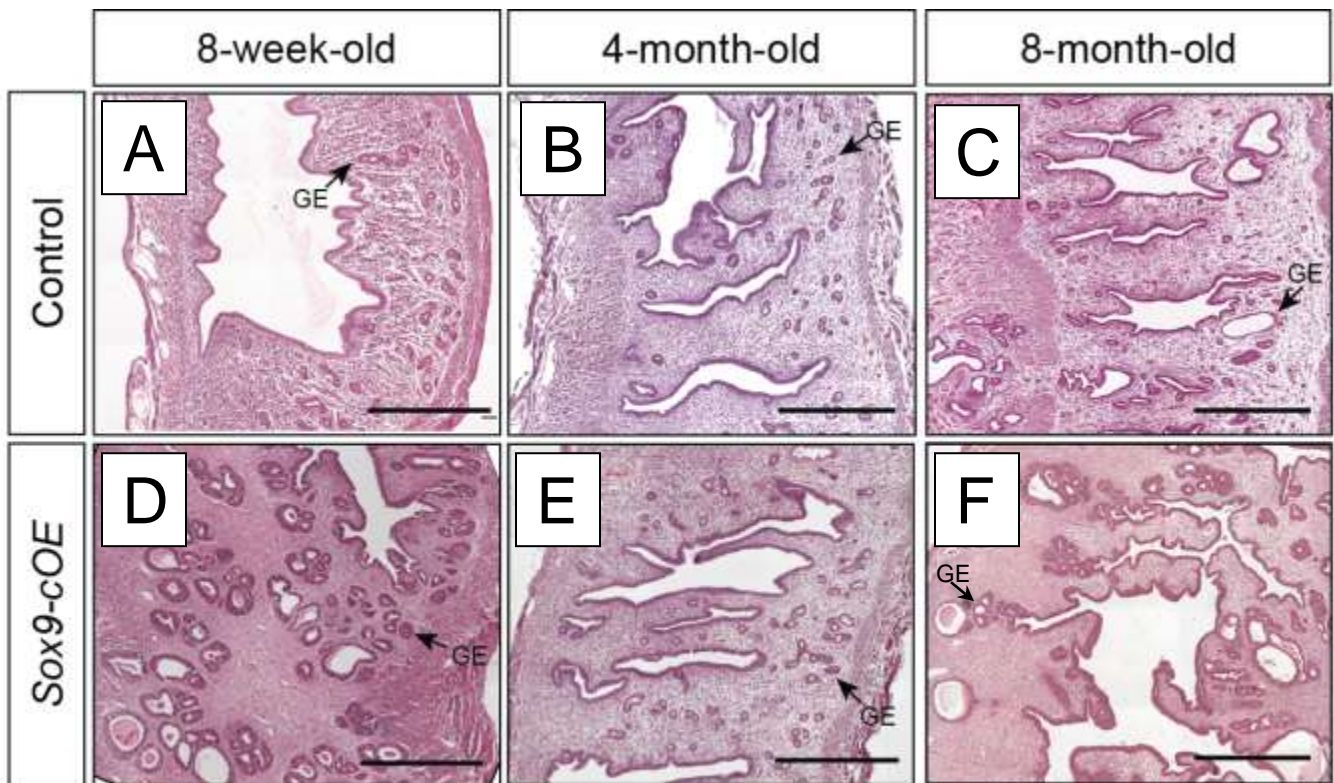
Figure 20: Endometrial lesions observed in *Sox9-cOE* females. H&E sections from 1-year-old (A, B, F) and 8-month-old (C, D, E) *Sox9-cOE* females. Multiple cystically dilated UGs observed on cross sections (A) and longitudinal sections (B). (C-F) Crowded UGs showing cribriform appearance (black arrowheads) present in the endometrium. Thick-walled blood vessels (*) observed in the stroma. Scale bar, 50 µm.
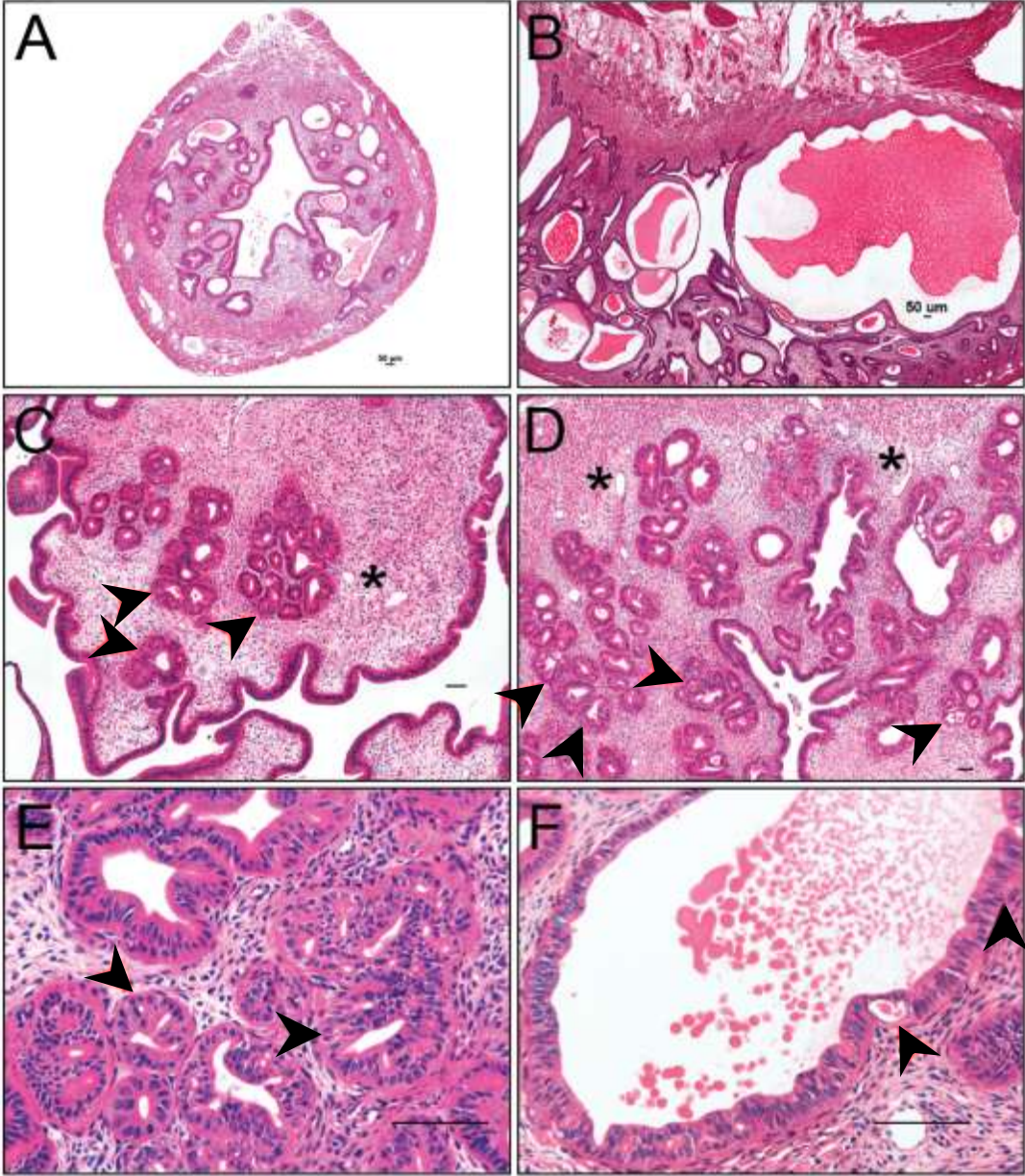
However, uterine sections obtained from 1-year-old *Sox9-cOE* uterine sections displayed multiple large cystically dilated UGs along the length of the uterus (Figure 20B). These cysts appear to encroach into the endometrium, overloading the uteri with secretions (Figure 20F, black arrowhead). The secretions appeared to be confined to the cysts. We observed that the glandular lumen was connected to the uterine cavity; therefore we were unable to explain why the lumen of cystically dilated glands was overloaded with secretions. However, we observed secretions inside sections of the GE that appeared to contain ectopic lumens (Figure 20F, black arrowhead).

Histologically, the morphological abnormalities present in *Sox9-cOE* female uteri appeared similar to that observed in human endometrial polyps[27], although we did not discern any polyps inside the uterine cavity. Thus, we termed the morphology "polypoid-like". We also noted the presence of UGs within the myometrium (Figure 21A). In women, the presence of ectopic UGs within the myometrium characterizes a medical condition known as adenomyosis[127]. Adenomyosis is a common lesion observed in human endometrial polyps. Additionally, we observed "thick-walled" blood vessels (Figure 20, asterisk; Figure 21, white arrowhead), another common key feature of endometrial polyps. The earliest time-point in which we observed a polypoid-like histology in *Sox9-cOE* females was in tissue sections of an 8 week-old female (Figure 19C).

Figure 21: Endometrial polyp-like lesions observed in *Sox9-cOE* females.
(A-D) Uterine sections from *Sox9-cOE* females stained by Phalloidin (green) and DAPI (blue). Showing mRFP1 in tissues were Cre was not expressed (i.e. blood vessels). (A, C) UGs present within the myometrium (black arrowheads). (B) Magnified image from (A) to display the depth of lumen in cystically dilated glands (asterisk). (D) Showing blood vessel present near the cystically dilated UG (white arrowhead). (E-H) Immunofluorescent staining of the human (E, F) and *Sox9-cOE* (G, H) mouse uterus using an α-SOX9 antibody (green). Nuclei were stained with DAPI (black). (E, G) An α-E-Cadherin antibody was used to mark the epithelium. (E, F) The GE of cystically dilated UG in a human endometrial polyp displays a reduction in nuclear localized Sox9 (*). (G, H) Likewise, mice uterine sections show a reduction in levels of Sox9. Sox9, green; E-Cadherin, red. Scale bar, 50 µm.
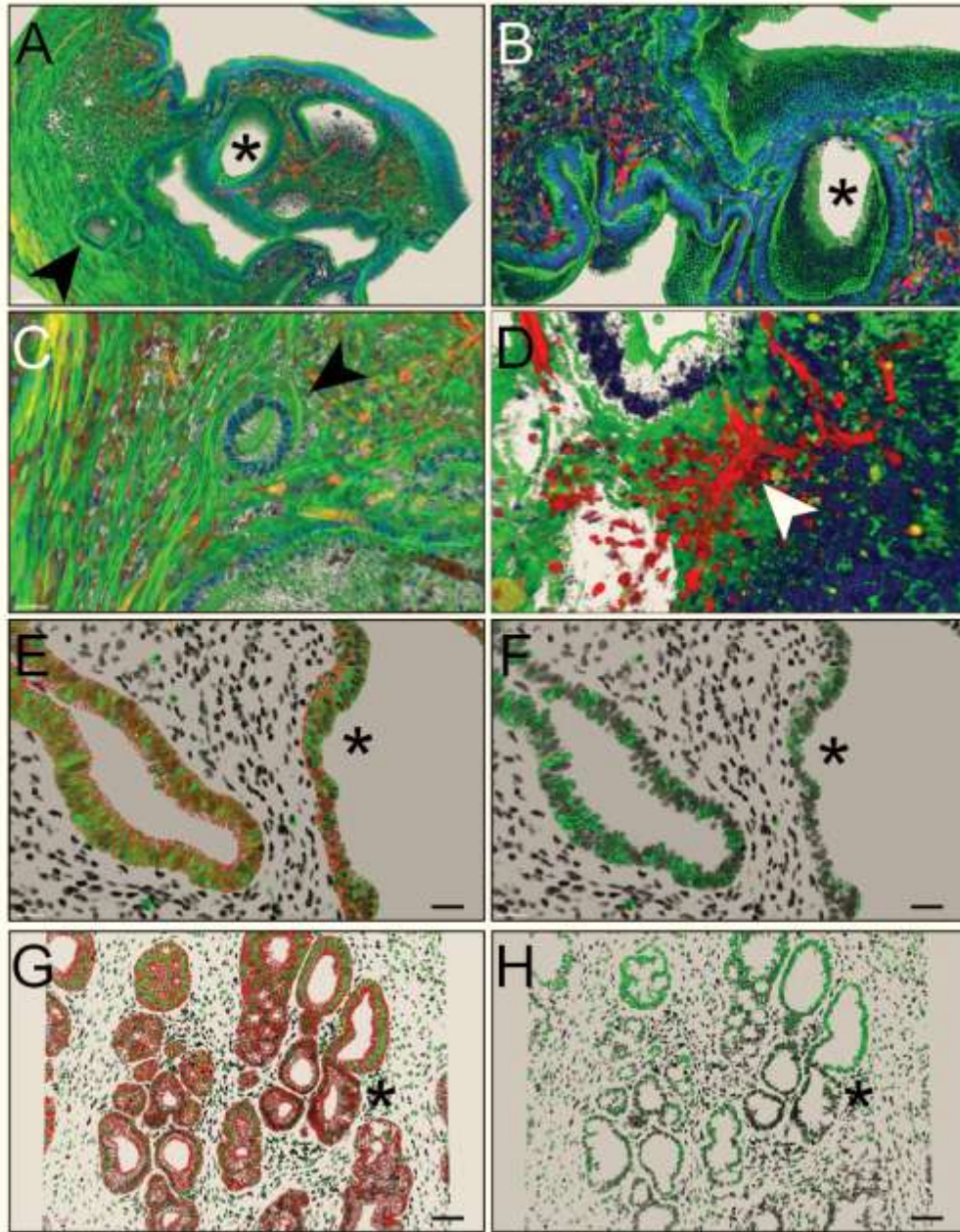
Therefore, it appears that by overexpressing *Sox9* in the epithelium, and some parts of the stroma, the cells acquire the characteristic stromal fibrosis and cystically dilated morphology observed in tissue sections of human endometrial polyps.

We performed a thorough examination of uterine slides from 8-month and 1-year-old *Sox9-cOE* females and examined uterine glands that displayed potentially premalignant cytological and architectural abnormalities. In some forms, the glands were microscopically dilated, comparable to what is seen in human simple endometrial hyperplasia. In other forms, the glands were in a more cribriform, crowded fashion, similar to what is seen in human complex endometrial hyperplasia. Contrary to our expectations, SOX9 was lost in part of the uterine glands showing cribriform lesions (Figure 21G, H; Figure 21A, B).

We stained tissue sections displaying endometrial polypoid-like lesions with Phalloidin to mark the actin cytoskeleton (Figure 16A-D). We observed UGs within the myometrium (Figure 16, black arrowhead) and thick blood-vessels (white arrowhead). Overall, the cellular morphology observed in adult *Sox9-cOE* samples portrayed the "hallmarks" endometrial lesions known to be present in endometrial polyps. Moreover, the presence of cribriform foci indicates progression into premalignant endometrial lesions. Since we observed that the GE showing cribriform foci had sections devoid of SOX9, we decided to investigate if SOX9 was also downregulated (Figure 21G, H) in human endometrial polyps. Dr. Russell Broaddus (M.D. Anderson Cancer Center) kindly provided us with tissue sections derived from human endometrial polyps.

Immunofluorescent staining against SOX9 revealed that cystically dilated UGs express SOX9 in the cytoplasm but not in the nucleus (Figure 21 E, F). Unlike in human samples, where we detected cytoplasmic SOX9, in *Sox9-cOE* uterine sections, we observed a total loss of SOX9 in parts of the hyperplastic uterine glands (Figure 16G, H).

We took high-resolution images of cribriform foci to examine the formation the ectopic lumens inside the GE (Figure 22). The nuclei were positioned very close to the basement membrane (Figure 22C-F). We observed two cells forming an ectopic lumen (Figure 22E, F). Their nuclei were positioned near to the basement membrane to which the epithelia attaches. Additionally, we noted that there were cells in the apical side to the epithelium that seem to maintain the continuum of the epithelial sheet (Figure 22E, F).

SOX9 is known to regulate extracellular matrix (ECM) gene transcription. We stained uterine sections using both Mason's Trichrome and Alcian Blue protocols. By Mason's Trichrome staining, we detected an excess of collagen fibers in uterine sections derived from *Sox9* overexpressing females (Figure 23D, E). Since SOX9 is well known to activate *Col2a1* in chondrocytes, it is possible that SOX9 is upregulating genes that play a role in extracellular membrane deposition and secretion. The levels of mucopolysaccharides, observed by Alcian Blue staining, remained unchanged in *Sox9-cOE* uteri (Figure 23F).

Figure 22: Immunofluorescent staining of UGs displaying a cribriform appearance. (A, F) Sections stained using α-SOX9 (green) and α-E-Cadherin anitbodies (red). (B) Displaying only green channel to show loss of SOX9 in areas containing endometrial lesions (black arrowhead). (C-F) UGs showing crowding of the GE and formation of cribriform foci. Ectopic lumens present on cribriform foci. (SOX9, green; DAPI, blue; E-Cadherin, red) Scale bar, 10 μm.
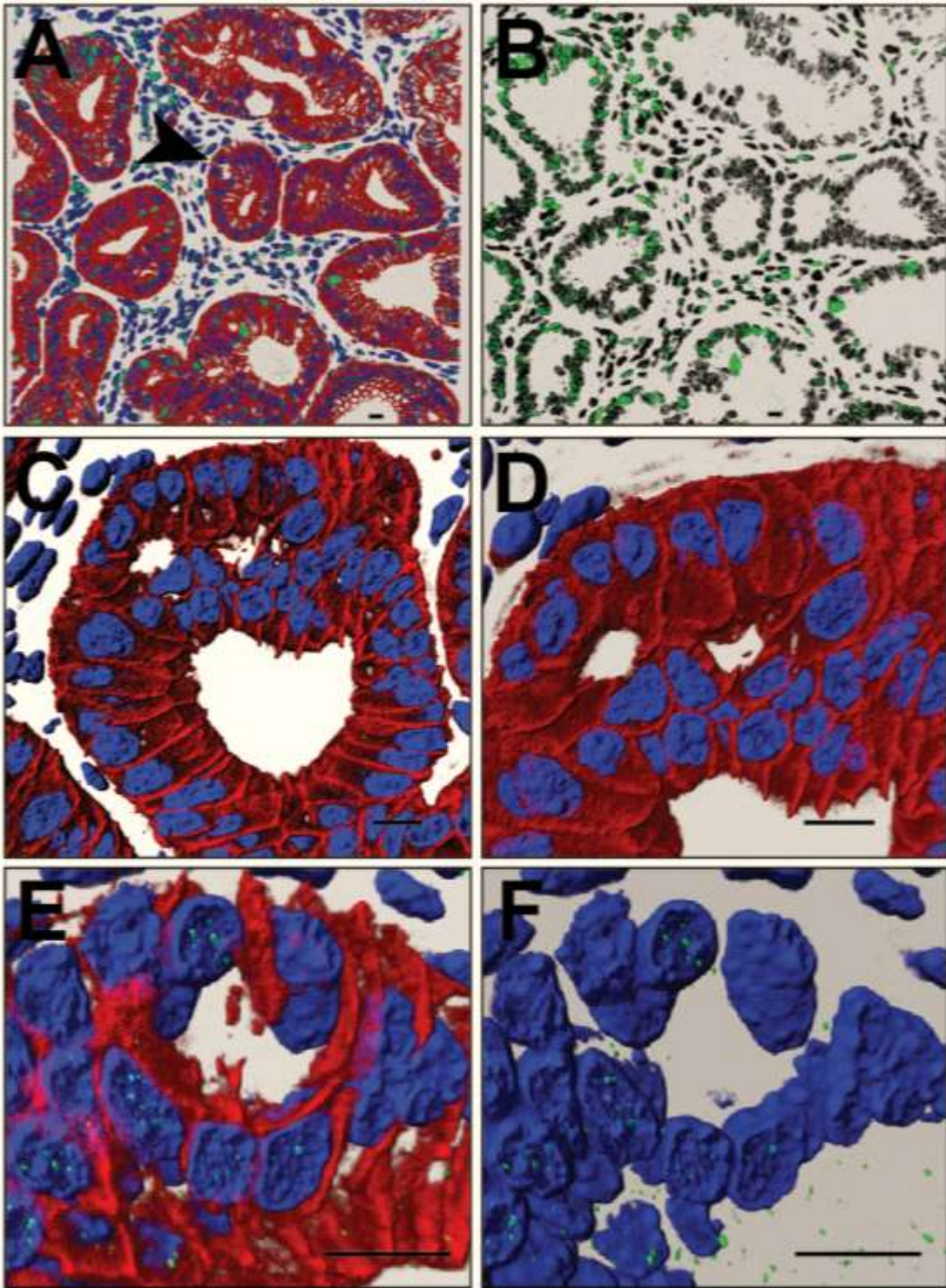
Figure 23: Increase of collagen fibers in adult *Sox9-cKO* uterus. (A, B, D, E) Tissue sections from 4-month-old females stained by Masson's Trichrome. An increase in collagen fibers, stained blue, was detected in the *Sox9-cOE* endometrium (D, E) when compared to controls (A, B). (C, F) Tissue sections stained by Alcian blue. No difference in levels of mucopolysaccharides or glycosaminoglycans was observed between *Sox9-cOE* and controls. Scale bar 50 μm.
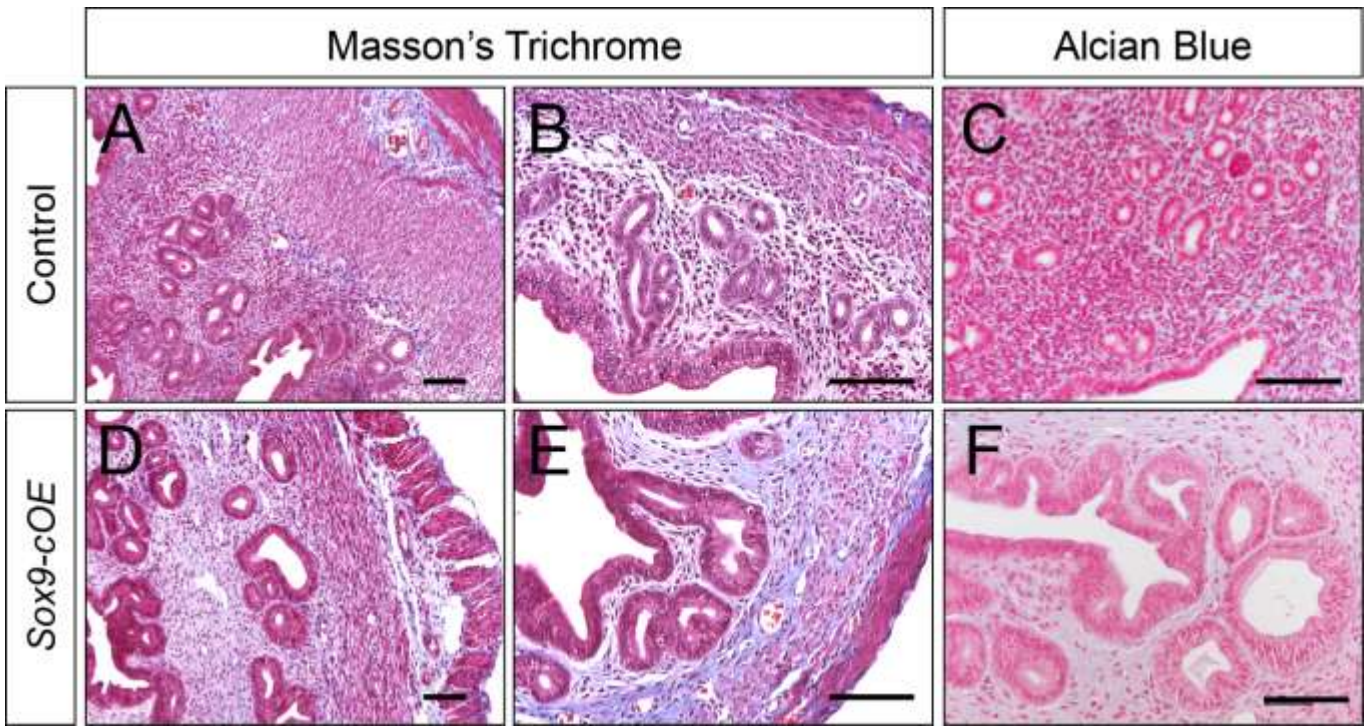
Determining when *SOX9* is Inactivated and Overexpressed Post Cre Expression

Pgr-Cre mice were previously generated by knocking in Cre into the genomic region that encodes for the first exon of the *Pgr* gene[106]. The group that generated this mouse line performed a lineage-tracing analysis experiment by crossing these mice to *Rosa-26-reporter* mice. They reported LacZ expression in the LE and GE at P14. Minimal LacZ signal was detected in the stroma and the myometrium. Sexually mature females (~6 weeks) showed a similar pattern of LacZ expression in the uterine epithelium to that observed at P14. However, LacZ signal was also detected in the stroma and the myometrium in adult females. Taking in consideration this expression pattern, we presumed that Cre would inactivate or overexpress *Sox9* in the LE and GE around P14. We also realized that upon females reaching sexual maturity *Sox9* should be inactivated in the subepithelial stroma and in the myometrium. Sox9 is not expressed in the stroma, thus knocking it out should not affect the normal function of the stroma. However, ectopic expression of *Sox9* in the stroma and myometrium after females reached sexual maturity could have potentially altered the endometrial homeostasis.

Regardless, of what has been described in the literature, we needed to determine when SOX9 is overexpressed in the uterine epithelium of *Sox9-cOE* females. Additionally, we needed to establish when *Sox9* is ectopically expressed in the stroma and myometrium. At the same time, we identified when

SOX9 is downregulated in the *Sox9-*cKO females. We began examining uterine tissues for the presence of SOX9 at P21, presuming that one week was enough time to completely inactivate *Sox9* in the uterine epithelium of *Sox9-cKO* females. Although we expected Sox9 levels to rise in the uterine epithelium of *Sox9-cOE* females at P21, we anticipated that ectopic expression of *Sox9* in the stroma and myometrium should not be observed until the females reached sexual maturity.

Immunofluorescent staining revealed diminished levels of SOX9 in *Sox9-cKO* uteri at P21 (Figure 24A, B). We also detected low levels of ectopic expression of SOX9 in the myometrium and in the stroma in *Sox9-cOE* uterine sections (Figure 24M, N). At P28, we detected low levels of SOX9 in the uterine epithelium of *Sox9-cKO* females (Figure 24C, D). Conversely, we did not find measurable differences in the levels of SOX9 in the uterine epithelium of *Sox9-cOE* females at P28 (Figure 24O-P). However, we discerned low levels of SOX9 ectopically expressed in the uterine stroma of *Sox9-cOE* females at P28 (Figure 24O-P). At P35, SOX9 was expressed in the GE of *Sox9-*cKO uteri, although at lower levels when compared to age-matched control females (Figure 24E, F, K, L). SOX9 was almost completely absent in the LE of *Sox9-*cKO uteri. The cells maintaining SOX9 expression in the *Sox9-*cKO were observed in groups or clumps instead of single cells randomly in the uterine epithelium (Figure 24F). In age-matched *Sox9-cOE* females*,* we observed a striking increase in the levels of SOX9 in both the LE and GE (Figure 24Q, R) when compared to control females.

Figure 24: Determining when *Sox9* is inactivated/ overexpressed. (A-R) Immunofluorescent staining using α-SOX9 (green) and α-E-Cadherin (red) antibodies at various time-points. Uteri from Sox9-*cKO* (A-F), control (G-L), and *Sox9-cOE* (M-R) females. (B, D, F, H, J, L, N, P, R) DAPI signal removed to emphasize SOX9 (green). (A-F) Decreased levels of SOX9 observed in the LE of uteri from *Sox9-cKO* at P35 (E, F) when compared to controls (K, L). Increased levels of SOX9 observed in the LE and GE of uteri from *Sox9-cOE* at P35 (Q, R) when compared to controls (K, L). Ectopic expression of SOX9 detected in the stroma and myometrium of uteri from *Sox9-cOE* at P28 (O, P) and P35 (Q, R). Sox9, green; DAPI, blue; E-Cadherin, red. Scale bar, 50 μm.
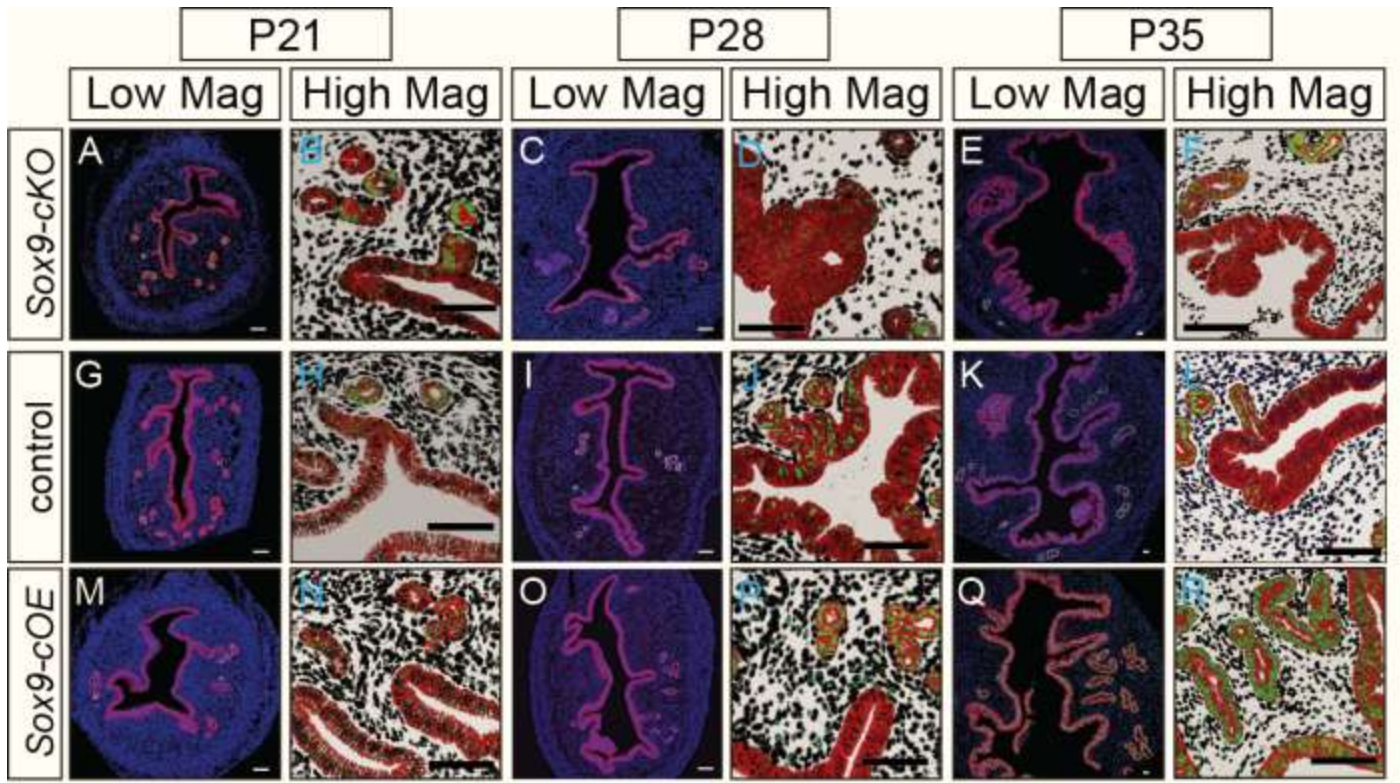
We also observed cells in the stroma and myometrium that displayed nuclear localized SOX9. There is a possibility that the low-levels of ectopic expression of SOX9 observed in the stroma and myometrium could be contributing to the stromal fibrosis in *Sox9-cOE* uteri.

Proliferation, Apoptosis and Morphometrical Analysis

The endometrium undergoes rapid cycles of proliferation, differentiation, and apoptosis during the estrous cycle. To determine the stage of the estrous cycle the female was experiencing, we collected vaginal smears for at least three consecutive days. Collecting samples can affect the uterine epithelium. For example, after performing various vaginal smears, the probability of inflicting a bacterial infection increases over the number of days we collect samples; this creates another variable that might interfere with our results. We decided to only perform a vaginal smear prior to sacrificing the females. Concomitant with the gross examination and cellular morphology, we were able to estimate the stage of the estrous cycle. Nonetheless, this was a crude estimation and the cellular morphology changes very rapidly from one stage to the next. We even observed differences in proliferation and apoptosis in control female uteri dissected at the same stage of the estrous cycle.

We compared tissue sections generated from mutant and control adult females. No major differences in cell proliferation in tissue sections stained with α-Ki67 (Figure 25) and phosphohistone H3 (Figure 26) were detected. All three

genotypes, *Sox9-cKO*, control, and *Sox9-cOE* displayed high levels of Ki67-positive staining in the LE during estrus, while during diestrus the number of Ki67-positive LE cells became almost negligible (Figure 25A, B, E, F, K, L). In the GE, we observed low numbers of Ki67-positive cells during estrus. During diestrus, the GE of both control and *Sox9-cOE* showed positive staining against Ki67 (Figure 25G, H, K, L) while the majority of the GE in *Sox9-cKO* females were devoid of Ki67 (Figure 25C, D). This experiment was performed in longitudinal sections; therefore, we were able to see that almost all UGs were Ki67-negative during diestrus. Additionally, there is a slight increase in the number of Ki67-positive cells in the LE during estrus (Figure 25A, B). However, when we examined the number of cells undergoing mitosis, by staining with α-phosphohistone H3 antibody, we were unable to observe any measurable difference between all three genotypes (Figure 26). This indicates that although there is a decrease in levels of Ki67 in the GE of *Sox9-cKO*, the uterine epithelium, both GE and LE, undergo similar rates of cell division.

Metestrus is marked by a massive wave of cell apoptosis and tissue breakdown as both estrogen and progesterone levels decline[128]. To determine if there was any change in the number of cells undergoing apoptosis, we performed TUNEL staining on tissue sections derived from uteri dissected during metestrus. This method allowed us to detect DNA fragmentation, which was visualized under the fluorescent microscope. Staining revealed that all three genotypes contained comparable levels of fragmented DNA in the area between the epithelium and the stroma (Figure 27).

Figure 25: Proliferation in adult uteri assayed by α-Ki67 antibody staining.

(A-L) Immunofluorescent staining using α-SOX9 (green) and α-Ki67 (red) antibodies on the adult mouse uterus. Ki67 marks proliferating cells. Stained with DAPI (blue). Minimal differences observed when comparing levels of Ki67 positive cells between *Sox9-cKO* (A-D), control (E-H) and *Sox9-cOE* (I-L). Sox9, green; Ki67, red. Scale bar, 50 μm.
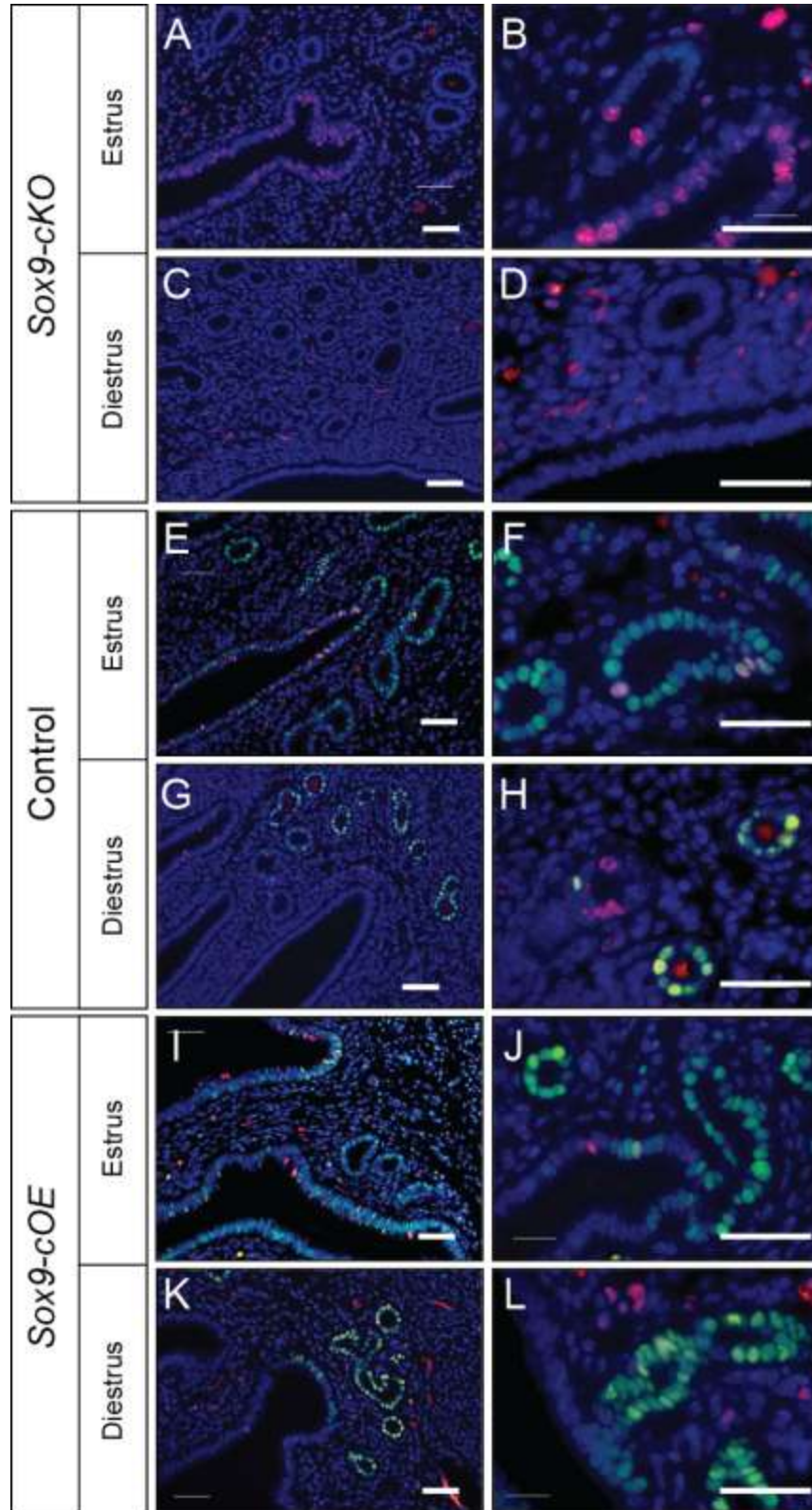
Figure 26: Immunofluorescent staining against α-Phosphohistone H3 in the adult uteri. (A-F) (A-L) Immunofluorescent staining using α-phosphohistone H3 (green) on the adult mouse uterus. Phosphohistone H3 is a marker of cells undergoing mitosis. Stained with DAPI (blue). (A, C, E) Showing uterine sections from *Sox9-cKO,* control, and *Sox9-cOE* during proestrus. (B, D, F) Displaying tissue sections dissected during diestrus. Phosphohistone H3, green; DAPI, blue. Scale bar 50 μm.

	Proestrus	Diestrus
Sox9-cKO	A	B
Control	C	D
Sox9-cOE	E	F
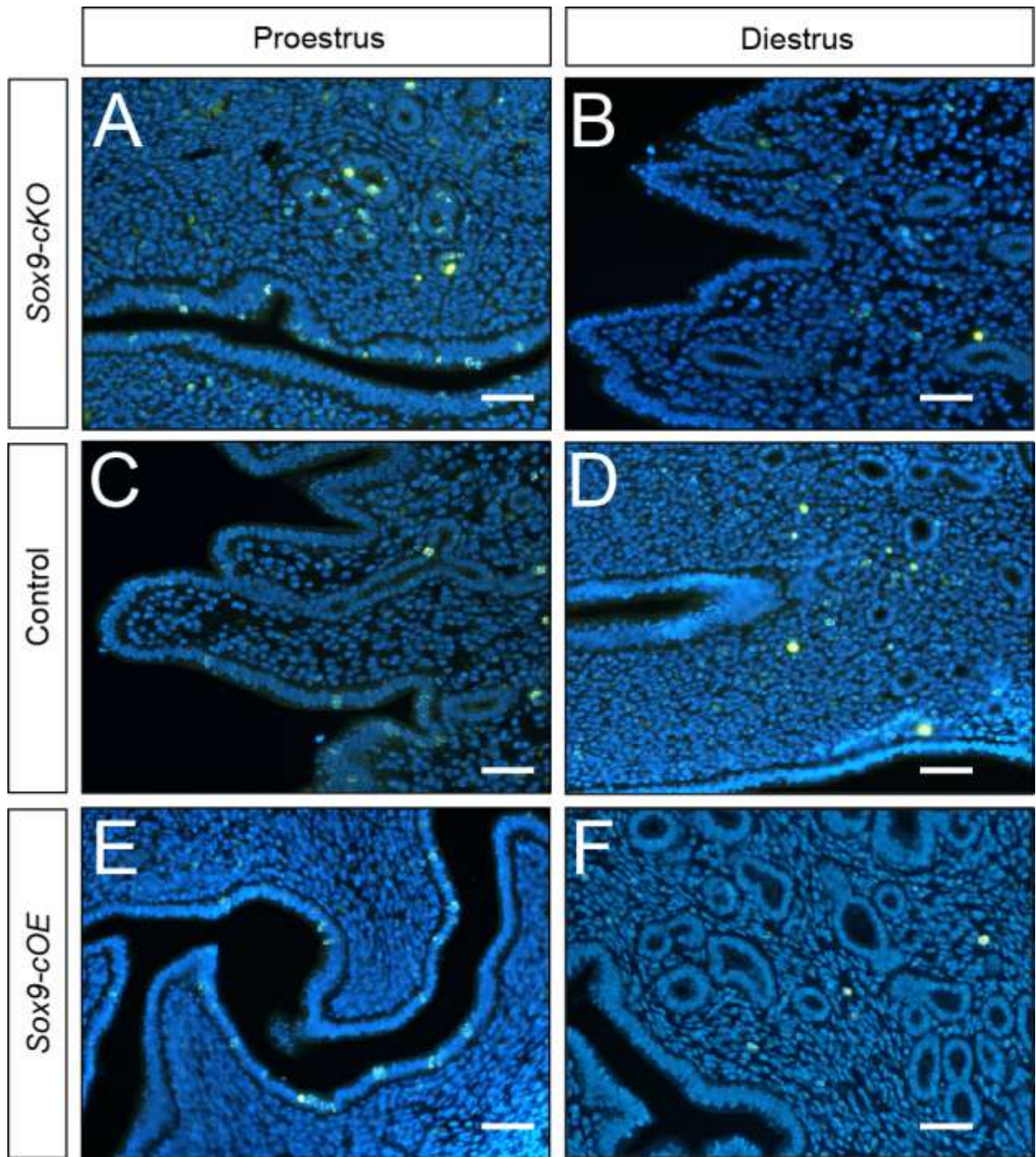
Figure 27: Comparing apoptotic levels in adult uteri during metestrus. (A, B, D, E, G, H) TUNEL assay performed on tissue sections derived from *Sox9-cKO*, control and *Sox9-cOE* females sacrificed during metestrus. No major differences in cell death were detected after performing TUNEL staining, a marker of DNA fragmentation, between *Sox9-cKO*, control and *Sox9-cOE*. (C, F, I) Showing uterine sections stained using H&E. (C) Displaying cell morphology to point out the large number of vacuoles observed in the LE of *Sox9-cKO* females compared to both control (F) and *Sox9-cOE* (I). Arrowheads show a potential loss of epithelial integrity following *Sox9* inactivation. TUNEL staining, green; DAPI, blue. Scale bar 50 μm.

	Tunel Low Mag	Tunel High Mag	H&E High Mag
Sox9-cKO	A	B	C
Control	D	E	F
Sox9-cOE	G	H	I
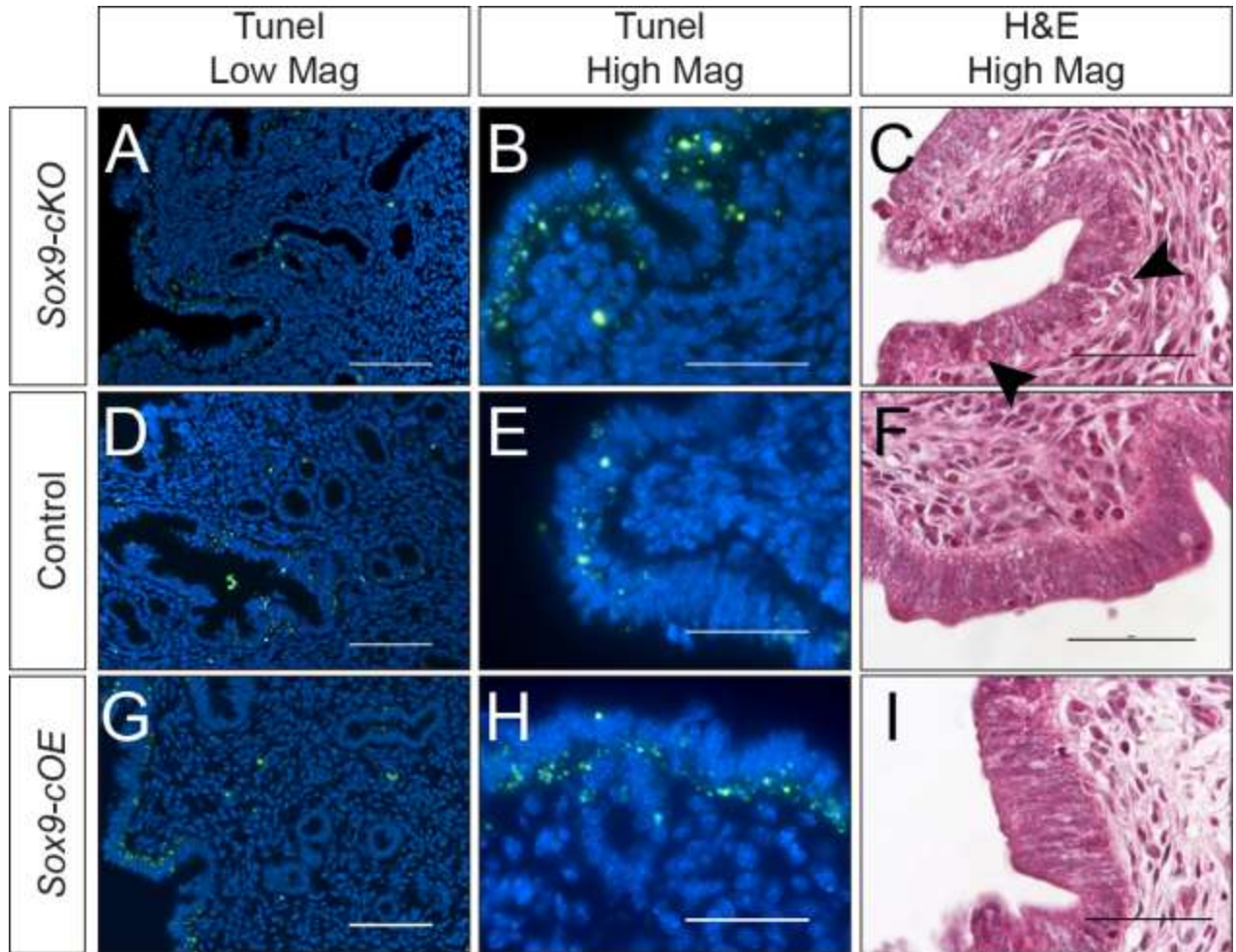
In tissue sections stained by H&E, we observed many vacuoles in the basement membrane and inside the epithelial layer and in the uterine cavity (Figure 27C, F, I). It appears that the fragmented DNA is transported inside vacuoles from the basement membrane into the uterine lumen. The LE of *Sox9-cKO* contained more of these vacuoles than the LE from both control and *Sox9-cOE* mice (Figure 27C).

While trying to explain why there appears to be more vacuoles in the *Sox9-cKO* uterine epithelium, we noticed a potential difference in the thickness of the epithelium. We measured the height of the columnar epithelium in multiple tissue sections and at different time-points (Figure 28). At P21 and P28 the height of the LE is comparable in *Sox9-cKO* to control, and *Sox9-cOE*, indicating that inactivating and overexpressing *Sox9* does not affect the thickness of the epithelium in non-cycling prepubescent females. At P35, when the females begin to cycle, there is statistical difference (p= 0.000307) in the height of the LE between *Sox9-cKO* and control. No difference (p= 0.643484) was detected between control and *Sox9-cOE*. The LE in both control and *Sox9-cOE* is thicker than the LE in *Sox9-cKO* uteri. This observation suggests that Sox9 regulates aspects of the molecular mechanism that promotes the thickening of the LE.

Interestingly, while in adult control females the LE is statistically thicker during estrus when compared to diestrus (p=0.00175) (Figure 29), in both *Sox9-cKO* and *Sox9-cOE*, there is no statistical difference in the height of the LE when comparing diestrus and estrus (p=0.33 and p=0.065, respectively).

Figure 28: Morphometrical measurement of the LE from prepubescent females. Morphometrical measurements of the height of the LE at various time-points. No significant difference between measurements made of the thickness of the epithelium between *Sox9-COE* and control at P21, P28, and P35. No significant difference in the thickness of the LE was detected between *Sox9-cKO* and control females at P21 (p= 0.139367) and P28 (p= 0.867993). A significant difference (p= 0.000307) was observed at P35.

.
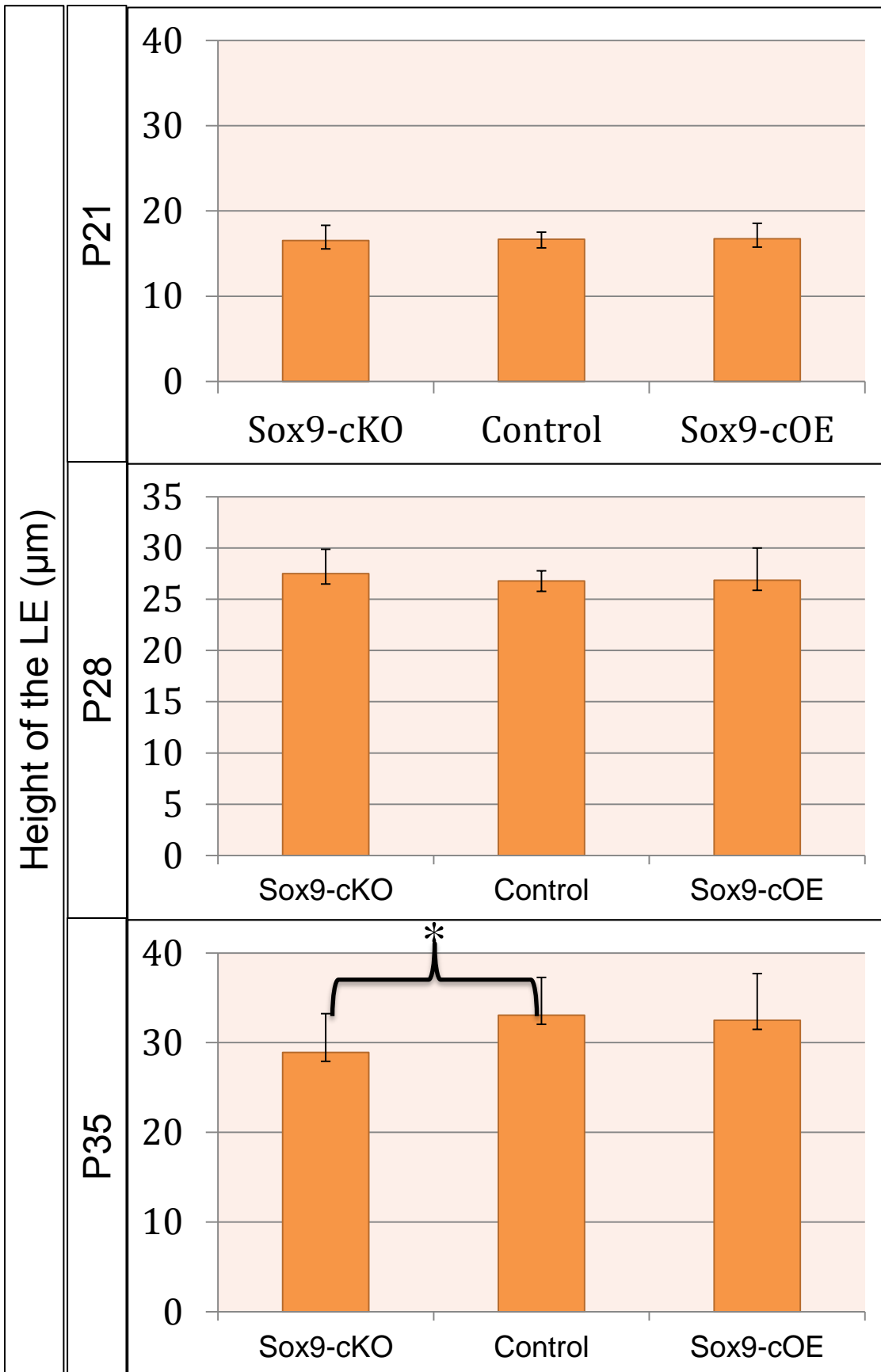
Figure 29: Morphometrical measurements of the LE from adult cycling females. Height of the LE during diestrus and estrus of stage-matched *Sox9-cKO*, control, and *Sox9-cOE*. In control females, the LE is significantly thicker during estrus (p= 0.001753). No significant changes between estrus and diestrus were measured in either *Sox9-cKO* (p= 0.330779) or *Sox9-cOE* (p= *0.065496).* The height of the LE is statistically shorter in *Sox9-cKO* (p= 1.13762E-10) and taller in *Sox9-cOE* (p= 1.87535E-16) when compared to stage-matched controls.
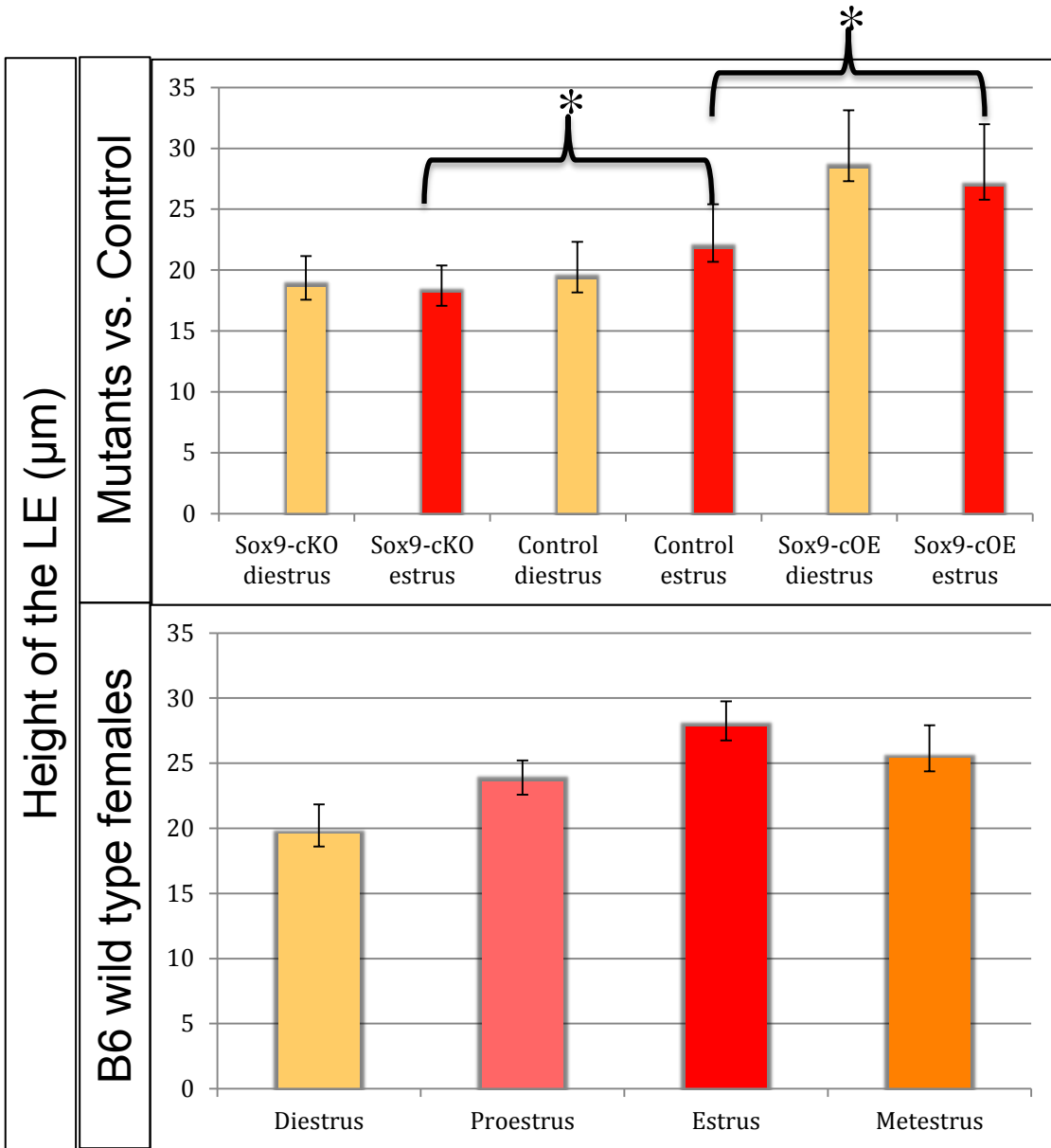
Moreover, the LE is thicker in *Sox9-cOE* when compared to control females in both diestrus and estrus (Figure 29). The thickness of the luminal epithelium in *Sox9-cKO* uteri remains at the "base level" (comparable to that of the control during diestrus) throughout the entire estrous cycle. This indicates that in adult females SOX9 plays a role in allowing the LE to thicken upon the influence of hormones. Additionally, since we initially did not observe any significant difference between control and *Sox9-cOE*, presumably, the changes observed might be generated by the ectopic expression of Sox9 in the stroma and myometrium.

Molecular Markers

UGs become hyperplastic after we overexpressed SOX9. To determine if the GE changes differentiation status, we performed immunofluorescent staining using an α-FOXA2 antibody (Figure 30). FOXA2 is marker for GE; it is present in the deeper part of the UGs, closest to the myometrium. FOXA2 was present in the GE of *Sox9-cKO*, control, and *Sox9-cOE,* suggesting *FoxA2* expression is independent of SOX9. Interestingly, FOXA2 was absent in some areas that display cystically dilated hyperplastic UGs in both 8 month and 1-year-old tissue samples (Figure 30C, D, G, H). These areas of the UG also displayed a loss of SOX9. These observations suggest that FOXA2-expressing GE cells are maintained in the cystically dilated hyperplastic UGs.

Figure 30: Hyperplastic UGs maintain FOXA2 expression, a marker of GE.

(A-H) Immunofluorescent staining using an α-FOXA2 antibody. Showing FOXA2 positive immunofluorescent staining in the GE of 8-month and 1-year-old control and *Sox9-cOE.* (C, D) Cribriform UGs showed decreased levels of FOXA2. (E-H) Showing cystically dilated UGs also displaying a reduction in levels of FOXA2. FOXA2, red; DAPI, blue. Scale bar, 50 μm.
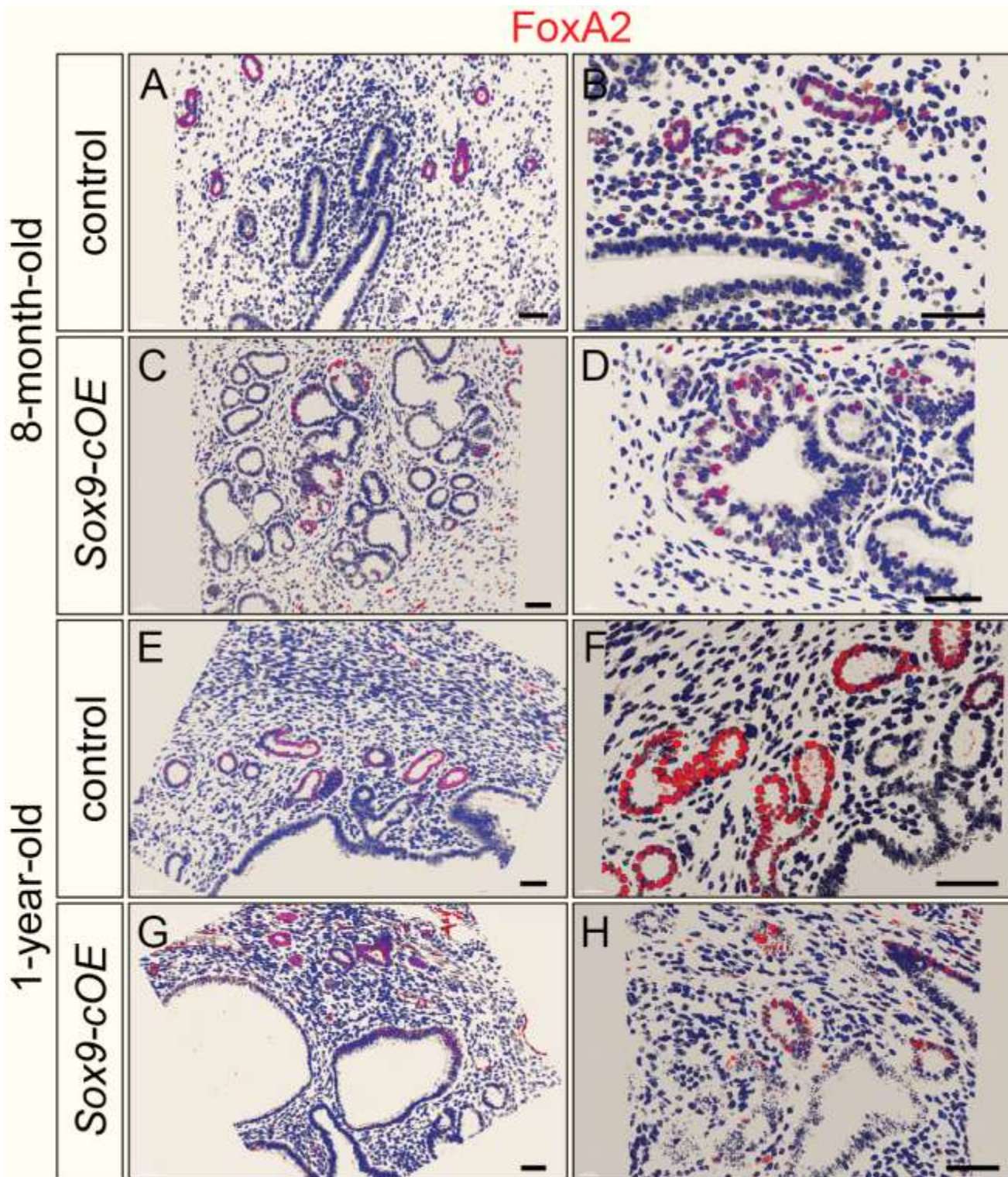
To determine if the integrity of the LE had become compromised, we performed immunofluorescent staining using an α-p63 antibody (Figure 31). This transcription factor is expressed in stratified squamous epithelium but is absent in columnar epithelium. As a control, we co-stained tissue sections that contained parts of the cervix. The cervical epithelium is stratified and as expected, we detected positive staining when stained with α-p63 (Figure 31E, F). We were unable to detect any levels of p63 in the LE or GE in all samples we examined (Figure 31A-F). Even 1-year-old tissue sections that display hyperplasia and metaplasia did not stain positive for p63. This observation suggests that although hyperplastic, the uterine epithelium does not become stratified.

Discussion

Overexpressing *Sox9* Leads to Endometrial Hyperplasia

We devised a genetic strategy to constitutively activate *Sox9* in the FRT. *Sox9* expression was driven by the CAG promoter that can lead to ubiquitous expression[126]. The allele was activated upon Cre-mediated recombination. We used the *Pgr* promoter to drive expression of Cre. *Pgr* is initially expressed mostly in the uterine epithelium. Upon females reaching sexual maturity,

Figure 31: The uterine epithelium does not become stratified. (A-F) Immunofluorescent staining performed in uterine tissues using an α-p63 and α-SOX9 antibodies. P63 marks squamous stratified epithelium. (A-B) Showing 1-year-old tissue sections derived from 1-year-old *Sox9-cKO* (A) and control (B). (C, D) Tissue sections derived from 1-year-old *Sox9-cOE* females showing areas containing cystically dilated UGs. Though hyperplastic, the uterine epithelium does not express p63. (E, F) Tissue sections derived from 1-year-old *Sox9-cOE* females containing areas of the cervical epithelium. The cervical epithelium stained positive for p63. SOX9, green; P63, red. Scale bar, 50 μm.

Sox9 green; P63 red

138
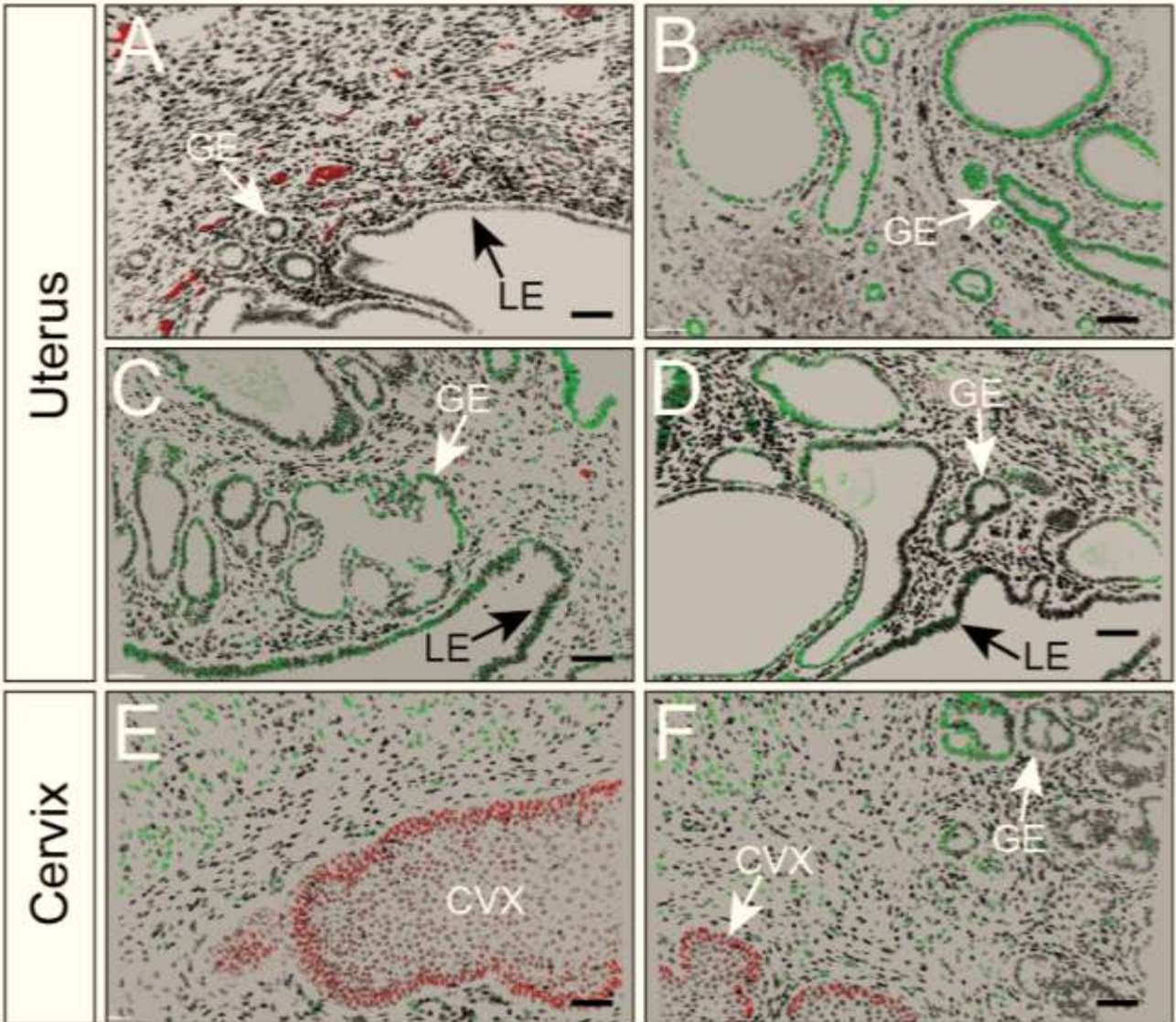
Pgr is expressed in the uterine epithelium, stroma and myometrium[106]. Before puberty, the uteri of *Sox9-cOE* females appeared morphologically normal when compared to control littermates. Therefore, overexpressing *Sox9* in the uterine epithelium does not result in immediate morphological abnormalities. Gross examination of 8-month and 1-year-old *SOX9-cOE* females revealed multiple cystic structures present inside the uterus. These cysts resembled the cystic structures present in human endometrial polyps[27]. Histologically, these structures appeared as cystically dilated uterine glands present in the endometrium surrounded by fibrotic stroma. Another group reported that injecting *N*-ethyl-*N*-nitrosourea (ENU) in mice containing only one functional *p53* allele (*p53* +/-) also development endometrial polyps with a similar histology to what we observed[129]. Endometrial polyps are usually benign, although they can also transform into endometrial cancer[30]. 20-25% of women over the age of 40 will eventually develop endometrial polyps[29].

Histologically, the aged *Sox9-cOE* females included stromal fibrosis, cystically dilated UGs, thick-walled blood vessels and adenomyosis. These cystic dilatations observed in our *Sox9-cOE* mice did not appear to grow inside the uterine cavity as in endometrial polyps. Nonetheless, histological analysis of *Sox9-cOE* uterine sections clearly revealed lesions characteristic of human endometrial polyps.

We have also discovered regions that showed morphology associated with complex hyperplasia; glands that vary in size and contain numerous size buds. The UGs showed a crowded cytoarchitecture, although stroma was

observed between the epithelium, indicating that though hyperplastic, the lesions had not progressed to endometrial adenocarcinomas. Therefore, *Sox9-cOE* females develop cellular changes that are considered hallmarks of disease progression. The cytological abnormalities resembled what is seen in human simple endometrial hyperplasia. Moreover, we detected glands growing in a more cribriform, crowded fashion, similar to what is seen in human complex endometrial hyperplasia[27].

Endometrial polyps are known to develop into endometrioid adenocarcinoma[30]. With this in mind, it seems that the polypoid-like lesions we observed in *Pgr-Cre; SOX9-cOE* may be progressing to a disease state comparable to that found in humans. Further examination of more time points would allow us to study disease initiation and progression. Moreover, breast cancer patients treated with Tamoxifen are at a higher risk of developing endometrial polyps, simplex and complex hyperplasia, adenomyosis, and adenocarcinoma[130-132]. It is essential to understand the aberrant cellular program that leads to atypical endometrial hyperplasia and endometrioid adenocarcinoma. Our new mouse model is an excellent candidate to track the progression of this disease of the FRT.

Greater Epithelial Invagination Results in Hyperplastic Lesions

In an effort to explain the possible cellular mechanism through which glandular hyperplasia manifests, we have introduced a plausible hypothesis:

Sox9 stimulates epithelial invagination and subsequent differentiation of luminal epithelium into glandular epithelium. This could explain the appearance of glandular hyperplasia over a certain period of time (8 weeks to approximately one year). In our mouse model, we have observed that the *Sox9-cOE* uteri appear to contain greater luminal space when compared to control uteri. In contrast, the uteri of *Sox9-cKO* appear to contain less luminal space when compared to control uteri. Perhaps, by being at the center of the β-Catenin-FGF signaling pathway, *Sox9* functions as a regulator of GE cell fate specification. A recent study showed that ectopic expression of both SOX9 and SLUG were sufficient to differentiate mammary luminal epithelium into long-term repopulating stem cells of the mammary glands[133]. Thus, continuous expression of *Sox9* results in glandular hyperplasia, because cells of the LE are specified to become GE. On the other hand, inactivating *Sox9* leads to formation of more LE, which can be observed as greater LE folds inside the uterine lumen. Therefore, one can postulate that the rate of GE to LE increases when *Sox9* is overexpressed and that the rate decreases when it is conditionally inactivated. This mechanism seems to be maintained in balance by an unknown genetic program. As females age and cells accumulate mutations, this genetic program may become unbalanced and lead to hyperplastic lesions.

As the female mouse transitions through the estrous cycle, cells turn on expression of SOX9 in the LE from proestrus until metestrus, when it appears to revert back to basal levels. It happens that SOX9 turns on during the proliferative phase of the estrous cycle, perhaps promoting the formation of new GE at each

new cycle. *Wnt5a* and *Wnt4* have been shown to be upregulated in the stroma in response to hormonal cues[134]. Wnts activate β-CATENIN, which then activate genes that promote proliferation. In the GE, SOX9 potentially negatively regulates β-CATENIN, while positively regulating its own transcription, leading to lower levels of cell proliferation. This correlates with our observations that mitotic figures were devoid of SOX9. We also detected loss of SOX9 in uterine sections displaying hyperplastic lesions. Inactivation of SOX9 could potentially lead to the increased β-CATENIN activity, which results in the hyperplastic lesions observed. Immunohistochemistry analysis of the activated form of β-CATENIN would allow us to determine if this is what is occurring.

Interestingly, even though SOX9 is mainly expressed in the uterine epithelium, we observed morphological differences in the uterine stroma after inactivating *Sox9*, suggesting that SOX9 somehow regulates aspects of the epithelial-mesenchymal crosstalk. Additionally, we also detected morphological changes in the both the uterine epithelium and in the stroma in *Sox9-cOE* uteri, reinforcing the notion that *Sox9* regulates elements of the epithelial-mesenchymal crosstalk. The endometrial hyperplasia observed could potentially stem from faulty communication with the stroma, since stromal fibrosis could be the mediator of the hyperplasia. However, constitutive activation of *Smoothened* also leads to stromal fibrosis, albeit these mice did not develop cystic dilatations[135]. Overexpressing *Sox9* using the *Amhr2-Cre* mouse line, which expresses Cre only in the stroma, would help us determine if SOX9 promotes the

stromal fibrosis, and if this fibrosis leads to the development of cystically dilated uterine glands.

Chapter V: Future Studies

Using OPT imaging, we determined that UGs branch sometime after P11 in the mouse uterus. By imaging FRTs at various time-points between P11 to 8 weeks, we should be able to determine when branching morphogenesis takes place in the mouse uterus. Concomitantly, we will measure estrogen and progesterone levels to determine if the process of branching morphogenesis is affected by hormones. Furthermore, we would like to culture GE using in vitro culturing systems that mimic the 3D matrix found in the uterus in vitro to determine the molecular pathways that affect branching morphogenesis[97].

We correlated the presence of SOX9 with the initial formation of the UGs. Recently, it was demonstrated that *Sox9*-expressing cells in the adult intestinal crypt, pancreatic duct, and bile duct contribute to organ maintenance by renewing various differentiated cell types, including hepatocytes[136]. Lineage-tracing experiments revealed that hepatocytes formed during embryogenesis do not develop from *Sox9*-expressing cells; however, *Sox9*-expressing cells of the bile duct are able to differentiate into hepatocytes later during adulthood. This implies that *Sox9*-expressing epithelial cells give rise to organ progenitor stem cells that contribute to organ maintenance. Furthermore, it was recently demonstrated that transient expression of *Sox9* and *Slug* are sufficient to convert mammary luminal epithelial cells into bipotential mammary gland stem cells[133]. In the human endometrium, it has been hypothesized that epithelial progenitor cells reside in the GE[137]. We detected SOX9 expression in the GE of human

endometrial samples. Therefore, it would be interesting to explore the role of SOX9 in the maintenance of the uterine epithelium. Our initial observations indicated that SOX9-LP cells are present in areas of active regeneration in the post-partum mouse uterus. Perhaps, *Sox9*-expressing cells, sequestered in the UGs, are able to contribute to the maintenance of the uterine epithelium. It was shown that the LE divides more rapidly than the GE, suggesting that the GE contains epithelial progenitor cells that contribute to the re-epithelialization of the endometrium after menses[138].

One hypothesis is that SOX9 induces the formation of a pool of progenitor epithelial cells that reside in the GE. In the GE, these progenitor cells are likely sequestered from potentially hazardous areas (i.e. the uterine cavity) that could be exposed to foreign materials. Inactivating *Sox9* in the lung and in the uterus did not compromise the organ[101]. We observed a similar result after conditionally knocking out *Sox9* in the uterine epithelium. SOX8, SOX9, and SOX10 have known compensatory roles; therefore, future experiments would require knocking out two or possibly all three *SoxE* genes. Alternatively, the lack of an overt phenotype may be because our mice are kept in almost pathogen-free conditions, where they are not exposed to the hazards of the outside world. It is possible that living in clean conditions does not induce lineage-specific progenitor cell activity inside a protected zone. One could explore what would happen if mice were transferred into real world conditions like wild mice.

I would like also to explore the role of overexpressing *Sox9* exclusively in the uterine stroma and compare the phenotype to ours in the epithelium. We

observed multiple hyperplastic lesions in the uteri of *Sox9-cOE* females. Is the hyperplasia a consequence of stromal fibrosis or are these two events separate? This could be achieved by crossing *Sox9-OE* with *Amhr2-Cre* mice, since *Amhr2* is expressed exclusively in the mesenchymal compartment of the mouse uterus.

I would also like to explore the cellular mechanisms that promote the formation of polyps inside the uterine cavity in humans. In mice, even though we observe very similar morphology, we are unable to detect actual polyps inside the uterine cavity. Today, there are other better mouse models that can be used to specifically express Cre in the GE. *Foxa2-rtTA* mice[139] may be used to conditionally overexpress *Sox9* exclusively in the GE. Additionally, I would like to use these mice to turn on expression of a marker in the UGs and let these mice age and have multiple parturitions. My aim would be to investigate if after tissue regeneration, cells that once were part of the GE transdifferentiated into LE. This would support the idea that the GE serves as a lineage-specific epithelial progenitor cell. I would also like to investigate in more detail the mechanism that maintains *Sox9* expression in the GE, especially Fgf signaling originating from the myometrium. There are several mouse lines that can be used to express Cre only in the myometrium to conditionally knockout *Fgf7* and *Fgf10*. *Amhr2-Cre* mice may be used for this purpose.

Additionally, we have generated a great amount of data by using ChIP-Seq for SOX9 binding site, which I would like to compare to an RNA-Seq analysis of the GE. We plan to isolate and sequence all mRNA present in SOX9-

expressing cells. By comparing both data sets, we would get a better understanding of the signaling network controlled by SOX9.

Appendix: Identification of Candidate SOX9 Target Genes by Chromatin Immunoprecipitation Followed by ChIP-Seq

Introduction

SOX9 interacts with DNA through its HMG domain. It binds to the minor groove of the DNA double helix and induces bending of the DNA[82]. SOX9 regulates the expression of its gene targets using an N-terminus transactivation domain[140]. By interacting with p300, a histone acetylase, SOX9 activates gene expression of its target genes[141]. To discover SOX9 target genes, we decided to determine which DNA sequences SOX9 binds to in the mouse genome. Previously, potential SOX9 interactions sites have been uncovered using ChIP-on-chip[142]. We decided to perform ChIP-Seq to discover potential genes regulated by SOX9. We isolated DNA fragments bound to SOX9 in both the uterus and testis isolated from C57BL/6J females and sequenced them using high-throughput sequencing. We obtained millions of short reads from both DNA samples (uterus and testis). Both sets of sequences were independently aligned with the mouse genome (assembly 2007 NCBI37/mm9) using Galaxy[143]. By comparing both data sets, we were able to discover 666 potential SOX9 target genes.

Material and Methods

Chromatin Immunoprecipitation Followed by Next Generation Sequencing (ChIP-Seq)

Approximately 30 adult (6-8 week old) uteri from females and ~20 pairs of testes from postnatal day 5-7 males were isolated from strain C57BL/6J. The organs were removed promptly and placed in cold PBS. Organs were weighed, placed in a petri dish, and minced into fine pieces with a razor blade. 5 ml cold PBS was added to each dish to resuspend the minced tissue and transferred to a 15 ml conical tube. An additional 5 ml of cold PBS was added to the dish to collect the residual tissues and the suspension was transferred into the same tube to pool the material (total 10 ml of tissue suspension in PBS). 278 μl of 37% formaldehyde (Sigma, cat# F8775) was added to the 10 ml tissue suspension and rotated at RT for 10 minutes to crosslink the protein to the DNA. To stop the crosslinking reaction, we added (1/3 volume) 3.4 ml of 0.5 M glycine (final concentration 0.125 M) into the 15 ml conical tube, and then rotated at RT for 5 minutes. The tubes were centrifuged at 1000 g for 5 minutes at 4°C. The supernatant was decanted and the pellet was washed twice with cold PBS, and then centrifuged at 1000 g for 5 minutes at 4°C. The supernatant was decanted and the cell pellet was resuspended in 5 ml of cold PBS supplemented with protease inhibitor (Roche, Cat# 04693116001) and 1 mM PMSF. The samples were transferred into a 15 ml dounce and dounced 10-20 times using a "loose"

pestle. The dounced samples were transferred into a new 15 ml conical tube and centrifuged at 1000 g for 5 minutes at 4°C. The supernatant was discarded and 5 ml of cell lysis buffer (5 mM PIPES, pH 8.0, 85 mM KCl, 0.5 % NP40) supplemented with PI and 1 mM PMSF was added. The samples were left to swell on ice for 10 minutes and transferred into a clean dounce. The samples were dounced 10-20 times with a "tight" pestle to break the cell membrane and separate the cytoplasmic content from the nuclei. The contents were transferred into a new 15 ml conical tube. The dounce was rinsed with 1 ml chilled lysis buffer with 1 mM PMSF and the residue was pooled into the same 15 ml conical tube. Total sample volume was 6 ml. The total number of nuclei was estimated by sampling 20 μl of the total solution and mixing with 20 μl of 0.4% trypan blue. The number of nuclei present was counted using a hemocytometer. The 15 ml conical tubes were centrifuged at 1000 g for 5 minutes at 4°C to pellet the nuclei. The pelleted nuclei was resuspended in nuclei lysis buffer (1% SDS, 10 mM EDTA, 50 mM Tris-HCl, pH 8.1) supplemented with PIs and PMSF at 1 x 10^6 nuclei per 200 μl. The nuclei suspension was divided into multiple 1.5 ml tubes (200 μl per tube) and 0.1 g of glass beads (212 – 300 micron in diameter, Sigma, cat # G1277) per tube were added. The tubes were sonicated using the Bioruptor (Diagenode) for 10 cycles to achieve chromatin fragment sizes around 500 base pair. The samples were centrifuged at 1000 g for 5 minutes at 4°C to pellet the glass beads. The supernatant was transferred into a new 1.5 ml tube. The tubes were centrifuged at 15000 g for 10 minutes at 4°C to remove cellular debris and residual glass beads. The supernatant was transferred into a new 1.5 ml tube.

The samples that were not used for the next step were stored at -80°C. Prior to the immunoprecipitation step, 250 mg of Protein A-sepharose CL-4B (GE Healthcare, cat # 17¬0780-01, size = 1.5 g) was added to a 15 ml conical tube. 10 ml PBS was added to swell the beads at 4°C for >2 hours. The beads were washed 3 to 4 times by centrifuging the tubes at 1000 g for 5 minutes at 4°C, discarding the supernatant and adding 10 ml of PBS each time. Once the beads were washed, a 2 ml slurry (~50%) of Protein A beads was prepared. For each IP reaction, 50 µl of the Protein A slurry was used with the addition of 1 ml of ChIP dilution buffer (0.01% SDS, 1.1% triton X-100, 1.2 mM EDTA, 16.7 mM Tris-HCl, pH 8.1, and 167 mM NaCl) supplemented with 1 mg/ml BSA and 1 mM PMSF. Each tube was incubated for an hour in ChIP dilution buffer for 1 hour at 4°C. This last step was repeated two times, centrifuging at 500 g for 2 min at 4°C per wash, discarding the supernatant each time. For each IP experiment, 100 µl of the chromatin was diluted with 900 µl of ChIP dilution buffer. The diluted chromatin was added to a tube containing 50 µl of Protein A slurry and rotated for 1 hour at 4°C. The samples were centrifuged at 500 g for 2 minutes. The supernatant was transferred into a new 1.5 ml tube and 5 µg of α-SOX9 antibody was added to each tube. The tubes were left rotating overnight at 4°C.

The next morning, the Chromatin-Antibody suspension was transferred to a tube containing Protein A slurry and rotated for 1 hour at 4°C. The samples were washed by centrifuging the tubes at 200 g for 2 minutes at 4°C. The supernatant was discarded and 1 ml of low salt immune complex wash buffer (0.1% SDS, 1% Triton X-100, 2 mM EDTA, 20 mM Tris-HCl, pH8.1, 150 mM

NaCl) was used to wash the Chromatin-Antibody complex for 5 minutes. The samples were centrifuged as described in the previous step, the supernatant was discarded and the Chromatin-Antibody complex was washed using a high salt immune complex wash buffer (0.1% SDS, 1% Triton X-100, 2 mM EDTA, 20 mM Tris-HCl, pH 8.1, 500 mM NaCl) for 5 minutes. The same washing steps were repeated using lithium chloride immune complex wash buffer (0.25 M LiCl, 1% IGEPAL-CA630, 1% sodium deoxycholate, 1 mM EDTA, 10 mM Tris-HCl, pH 8.1) and two consecutive washing steps using TE buffer (10 mM Tris-HCl, pH 8.1, 1 mM EDTA). 125 μl of freshly prepared ChIP elution buffer (1 M sodium bicarbonate, 10% SDS) was used to elute the Chromatin-Antibody complex from the Protein A beads. The tubes were placed on a nutator for 15 minutes at room temperature. The tubes were centrifuged at 500 g for 2 minutes at room temperature. The supernatant was transferred into a new 1.5 ml tube and an additional 125 μl of ChIP elution buffer was added to the tube containing the beads. The previous steps were repeated and the supernatant was pooled with the initial 125 μl sample recovered. The total volume became 250 μl. A de-crosslinking step was performed on both the experimental sample and the input by incubating the samples overnight in a solution containing 10 μl of 5 M NaCl and 1 μl 10 mg/ml RNase A at 65°C. The next morning, 5 μl of 0.5 M EDTA, 10 μl 1 M Tris-HCl, pH 6.5, and 1 μl of 10 mg/ml Proteinase K was added. The samples were incubated for 2 hours at 45°C. The DNA fragments were isolated using a phenol/chloroform extraction step followed by DNA precipitation. 20 μg of

glycogen was added in the precipitation step to maximize DNA recovery. The DNA pellet was resuspended in 30 μl of sterile water and stored at -20°C.

The DNA fragments were sent to Cincinnati Children's Hospital Medical Center Genetic Variation and Gene Discovery Core Facility and were sequenced using an Illumina HiSeq2000. We obtained millions of short reads from both DNA samples (uterus and testis). Both sets of sequences were processed using Galaxy, an open, web-based platform for biomedical research. Both sets of sequences were processed using Galaxy, an open, web-based platform for biomedical research. We ran the FASTQ Groomer program (version 1.0.4)[144] on both datasets, then mapped using Map with Bowtie for Illumina (version 1.1.2)[145] with the mouse genome (assembly 2007 NCBI37/mm9). We converted the format from SAM to BAM using the SAM-to-BAM program (version 1.1.2)[146]. We used MACS (version 1.0.1)[147] to visualize peaks independently aligned to the mouse genome.

Results

Initially, regions of high sequence repeats (downloaded from USCS genome browser) were subtracted from both the uterus and testis data sets. Repetitive sequences were a concerned because once the program encounters one it can potentially realigned it multiple times in various parts of the reference genome where they are present, potentially creating various fabricated peaks that could obscure the real peaks. Initially, the program discovered 2,872 and

2,597 areas from testis and uteri, respectively, where the sequences seemed to cluster, indicating that these were potential SOX9-DNA binding regions. After depleting the sequences of repetitive-sequences, the program realigned our sequences and discovered 1,921 and 1,742 potential SOX9-DNA binding regions, in samples from testis and uterus, respectively. We intersected both datasets to uncover how many of these regions were present in both samples. The computer program uncovered 666 potential SOX9-DNA binding sites that were present in both tissues. We classified these 666 areas as potential SOX9-DNA binding sites. Areas mapped to the mouse genome are represented by a black bar (Figure 32). Although we did not observe any bars near published SOX9-targets like *Col2a1* and *Amh*, we were able to detect peaks near other important genes. Additionally, as a quality control we examined SOX9-potential binding sites that mapped to Chromosome Y (Figure 32C). From the 1,742 potential SOX9-DNA binding regions obtained from the uterus, only 3 sequences (0.17%) mapped to the Chromosome Y. In contrast, from the 1,921 potential SOX9-DNA binding regions obtained from the testis, 9 sequences (0.47%) mapped to the Chromosome Y.

From the 666 SOX9-binding regions, we obtained a list of 336 potential SOX9-targets (table 1), defined by the University of California, Santa Cruz (UCSC) bioinformatics site using table browser. We pursued one candidate gene that stood out from the rest: Transient receptor potential cation channel, subfamily V, member 4 (TRPV4).

Figure 32: Verification of ChIP-Seq integrity. (A-E) DNA sequences, derived from SOX9-ChIP of uterus and testis, aligned to the mouse reference genome. Showing potential SOX9-binding site (band, user track) present near *Col2a1* (A) and *Amh* (B). (C) Three potential SOX9-binding sites discovered on Chromosome Y. (D) Potential SOX9-binding sites discovered in the intronic region of *Trpv4* (E) and *Cacng2* (F).
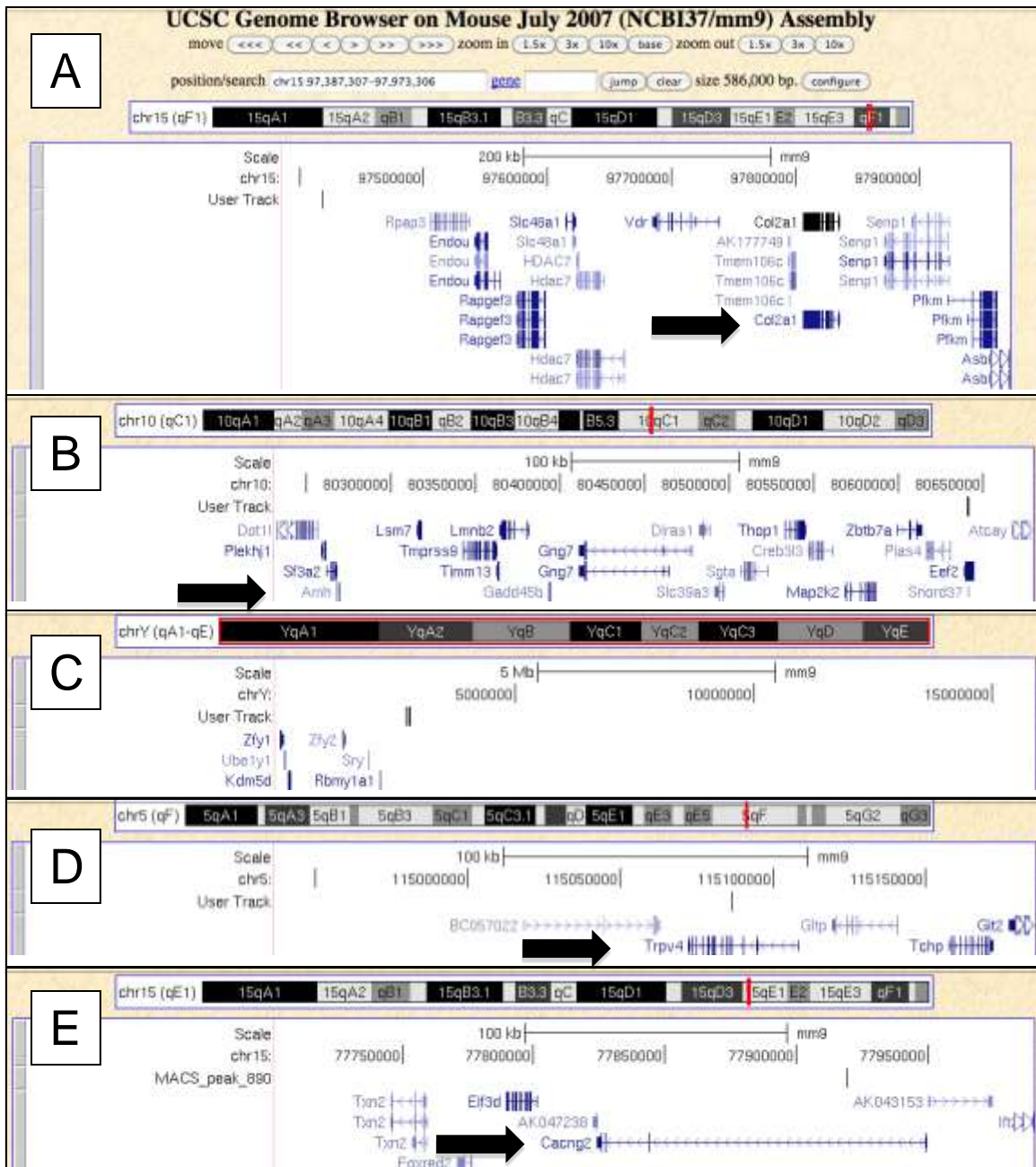
1110007A13Rik	AK086741	Ccdc60	Esr1	Il1rapl1	Mid1	Plxnc1	Sos2	Vwa3b
1500017E21Rik	AK087719	Cd44	Fam184b	Il31ra	mKIAA0933	Polr2f	Spag17	Vwf
2210408I21Rik	AK090337	Cdc42bpb	Fam19a2	Immp2l	mKIAA1164	Poteg	Spata17	Wbscr17
2610528E23Rik	AK138135	Cdh12	Fam46c	Ints4	mlr2	Ppfia2	Ssh1	Wdr76
3110070M22Rik	AK144265	Cdh23	Fam63b	Ipcef1	MOR	Ppm1h	Ssh2	Wdvcf
4921504E06Rik	AK145544	Cdk5rap2	Fbxo28	Itga9	Mphosph8	Ppp1r9a	Ssxb1	Wnt7b
4930468A15Rik	AK146888	Cdk8	Fbxw4	Izumo1	Mrc2	Ppp2r2b	Ssxb9	Wrb
4930525F21Rik	AK148393	Chl1	Filip1l	Jarid2	M-rdgB beta	Prkch	Steap1	X99384
4933404O12Rik	Aldh7a1	Clca2	Flt1	Jph1	Mtrf1	Prkdc	Steap2	Xkrx
5730522E02Rik	Ank1	Clca5	Fnbp1	Kcnh1	Myo7a	Proca1	Sympk	Zc3h7a
9530059O14Rik	Ank2	Cldn10	Foxj2	Kcnq1	Nalcn	Ptprm	Taco1	Zfp106
A130040M12Rik	Ankar	Cntnap3	Frmd4a	Kctd16	Ncam1	Raet1a	Tacr2	Zfp263
A1cf	Ano2	Cntnap5a	Frmd4b	Kctd19	Ncoa1	Raet1c	Taf1b	Zfp791
A630089N07Rik	Apool	Col23a1	Fut8	Kif26b	Nedd4l	Rbm14	Tanc2	Zfp808
Abcb10	Arhgap21	Col4a6	Fxy	Klph	Nell1	Rbm4b	Tbc1d1	Zfp821
Abhd3	Arhgap24	Col6a6	Galntl1	Ksr1	Neurabin	Rgs6	Tcp10a	Zfp949
Abhd6	Arsb	Copz1	Gdap2	Lama1	Nkain3	Rims1	Tcp10c	
abParts	Asrgl1	Csda	glur-1	Lamb3	Nkd1	Rims2	Tcra	
Acacb	Atf2	Csmd1	Gm10905	Large	Noc3l	Rin2	TCR-alpha chain	
Acpl2	Atp7a	Cyp27a1	Gm15800	Lars2	NOX1	Robo1	Tcte2	
Acsl5	Atp7b	D130009I18Rik	Gm16980	Lats2	Nudcd2	Ror2	Timd2	
Acss1	Atrnl1	D430042O09Rik	Gm17002	Lcor	Oprm1	Ros1	Tmc3	
Actr3b	Auts2	D5Ertd579e	Gm525	Lctl	Padi4	Rshl2a	Tmed8	
AK005414	av	Dab2	Gm5544	Lep	Parn	Rsph3a	Tmem164	
AK015347	B230307C23Rik	Dapk1	Gnb1l	Lig1	Pde1c	Rsph3b	Tmem170	
AK016100	B3galnt2	Ddr2	Gphn	Limch1	Pde7b	Rttn	Tmem56	
AK042300	Bard1	Dgki	Greb1	Lin7a	Pdia5	Sbk1	Tmprss15	
AK043285	Bbox1	Dlgap2	Gria1	Lipc	Pdss2	Sbno1	Tmtc1	
AK045681	Bbx	Dnahc14	Grk5	Litaf	Pepd	Sepsecs	Trerf1	
AK047857	BC068229	Dnahc7b	Gsdmc	Lmbrd1	Phactr2	Setbp1	Trhde	
AK050844	beta3GalNAcT2	Dopey2	Gsdmc2	Lmln	Phldb2	Setd4	Trim50	
AK076665	Bhlhb9	Dpf3	Gzmk	Lrp1b	Phrf1	Sfi1	Trpm3	
AK076959	Bpag1	Dpp9	H60b	Lrrc69	Pign	Sh3bgrl2	Trpv4	
AK077481	Bzw2	Dux	Hapln1	Ly86	Pisd-ps2	Sipa1l1	Ttc28	
AK079660	C030034L19Rik	Eef2	Hexb	Magi2	Pitpnc1	Slc14a2	Tusc3	
AK080816	C230081A13Rik	Efna5	Hip1	Mamdc2	Pkn3	Slc39a11	Usp39	
AK081244	C730048C13Rik	Eftud1	Hs6st3	Map2k6	Pknox1	Slc3a1	Vmn2r16	
AK084059	Cadps	EG630579	Hsd11b1	Mcmbp	Plcl2	Slc44a1	Vmn2r59	
AK085253	Camk1d	Epm2a	Htr2c	Mdga2	Plxdc1	Smo	Vmn2r77	
AK086315	Capn8	Erc2	Ifltd1	Mettl3	Plxdc2	Sorcs1	Vps45	

Table 1: Potential SOX9-targets.

Trpv4 is expressed in the epithelia of the kidney, lung, skin, sweat glands and intestines[148-153]. *Sox9* is expressed in the epithelia of all the aforementioned organs and in the testis[154]. Therefore, we decided to determine if knocking out or overexpressing *Sox9* affected the levels of TRPV4. We performed immunohistochemistry using an antibody α-TRPV4.

The levels of TRPV4 were higher in the uterine epithelium of *Sox9-cOE* females (Figure 33J, K, L) when compared to controls (Figure 33E, F, G). Moreover, we also detected ectopic expression of TRPV4 in the uterine stroma in *Sox9* overexpressing mice (Figure 33J, K). We also observed a small reduction in the levels of TRPV4 in the uterine epithelium of *Sox9-cKO* females (Figure 33A, B, C). Thus, there is a positive correlation between TRPV4 levels and SOX9 levels, consistent with the idea that *Trpv4* is a direct transcriptional target of SOX9.

In previous chapters, we showed that SOX9 levels fluctuated in the LE throughout the estrous cycle. Immunohistochemistry analysis indicated that TRPV4 levels remained constant in the uterine epithelium throughout the estrous cycle (Figure 34). Furthermore, it appeared that TRPV4 was localized to the basal membrane domain, primarily in GE. SOX9 is expressed primarily in the GE.

Figure 33: Increased levels of TRPV4 detected in the adult uterine epithelium of *Sox9-cOE* females. Immunohistochemistry performed using α-TRPV4 antibody (red) with nuclei counterstained by hematoxylin (blue). Compared to *Sox9-cKO* (A-D) and control (E-H), tissue sections derived from *Sox9-cOE* (I-L) show augmented levels of TRPV4. Scale bar 50 μm.

	Uteri Low Mag	GE High Mag	LE High Mag	Oviduct Low Mag
Sox9-cKO	A	B	C	D
Control	E	F	G	H
Sox9-cOE	I	J	K	L
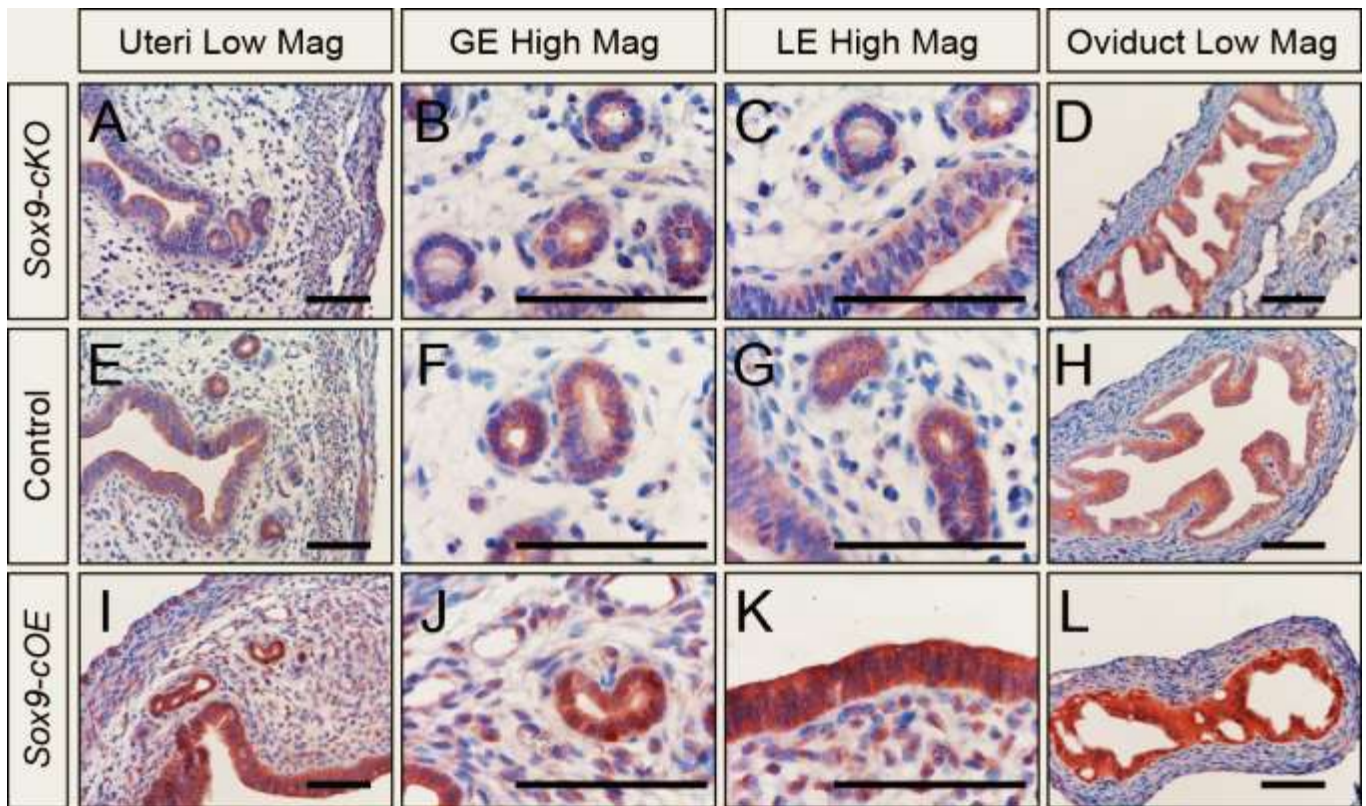
Figure 34: TRPV4 levels are maintained constant through the estrous cycle. Immunohistochemistry analysis performed on uterine sections derived from adult B6 females dissected at different stages of the estrous cycle using α-TRPV4 antibody (red). No counterstain was performed. TRPV4 detected primarily in the basal domain of the uterine epithelium, predominantly in the GE (B, E, H, K). TRPV4 levels remain unchanged though the estrous cycle in B6 females. Scale bar 50 μm.

	Low Mag	GE High Mag	LE High Mag
Proestrus	A	B	C
Estrus	D	E	F
Metestrus	G	H	I
Diestrus	J	K	L
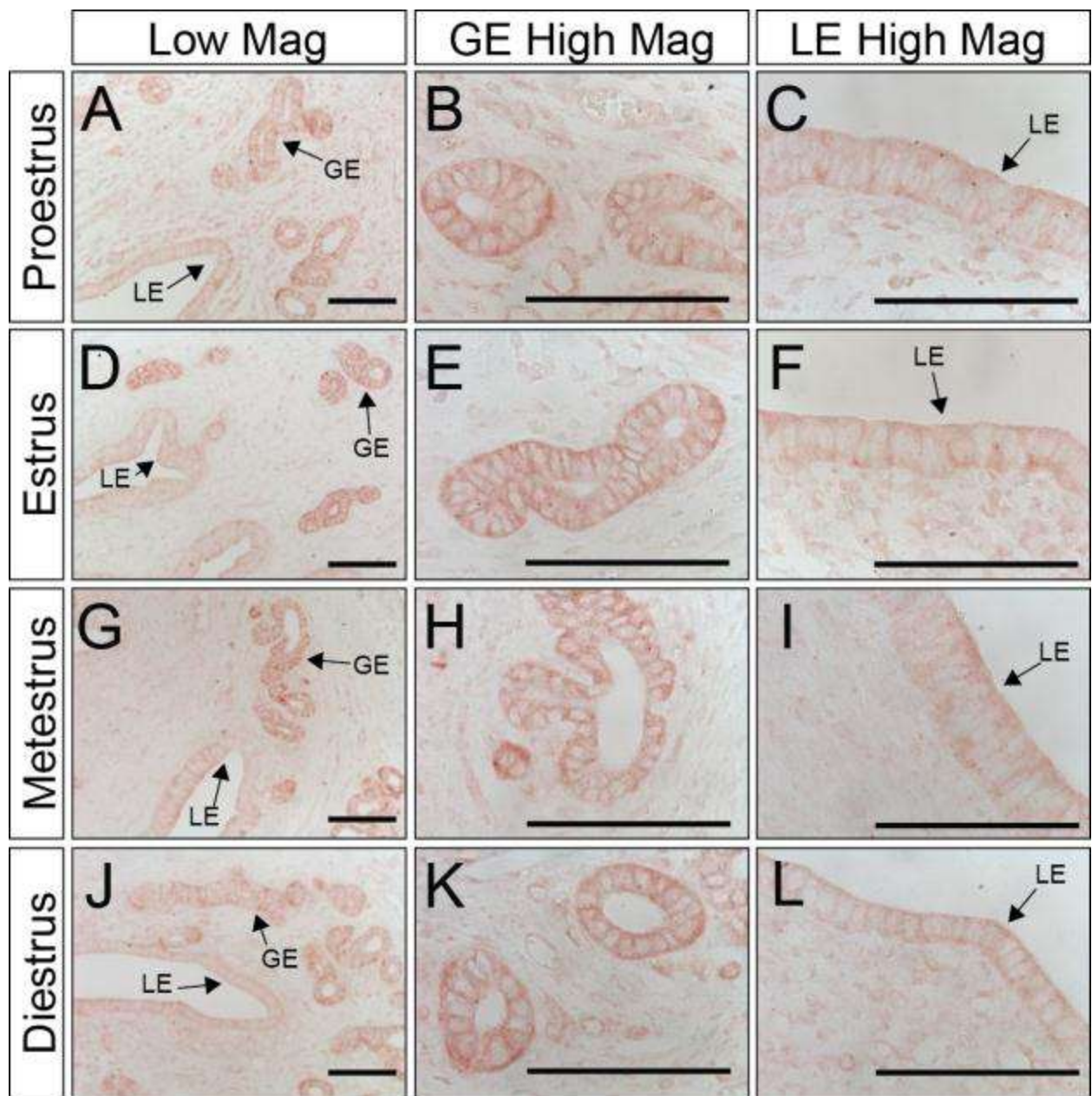
Discussion

We have shown that SOX9 potentially binds and activates expression of *Trpv4*, a voltage-dependent Ca^{2+} channel. In the mouse mammary cell line HC11, activation of TRPV4 promotes intracellular Ca2+ influx and increases paracellular epithelial barrier permeability by lessening lateral tight-junctions[155]. Interestingly, TRPV4 is also expressed in epithelial cells of the kidney, lung, skin, sweat glands and intestines[148-153]. *Sox9* is expressed in all the aforementioned organs, supporting the idea that SOX9 promotes expression of *Trpv4.*

In the HC11 cell line, TRPV4 is localized to the basolateral membrane domain, and activation of this receptor was shown increase paracellular permeability[155]. Furthermore, it was also demonstrated that the increase in paracellular permeability was in part caused by a decrease in the expression of claudins. Claudins play a role in maintaining cell-cell tight junctions. Cadherins are also responsible for establishing cell-cell contacts that control diffusion and confer structural integrity to the epithelium. Cadherins have a five repeat extracellular domain and a conserved cytoplasmic domain. Ca^{2+} is required for binding of the extracellular domains. β-CATENIN along with α-CATENIN bridge the cadherin conserved cytoplasmic domain to the actin cytoskeleton. Maintenance of tight junctions is essential to maintain membrane domains that serve to polarize the cells[44].

Activation of TRPV4 by mechano-stimulation should trigger influx of Ca^{2+}, allowing intracellular ion transport, while disrupting claudin-binding. In the

paracellular space, reduction in levels of Ca^{2+} can potentially decrease adhesion of cadherins. During the estrous cycle, the proliferative phase is followed by massive apoptosis. Tight junctions need to be released during metestrus, when multiple fragmented cells can be detected in the basal lamina prior to being expelled into the uterine cavity. Using immunofluorescent staining against SOX9, we detected greater numbers of SOX9-positive cells starting at proestrus and ending during metestrus. However, we did not detect any changes in the levels of TRPV4 during the estrous cycle.

In the uterus of *Sox9-cOE* mice, we have observed a marked increase in stromal fibrosis. D'Aldebert et, al. showed that activation of TRPV4 led to increased chemokine release and inflammation of the colon. It is possible the stromal fibrosis observed in *Sox9-cOE* mice could be a potential result from increased chemokines[151].

Our data indicates that the LE of *Sox9-cOE* females is statistically taller than both control and *Sox9-cKO*. Therefore, it is plausible that the increase in epithelium height is a consequence of upregulating *Trpv4*. In summary, these studies indicate that SOX9 directly binds the *Trpv4* locus to regulate its transcription. The role of *Trpv4* may be to maintain the integrity of the uterine epithelium.

References

1. Komatsu, M. & Fujita, H. Electron-microscopic studies on the development and aging of the oviduct epithelium of mice. *Anatomy And Embryology* **152**, 243-59 (1978).

2. Humphrey, K.W. Observations on transport of ova in the oviduct of the mouse. *The Journal Of Endocrinology* **40**, 267-73 (1968).

3. Miller, J.G. & Schultz, G.A. Amino acid content of preimplantation rabbit embryos and fluids of the reproductive tract. *Biology Of Reproduction* **36**, 125-9 (1987).

4. Bazer, F.W. Uterine protein secretions: Relationship to development of the conceptus. *Journal Of Animal Science* **41**, 1376-82 (1975).

5. Orvis, G.D. & Behringer, R.R. Cellular mechanisms of Mullerian duct formation in the mouse. *Developmental Biology* **306**, 493-504 (2007).

6. Josso, N., Picard, J.Y. & Trah, D. The antimullerian hormone. *Recent Prog Horm Res* **33**, 117-67 (1976).

7. Kobayashi, A. & Behringer, R.R. Developmental genetics of the female reproductive tract in mammals. *Nature Reviews. Genetics* **4**, 969-80 (2003).

8. Yamanouchi, H., Umezu, T. & Tomooka, Y. Reconstruction of oviduct and demonstration of epithelial fate determination in mice. *Biology of Reproduction* **82**, 528-33 (2010).

9. Kurita, T., Cooke, P.S. & Cunha, G.R. Epithelial-stromal tissue interaction in paramesonephric (Mullerian) epithelial differentiation. *Developmental Biology* **240**, 194-211 (2001).

10. Matthews, C.J., Thomas, E.J., Redfern, C.P. & Hirst, B.H. Ion transport by human endometrial epithelia in vitro. *Human Reproduction* **8**, 1570-5 (1993).

11. Hay, W.W., Jr. Placental transport of nutrients to the fetus. *Hormone Research* **42**, 215-22 (1994).

12. Knipp, G.T., Audus, K.L. & Soares, M.J. Nutrient transport across the placenta. *Advanced Drug Delivery Reviews* **38**, 41-58 (1999).

13. Shynlova, O., Tsui, P., Jaffer, S. & Lye, S.J. Integration of endocrine and mechanical signals in the regulation of myometrial functions during pregnancy and labour. *European Journal Of Obstetrics, Gynecology, And Reproductive Biology* **144 Suppl 1**, S2-10 (2009).

14. Lee, K.Y., Jeong, J.W., Tsai, S.Y., Lydon, J.P. & DeMayo, F.J. Mouse models of implantation. *Trends In Endocrinology And Metabolism: TEM* **18**, 234-9 (2007).

15. Paria, B.C., Huet-Hudson, Y.M. & Dey, S.K. Blastocyst's state of activity determines the "window" of implantation in the receptive mouse uterus. *Proceedings Of The National Academy Of Sciences Of The United States Of America* **90**, 10159-62 (1993).

16. Sato T, Fukazawa Y, Kojima H, Enari M, Iguchi T & Ohta Y. Apoptotic cell death during the estrous cycle in the rat uterus and vagina. *The Anatomical Record* **248**, 76-83 (1997).

17. Zhang, Q. & Paria, B.C. Importance of uterine cell death, renewal, and their hormonal regulation in hamsters that show progesterone-dependent implantation. *Endocrinology* **147**, 2215-27 (2006).

18. Wood, G.A., Fata, J.E., Watson, K.L. & Khokha, R. Circulating hormones and estrous stage predict cellular and stromal remodeling in murine uterus. *Reproduction* **133**, 1035-44 (2007).

19. Martin, R.D. The evolution of human reproduction: a primatological perspective. *American Journal Of Physical Anthropology* **Suppl 45**, 59-84 (2007).

20. Crichton, E. *Reproductive Biology Of Bats*, (Academic Press, 2000).

21. Fuxe, K. & Nilsson, O. The mouse uterine surface epithelium during the estrous cycle. *The Anatomical Record* **145**, 541-8 (1963).

22. Hoover, R.N., Hyer, M., Pfeiffer, R.M., Adam, E., Bond, B., Cheville, A. L., Colton, T., Hartge, P., Hatch, E.E., Herbst, A.L., Karlan, B.Y., Kaufman, R., Noller, K.L., Palmer, J.R., Robboy, S.J., Saal, R.C., Strohsnitter, W., Titus-Ernstoff, L. & Troisi, R. Adverse health outcomes in women exposed in utero to diethylstilbestrol. *The New England Journal Of Medicine* **365**, 1304-14 (2011).

23. Stewart, C.A., Fisher, S.J., Wang, Y., Stewart, M.D., Hewitt, S.C., Rodriguez, K. F., Korach, K. S. & Behringer, R. R. Uterine gland formation in mice is a continuous process, requiring the ovary after puberty, but not after parturition. *Biology Of Reproduction* **85**, 954-64 (2011).

24. Persson, I., Adami, H.O., Bergkvist, L., Lindgren, A., Pettersson, B., Hoover, R. & Schairer, C. Risk of endometrial cancer after treatment with oestrogens alone or in conjunction with progestogens: results of a prospective study. *BMJ* **298**, 147-51 (1989).

25. Sherman, M.E. Theories of endometrial carcinogenesis: a multidisciplinary approach. *Modern Pathology: An Official Journal Of The United States And Canadian Academy Of Pathology, Inc* **13**, 295-308 (2000).

26. Siegel, R., Naishadham, D. & Jemal, A. Cancer statistics, 2012. *CA: A Cancer Journal For Clinicians* **62**, 10-29 (2012).

27. Silverberg, S.G. Problems in the differential diagnosis of endometrial hyperplasia and carcinoma. *Modern Pathology: An Official Journal Of The United States And Canadian Academy Of Pathology, Inc* **13**, 309-27 (2000).

28. Anastasiadis, P.G., Koutlaki, N.G., Skaphida, P.G., Galazios, G.C., Tsikouras, P.N. & Liberis, V.A. Endometrial polyps: prevalence, detection, and malignant potential in women with abnormal uterine bleeding. *European Journal Of Gynaecological Oncology* **21**, 180-3 (2000).

29. Humphrey, P.D., L; Pfeifer, J. *The Washington Manual Of Surgical Pathology*, (Lippincott Williams & Wilkins, 2008).

30. Savelli, L., De Iaco, P., Santini, D., Rosati, F., Ghi, T., Pignotti, E. & Bovicelli, L. Histopathologic features and risk factors for benignity, hyperplasia, and cancer in endometrial polyps. *American Journal Of Obstetrics And Gynecology* **188**, 927-31 (2003).

31. Tjarks, M. & Van Voorhis, B.J. Treatment of endometrial polyps. *Obstetrics And Gynecology* **96**, 886-9 (2000).

32. Deligdisch, L. Hormonal pathology of the endometrium. *Modern Pathology : An Official Journal Of The United States And Canadian Academy Of Pathology, Inc* **13**, 285-94 (2000).

33. Spencer, T.E. & Gray, C.A. Sheep uterine gland knockout (UGKO) model. *Methods In Molecular Medicine* **121**, 85-94 (2006).

34. Burton, G.J., Watson, A.L., Hempstock, J., Skepper, J.N. & Jauniaux, E. Uterine glands provide histiotrophic nutrition for the human fetus during the first trimester of pregnancy. *The Journal Of Clinical Endocrinology And Metabolism* **87**, 2954-9 (2002).

35. Gray, C. A., Bartol, F. F., Tarleton, B. J., Wiley, A. A., Johnson, G. A., Bazer, F. W. & Spencer, T. E. Developmental biology of uterine glands. *Biol Reprod* **65**, 1311-23 (2001).

36. Stewart C.L., Kaspar P., Brunet L.J., Bhatt H., Gadi I., Köntgen F. & Abbondanzo S.J*.* Blastocyst implantation depends on maternal expression of leukaemia inhibitory factor. *Nature* **359**, 76-9 (1992).

37. Zhu, L.J., Bagchi, M.K. & Bagchi, I.C. Attenuation of calcitonin gene expression in pregnant rat uterus leads to a block in embryonic implantation. *Endocrinology* **139**, 330-9 (1998).

38. Hu, J., Gray, C.A. & Spencer, T.E. Gene expression profiling of neonatal mouse uterine development. *Biol Reprod* **70**, 1870-6 (2004).

39. Gray, C. A., Bartol, F. F., Tarleton, B. J., Wiley, A. A., Johnson, G. A., Bazer, F. W. & Spencer, T. E. Developmental biology of uterine glands. *Biology Of Reproduction* **65**, 1311-23 (2001).

40. Kurita, T., Cooke, P.S. & Cunha, G.R. Epithelial-stromal tissue interaction in paramesonephric (Mullerian) epithelial differentiation. *Dev Biol* **240**, 194-211 (2001).

41. Cunha, G.R. Stromal induction and specification of morphogenesis and cytodifferentiation of the epithelia of the Mullerian ducts and urogenital sinus during development of the uterus and vagina in mice. *The Journal Of Experimental Zoology* **196**, 361-70 (1976).

42. Baer, M.M., Chanut-Delalande, H. & Affolter, M. Cellular and molecular mechanisms underlying the formation of biological tubes. *Current Topics In Developmental Biology* **89**, 137-62 (2009).

43. Hogan, B.L. & Kolodziej, P.A. Organogenesis: molecular mechanisms of tubulogenesis. *Nature Reviews. Genetics* **3**, 513-23 (2002).

44. Nelson, W.J. Epithelial cell polarity from the outside looking in. *News in Physiological Sciences: An International Journal Of Physiology Produced Jointly By The International Union Of Physiological Sciences And The American Physiological Society* **18**, 143-6 (2003).

45. Myat, M.M. & Andrew, D.J. Fork head prevents apoptosis and promotes cell shape change during formation of the Drosophila salivary glands. *Development* **127**, 4217-26 (2000).

46. Sawyer J.M., Harrell J.R., Shemer G., Sullivan-Brown J., Roh-Johnson M. & Goldstein B. Apical constriction: a cell shape change that can drive morphogenesis. *Developmental Biology* **341**, 5-19 (2010).

47. Jeong J.W., Kwak I., Lee K.Y., Kim T.H., Large M.J., Stewart C.L., Kaestner K.H., Lydon J.P. & DeMayo F.J. Foxa2 is essential for mouse endometrial gland development and fertility. *Biology Of Reproduction* **83**, 396-403 (2010).

48. Affolter, M., Zeller, R. & Caussinus, E. Tissue remodelling through branching morphogenesis. *Nature Reviews. Molecular Cell Biology* **10**, 831-42 (2009).

49. Wimsatt, W.A. New histological observations on the placenta of the sheep. *The American Journal Of Anatomy* **87**, 391-457 (1950).

50. Perry, J.S. & Crombie, P.R. Ultrastructure of the uterine glands of the pig. *Journal Of Anatomy* **134**, 339-50 (1982).

51. Lu, P., Ewald, A.J., Martin, G.R. & Werb, Z. Genetic mosaic analysis reveals FGF receptor 2 function in terminal end buds during mammary gland branching morphogenesis. *Developmental Biology* **321**, 77-87 (2008).

52. Majumdar, A., Vainio, S., Kispert, A., McMahon, J. & McMahon, A.P. Wnt11 and Ret/Gdnf pathways cooperate in regulating ureteric branching during metanephric kidney development. *Development* **130**, 3175-85 (2003).

53. Robinson, G.W., Hennighausen, L. & Johnson, P.F. Side-branching in the mammary gland: the progesterone-Wnt connection. *Genes & Development* **14**, 889-94 (2000).

54. Steinberg Z., Myers C., Heim V.M., Lathrop C.A., Rebustini I.T., Stewart J.S., Larsen M. & Hoffman M.P. FGFR2b signaling regulates ex vivo submandibular gland epithelial cell proliferation and branching morphogenesis. *Development* **132**, 1223-34 (2005).

55. Miller, C., Pavlova, A. & Sassoon, D.A. Differential expression patterns of Wnt genes in the murine female reproductive tract during development and the estrous cycle. *Mech Dev* **76**, 91-9 (1998).

56. Gordon, M.D. & Nusse, R. Wnt signaling: multiple pathways, multiple receptors, and multiple transcription factors. *The Journal Of Biological Chemistry* **281**, 22429-33 (2006).

57. Yost C., Torres M., Miller J.R., Huang E., Kimelman D. & Moon R.T. The axis-inducing activity, stability, and subcellular distribution of beta-catenin is regulated in Xenopus embryos by glycogen synthase kinase 3. *Genes & Development* **10**, 1443-54 (1996).

58. Vainio, S., Heikkila, M., Kispert, A., Chin, N. & McMahon, A.P. Female development in mammals is regulated by Wnt-4 signalling. *Nature* **397**, 405-9 (1999).

59. Stark, K., Vainio, S., Vassileva, G. & McMahon, A.P. Epithelial transformation of metanephric mesenchyme in the developing kidney regulated by Wnt-4. *Nature* **372**, 679-83 (1994).

60. Mericskay, M., Kitajewski, J. & Sassoon, D. Wnt5a is required for proper epithelial-mesenchymal interactions in the uterus. *Development* **131**, 2061-72 (2004).

61. Miller, C. & Sassoon, D.A. Wnt-7a maintains appropriate uterine patterning during the development of the mouse female reproductive tract. *Development* **125**, 3201-11 (1998).

62. Taylor, K.M., Chen, C., Gray, C.A., Bazer, F.W. & Spencer, T.E. Expression of messenger ribonucleic acids for fibroblast growth factors 7 and 10, hepatocyte growth factor, and insulin-like growth factors and their receptors in the neonatal ovine uterus. *Biology Of Reproduction* **64**, 1236-46 (2001).

63. Klint, P. & Claesson-Welsh, L. Signal transduction by fibroblast growth factor receptors. *Front Biosci* **4**, D165-77 (1999).

64. Pollock P.M., Gartside M.G., Dejeza L.C., Powell M.A., Mallon M.A., Davies H., Mohammadi M., Futreal P.A., Stratton M.R., Trent J.M. & Goodfellow P.J. Frequent activating FGFR2 mutations in endometrial carcinomas parallel germline mutations associated with craniosynostosis and skeletal dysplasia syndromes. *Oncogene* **26**, 7158-62 (2007).

65. Chen, C., Spencer, T.E. & Bazer, F.W. Fibroblast growth factor-10: a stromal mediator of epithelial function in the ovine uterus. *Biology Of Reproduction* **63**, 959-66 (2000).

66. Cardoso, W.V. & Lu, J. Regulation of early lung morphogenesis: questions, facts and controversies. *Development* **133**, 1611-24 (2006).

67. Warburton D., Bellusci S., De Langhe S., Del Moral P.M., Fleury V., Mailleux A., Tefft D., Unbekandt M., Wang K. & Shi W. Molecular mechanisms of early lung specification and branching morphogenesis. *Pediatric Research* **57**, 26R-37R (2005).

68. Topol, L., Chen, W., Song, H., Day, T.F. & Yang, Y. Sox9 inhibits Wnt signaling by promoting beta-catenin phosphorylation in the nucleus. *The Journal Of Biological Chemistry* **284**, 3323-33 (2009).

69. Bernard P., Ryan J., Sim H., Czech D.P., Sinclair A.H., Koopman P. & Harley V.R. Wnt Signaling in Ovarian Development Inhibits Sf1 Activation of Sox9 via the Tesco Enhancer. *Endocrinology* (2011).

70. Blache P., van de Wetering M., Duluc I., Domon C., Berta P., Freund J.N., Clevers H. & Jay P. SOX9 is an intestine crypt transcription factor, is regulated by the Wnt pathway, and represses the CDX2 and MUC2 genes. *The Journal Of Cell Biology* **166**, 37-47 (2004).

71. Murakami, S., Kan, M., McKeehan, W.L. & de Crombrugghe, B. Up-regulation of the chondrogenic Sox9 gene by fibroblast growth factors is mediated by the mitogen-activated protein kinase pathway. *Proceedings Of The National Academy Of Sciences Of The United States Of America* **97**, 1113-8 (2000).

72. Kim Y., Kobayashi A., Sekido R., DiNapoli L., Brennan J., Chaboissier M.C., Poulat F., Behringer R.R., Lovell-Badge R. & Capel B. Fgf9 and Wnt4 act as antagonistic signals to regulate mammalian sex determination. *PLoS Biology* **4**, e187 (2006).

73. Ling S., Chang X., Schultz L., Lee T.K., Chaux A., Marchionni L., Netto G.J., Sidransky D. & Berman D.M. An EGFR-ERK-SOX9 signaling cascade links urothelial development and regeneration to cancer. *Cancer Research* **71**, 3812-21 (2011).

74. Kiefer, J.C. Back to basics: Sox genes. *Developmental Dynamics : An Official Publication Of The American Association Of Anatomists* **236**, 2356-66 (2007).

75. McCauley, D.W. & Bronner-Fraser, M. Importance of SoxE in neural crest development and the evolution of the pharynx. *Nature* **441**, 750-2 (2006).

76. Akiyama H., Chaboissier M.C., Behringer R.R., Rowitch D.H., Schedl A., Epstein J.A. & de Crombrugghe B. Essential role of Sox9 in the pathway that controls formation of cardiac valves and septa. *Proceedings Of The National Academy Of Sciences Of The United States Of America* **101**, 6502-7 (2004).

77. Britsch S., Goerich D.E., Riethmacher D., Peirano R.I., Rossner M., Nave K.A., Birchmeier C. & Wegner M. The transcription factor Sox10 is a key regulator of peripheral glial development. *Genes & Development* **15**, 66-78 (2001).

78. Sock, E., Schmidt, K., Hermanns-Borgmeyer, I., Bosl, M.R. & Wegner, M. Idiopathic weight reduction in mice deficient in the high-mobility-group transcription factor Sox8. *Molecular And Cellular Biology* **21**, 6951-9 (2001).

79. Lioubinski, O., Muller, M., Wegner, M. & Sander, M. Expression of Sox transcription factors in the developing mouse pancreas. *Developmental Dynamics: An Official Publication Of The American Association Of Anatomists* **227**, 402-8 (2003).

80. Foster J.W., Dominguez-Steglich M.A., Guioli S., Kwok C., Weller P.A., Stevanović M., Weissenbach J., Mansour S., Young I.D., Goodfellow P.N., Brook J.D. & Schafer A.J. Campomelic dysplasia and autosomal sex

reversal caused by mutations in an SRY-related gene. *Nature* **372**, 525-30 (1994).

81. Lefebvre, V. & de Crombrugghe, B. Toward understanding SOX9 function in chondrocyte differentiation. *Matrix Biology: Journal Of The International Society For Matrix Biology* **16**, 529-40 (1998).

82. Lefebvre, V., Huang, W., Harley, V.R., Goodfellow, P.N. & de Crombrugghe, B. SOX9 is a potent activator of the chondrocyte-specific enhancer of the pro alpha1(II) collagen gene. *Molecular And Cellular Biology* **17**, 2336-46 (1997).

83. Bridgewater, L.C., Lefebvre, V. & de Crombrugghe, B. Chondrocyte-specific enhancer elements in the Col11a2 gene resemble the Col2a1 tissue-specific enhancer. *The Journal Of Biological Chemistry* **273**, 14998-5006 (1998).

84. Zhang, P., Jimenez, S.A. & Stokes, D.G. Regulation of human COL9A1 gene expression. Activation of the proximal promoter region by SOX9. *The Journal Of Biological Chemistry* **278**, 117-23 (2003).

85. Sekiya I., Tsuji K., Koopman P., Watanabe H., Yamada Y., Shinomiya K., Nifuji A. & Noda M. SOX9 enhances aggrecan gene promoter/enhancer activity and is up-regulated by retinoic acid in a cartilage-derived cell line, TC6. *The Journal Of Biological Chemistry* **275**, 10738-44 (2000).

86. Kou, I. & Ikegawa, S. SOX9-dependent and -independent transcriptional regulation of human cartilage link protein. *The Journal Of Biological Chemistry* **279**, 50942-8 (2004).

87. Kobayashi, A., Chang, H., Chaboissier, M.C., Schedl, A. & Behringer, R.R. Sox9 in testis determination. *Annals Of The New York Academy Of Sciences* **1061**, 9-17 (2005).

88. Hondo E., Phichitrasilp T., Kokubu K., Kusakabe K., Nakamuta N., Oniki H. & Kiso Y. Distribution patterns of uterine glands and embryo spacing in the mouse. *Anatomia, Histologia, Embryologia* **36**, 157-9 (2007).

89. Stewart, M.D., Jang, C.W., Hong, N.W., Austin, A.P. & Behringer, R.R. Dual fluorescent protein reporters for studying cell behaviors in vivo. *Genesis* **47**, 708-17 (2009).

90. Griswold, S.L., Sajja, K.C., Jang, C.W. & Behringer, R.R. Generation and characterization of iUBC-KikGR photoconvertible transgenic mice for live time-lapse imaging during development. *Genesis* **49**, 591-8 (2011).

91. Nel-Themaat, L., Gonzalez, G., Akiyama, H. & Behringer, R.R. Illuminating testis morphogenesis in the mouse. *Journal Of Andrology* **31**, 5-10 (2010).

92. Akiyama H., Kim J.E., Nakashima K., Balmes G., Iwai N., Deng J.M., Zhang Z., Martin J.F., Behringer R.R., Nakamura T., & de Crombrugghe B. Osteo-chondroprogenitor cells are derived from Sox9 expressing precursors. *Proceedings Of The National Academy Of Sciences Of The United States Of America* **102**, 14665-70 (2005).

93. Shioi G., Kiyonari H., Abe T., Nakao K., Fujimori T., Jang C.W., Huang C.C., Akiyama H., Behringer R.R. & Aizawa S. A mouse reporter line to conditionally mark nuclei and cell membranes for in vivo live-imaging. *Genesis* **49**, 570-8 (2011).

94. Hama H., Kurokawa H., Kawano H., Ando R., Shimogori T., Noda H., Fukami K., Sakaue-Sawano A. & Miyawaki A. Scale: a chemical approach for fluorescence imaging and reconstruction of transparent mouse brain. *Nature Neuroscience* **14**, 1481-8 (2011).

95. Mescher, A.L. *Junqueira's Basic Histology, Text & Atlas*, (McGraw-Hill Medical, 2009).

96. The, I. & Perrimon, N. Morphogen diffusion: the case of the wingless protein. *Nature Cell Biology* **2**, E79-82 (2000).

97. Yamada, K.M. & Cukierman, E. Modeling tissue morphogenesis and cancer in 3D. *Cell* **130**, 601-10 (2007).

98. Tomooka, Y., DiAugustine, R.P. & McLachlan, J.A. Proliferation of mouse uterine epithelial cells in vitro. *Endocrinology* **118**, 1011-8 (1986).

99. Pritchett, J., Athwal, V., Roberts, N., Hanley, N.A. & Hanley, K.P. Understanding the role of SOX9 in acquired diseases: lessons from development. *Trends In Molecular Medicine* **17**, 166-74 (2011).

100. Thomsen, M.K., Butler, C.M., Shen, M.M. & Swain, A. Sox9 is required for prostate development. *Dev Biol* **316**, 302-11 (2008).

101. Perl, A.K., Kist, R., Shan, Z., Scherer, G. & Whitsett, J.A. Normal lung development and function after Sox9 inactivation in the respiratory epithelium. *Genesis* **41**, 23-32 (2005).

102. Bi, W., Deng, J.M., Zhang, Z., Behringer, R.R. & de Crombrugghe, B. Sox9 is required for cartilage formation. *Nat Genet* **22**, 85-9 (1999).

103. Barrionuevo, F. & Scherer, G. SOX E genes: SOX9 and SOX8 in mammalian testis development. *The International Journal Of Biochemistry & Cell Biology* **42**, 433-6 (2010).

104. Polanco, J.C., Wilhelm, D., Davidson, T.L., Knight, D. & Koopman, P. Sox10 gain-of-function causes XX sex reversal in mice: implications for human 22q-linked disorders of sex development. *Human Molecular Genetics* **19**, 506-16 (2010).

105. Sternberg, N. & Hamilton, D. Bacteriophage P1 site-specific recombination. I. Recombination between loxP sites. *J Mol Biol* **150**, 467-86 (1981).

106. Soyal S.M., Mukherjee A., Lee K.Y., Li J., Li H., DeMayo F.J. & Lydon J.P. Cre-mediated recombination in cell lineages that express the progesterone receptor. *Genesis* **41**, 58-66 (2005).

107. Akiyama, H., Chaboissier, M.C., Martin, J.F., Schedl, A. & de Crombrugghe, B. The transcription factor Sox9 has essential roles in successive steps of the chondrocyte differentiation pathway and is required for expression of Sox5 and Sox6. *Genes & Development* **16**, 2813-28 (2002).

108. Nel-Themaat L., Vadakkan T.J., Wang Y., Dickinson M.E., Akiyama H. & Behringer R.R. Morphometric analysis of testis cord formation in Sox9-EGFP mice. *Dev Dyn* **238**, 1100-10 (2009).

109. Zipfel W.R., Williams R.M., Christie R., Nikitin A.Y., Hyman B.T. & Webb W.W. Live tissue intrinsic emission microscopy using multiphoton-excited

native fluorescence and second harmonic generation. *Proceedings Of The National Academy Of Sciences Of The United States Of America* **100**, 7075-80 (2003).

110.   Burney R.O., Talbi S., Hamilton A.E., Vo K.C., Nyegaard M., Nezhat C.R., Lessey B.A. & Giudice L.C*.* Gene expression analysis of endometrium reveals progesterone resistance and candidate susceptibility genes in women with endometriosis. *Endocrinology* **148**, 3814-26 (2007).

111.   Talbi S., Hamilton A.E., Vo K.C., Tulac S., Overgaard M.T., Dosiou C., Le Shay N., Nezhat C.N., Kempson R., Lessey B.A., Nayak N.R. & Giudice L.C. Molecular phenotyping of human endometrium distinguishes menstrual cycle phases and underlying biological processes in normo-ovulatory women. *Endocrinology* **147**, 1097-121 (2006).

112.   Sharman, A. Post-partum regeneration of the human endometrium. *Journal Of Anatomy* **87**, 1-10 (1953).

113.   Barrionuevo F., Naumann A., Bagheri-Fam S., Speth V., Taketo M.M., Scherer G. & Neubüser A. Sox9 is required for invagination of the otic placode in mice. *Developmental Biology* **317**, 213-24 (2008).

114.   Qi, J., Pellecchia, M. & Ronai, Z.A. The Siah2-HIF-FoxA2 axis in prostate cancer - new markers and therapeutic opportunities. *Oncotarget* **1**, 379-85 (2010).

115.   Amarilio R., Viukov S.V., Sharir A., Eshkar-Oren I., Johnson R.S. & Zelzer E. HIF1alpha regulation of Sox9 is necessary to maintain differentiation of

hypoxic prechondrogenic cells during early skeletogenesis. *Development* **134**, 3917-28 (2007).

116. Sakai, D., Suzuki, T., Osumi, N. & Wakamatsu, Y. Cooperative action of Sox9, Snail2 and PKA signaling in early neural crest development. *Development* **133**, 1323-33 (2006).

117. Spokony, R.F., Aoki, Y., Saint-Germain, N., Magner-Fink, E. & Saint-Jeannet, J.P. The transcription factor Sox9 is required for cranial neural crest development in Xenopus. *Development* **129**, 421-32 (2002).

118. Akiyama H., Lyons J.P., Mori-Akiyama Y., Yang X., Zhang R., Zhang Z., Deng J.M., Taketo M.M., Nakamura T., Behringer R.R., McCrea P.D. & de Crombrugghe B. Interactions between Sox9 and beta-catenin control chondrocyte differentiation. *Genes & Development* **18**, 1072-87 (2004).

119. Bernard P., Ryan J., Sim H., Czech D.P., Sinclair A.H., Koopman P. & Harley V.R. Wnt Signaling in Ovarian Development Inhibits Sf1 Activation of Sox9 via the Tesco Enhancer. *Endocrinology* **153**, 901-12 (2012).

120. Stern, C.D. Neural induction: old problem, new findings, yet more questions. *Development* **132**, 2007-21 (2005).

121. Reginensi A., Clarkson M., Neirijnck Y., Lu B., Ohyama T., Groves A.K., Sock E., Wegner M., Costantini F., Chaboissier M.C. & Schedl A. SOX9 controls epithelial branching by activating RET effector genes during kidney development. *Hum Mol Genet* **20**, 1143-53 (2011).

122. Darido C., Buchert M., Pannequin J., Bastide P., Zalzali H., Mantamadiotis T., Bourgaux J.F., Garambois V., Jay P., Blache P., Joubert

D. & Hollande F.. Defective claudin-7 regulation by Tcf-4 and Sox-9 disrupts the polarity and increases the tumorigenicity of colorectal cancer cells. *Cancer Res* **68**, 4258-68 (2008).

123. Jiang S.S., Fang W.T., Hou Y.H., Huang S.F., Yen B.L., Chang J.L., Li S.M., Liu H.P., Liu Y.L., Huang C.T., Li Y.W., Jang T.H., Chan S.H., Yang S.J., Hsiung C.A., Wu C.W., Wang L.H. & Chang I.S. Upregulation of SOX9 in lung adenocarcinoma and its involvement in the regulation of cell growth and tumorigenicity. *Clin Cancer Res* **16**, 4363-73 (2010).

124. Wang H., Leav I., Ibaragi S., Wegner M., Hu G.F., Lu M.L., Balk S.P, Yuan X. SOX9 is expressed in human fetal prostate epithelium and enhances prostate cancer invasion. *Cancer Res* **68**, 1625-30 (2008).

125. Dutt A., Salvesen H.B., Chen T.H., Ramos A.H., Onofrio R.C., Hatton C., Nicoletti R., Winckler W., Grewal R., Hanna M., Wyhs N., Ziaugra L., Richter D.J., Trovik J., Engelsen I.B., Stefansson I.M., Fennell T., Cibulskis K., Zody M.C., Akslen L.A., Gabriel S., Wong K.K., Sellers W.R., Meyerson M. & Greulich H. Drug-sensitive FGFR2 mutations in endometrial carcinoma. *Proc Natl Acad Sci U S A* **105**, 8713-7 (2008).

126. Kim Y., Murao H., Yamamoto K., Deng J.M., Behringer R.R., Nakamura T.& Akiyama H. Generation of transgenic mice for conditional overexpression of Sox9. *Journal Of Bone And Mineral Metabolism* **29**, 123-9 (2011).

127. Ferenczy, A. Pathophysiology of adenomyosis. *Hum Reprod Update* **4**, 312-22 (1998).

128. Dharma, S.J., Kholkute, S.D. & Nandedkar, T.D. Apoptosis in endometrium of mouse during estrous cycle. *Indian Journal Of Experimental Biology* **39**, 218-22 (2001).

129. Mitsumori K., Onodera H., Shimo T., Yasuhara K., Takagi H., Koujitani T., Hirose M., Maruyama C. & Wakana S. Rapid induction of uterine tumors with p53 point mutations in heterozygous p53-deficient CBA mice given a single intraperitoneal administration of N-ethyl-N-nitrosourea. *Carcinogenesis* **21**, 1039-42 (2000).

130. Neven, P., De Muylder, X., Van Belle, Y., Vanderick, G. & De Muylder, E. Tamoxifen and the uterus and endometrium. *Lancet* **1**, 375 (1989).

131. Ismail, S.M. Pathology of endometrium treated with tamoxifen. *Journal Of Clinical Pathology* **47**, 827-33 (1994).

132. McCluggage, W.G., Desai, V. & Manek, S. Tamoxifen-associated postmenopausal adenomyosis exhibits stromal fibrosis, glandular dilatation and epithelial metaplasias. *Histopathology* **37**, 340-6 (2000).

133. Guo W., Keckesova Z., Donaher J.L., Shibue T., Tischler V., Reinhardt F., Itzkovitz S., Noske A., Zürrer-Härdi U., Bell G., Tam W.L., Mani S.A., van Oudenaarden A. & Weinberg R.A. Slug and Sox9 cooperatively determine the mammary stem cell state. *Cell* **148**, 1015-28 (2012).

134. Hou, X., Tan, Y., Li, M., Dey, S.K. & Das, S.K. Canonical Wnt signaling is critical to estrogen-mediated uterine growth. *Mol Endocrinol* **18**, 3035-49 (2004).

135. Franco H.L., Lee K.Y., Rubel C.A., Creighton C.J., White L.D., Broaddus R.R., Lewis M.T., Lydon J.P., Jeong J.W. & DeMayo F.J. Constitutive activation of smoothened leads to female infertility and altered uterine differentiation in the mouse. *Biology Of Reproduction* **82**, 991-9 (2010).

136. Furuyama K., Kawaguchi Y., Akiyama H., Horiguchi M., Kodama S., Kuhara T., Hosokawa S., Elbahrawy A., Soeda T., Koizumi M., Masui T., Kawaguchi M., Takaori K., Doi R., Nishi E., Kakinoki R., Deng J.M., Behringer R.R., Nakamura T. & Uemoto S. Continuous cell supply from a Sox9-expressing progenitor zone in adult liver, exocrine pancreas and intestine. *Nature Genetics* **43**, 34-41 (2011).

137. Gargett, C.E. & Masuda, H. Adult stem cells in the endometrium. *Mol Hum Reprod* **16**, 818-34 (2010).

138. Kaitu'u-Lino, T.J., Ye, L. & Gargett, C.E. Reepithelialization of the uterine surface arises from endometrial glands: evidence from a functional mouse model of breakdown and repair. *Endocrinology* **151**, 3386-95 (2010).

139. Frank D.U., Elliott S.A., Park E.J., Hammond J., Saijoh Y. & Moon A.M. System for inducible expression of cre-recombinase from the Foxa2 locus in endoderm, notochord, and floor plate. *Dev Dyn* **236**, 1085-92 (2007).

140. McDowall S., Argentaro A., Ranganathan S., Weller P., Mertin S., Mansour S., Tolmie J. & Harley V. Functional and structural studies of wild type SOX9 and mutations causing campomelic dysplasia. *J Biol Chem* **274**, 24023-30 (1999).

141. Furumatsu T., Tsuda M., Yoshida K., Taniguchi N., Ito T., Hashimoto M., Ito T. & Asahara H. Sox9 and p300 cooperatively regulate chromatin-mediated transcription. *J Biol Chem* **280**, 35203-8 (2005).

142. Oh C.D., Maity S.N., Lu J.F., Zhang J., Liang S., Coustry F., de Crombrugghe B. & Yasuda H. Identification of SOX9 interaction sites in the genome of chondrocytes. *PLoS One* **5**, e10113 (2010).

143. Mouse Genome Sequencing, C. *et al.* Initial sequencing and comparative analysis of the mouse genome. *Nature* **420**, 520-62 (2002).

144. Cock, P.J., Fields, C.J., Goto, N., Heuer, M.L. & Rice, P.M. The Sanger FASTQ file format for sequences with quality scores, and the Solexa/Illumina FASTQ variants. *Nucleic Acids Res* **38**, 1767-71 (2010).

145. Langmead, B., Trapnell, C., Pop, M. & Salzberg, S.L. Ultrafast and memory-efficient alignment of short DNA sequences to the human genome. *Genome Biol* **10**, R25 (2009).

146. Li H., Handsaker B., Wysoker A., Fennell T., Ruan J., Homer N., Marth G., Abecasis G., Durbin R.; 1000 Genome Project Data Processing Subgroup. The Sequence Alignment/Map format and SAMtools. *Bioinformatics* **25**, 2078-9 (2009).

147. Zhang Y., Liu T., Meyer C.A., Eeckhoute J., Johnson D.S., Bernstein B.E., Nusbaum C., Myers R.M., Brown M., Li W., Liu X.S. Model-based analysis of ChIP-Seq (MACS). *Genome Biol* **9**, R137 (2008).

148. Tian W., Salanova M., Xu H., Lindsley J.N., Oyama T.T., Anderson S., Bachmann S. & Cohen D.M. Renal expression of osmotically responsive

cation channel TRPV4 is restricted to water-impermeant nephron segments. *American Journal Of Physiology. Renal Physiology* **287**, F17-24 (2004).

149.   Arniges, M., Vazquez, E., Fernandez-Fernandez, J.M. & Valverde, M.A. Swelling-activated Ca2+ entry via TRPV4 channel is defective in cystic fibrosis airway epithelia. *The Journal Of Biological Chemistry* **279**, 54062-8 (2004).

150.   Chung, M.K., Lee, H. & Caterina, M.J. Warm temperatures activate TRPV4 in mouse 308 keratinocytes. *The Journal Of Biological Chemistry* **278**, 32037-46 (2003).

151.   D'Aldebert E., Cenac N., Rousset P., Martin L., Rolland C., Chapman K., Selves J., Alric L., Vinel J.P. & Vergnolle N. Transient receptor potential vanilloid 4 activated inflammatory signals by intestinal epithelial cells and colitis in mice. *Gastroenterology* **140**, 275-85 (2011).

152.   Becker, D., Blase, C., Bereiter-Hahn, J. & Jendrach, M. TRPV4 exhibits a functional role in cell-volume regulation. *Journal Of Cell Science* **118**, 2435-40 (2005).

153.   Delany N.S., Hurle M., Facer P., Alnadaf T., Plumpton C., Kinghorn I., See C.G., Costigan M., Anand P., Woolf C.J., Crowther D., Sanseau P. & Tate S.N. Identification and characterization of a novel human vanilloid receptor-like protein, VRL-2. *Physiological Genomics* **4**, 165-74 (2001).

154.   Liedtke W., Choe Y., Martí-Renom M.A., Bell A.M., Denis C.S., Sali A., Hudspeth A.J., Friedman J.M. & Heller S. Vanilloid receptor-related

osmotically activated channel (VR-OAC), a candidate vertebrate osmoreceptor. *Cell* **103**, 525-35 (2000).

155.   Reiter B., Kraft R., Günzel D., Zeissig S., Schulzke J.D., Fromm M. & Harteneck C. TRPV4-mediated regulation of epithelial permeability. *The FASEB Journal : Official Publication Of The Federation Of American Societies For Experimental Biology* **20**, 1802-12 (2006).

Vita

Gabriel Gonzalez Ballester was born in Miami, Florida on September 26, 1979, the second son of Carlos Antonio Gonzalez Alers and Emilia Mercedes Ballester Medina. He received the degree of Bachelor of Science with a major in biology from the University of Puerto Rico, Mayagüez, in May 2001. In 2001, joined the United States Air Force where he worked as a medical laboratory technician. In 2006, he joined the University of Texas M.D. Anderson Cancer Center in the department of Stem Cell Transplantation as a Clinical Cell Therapy Specialist. In September of 2006, he entered the University of Texas Health Science Center at Houston Graduate School of Biomedical Sciences. He completed all the requirements for the M.S. degree in 2008 and stayed in Dr. Behringer's lab to pursue his Ph.D.

Permanent address:

14707 Arbor Trace

Cypress, Texas 77429